SYNTHESIS AND PROPERTIES OF CHARGE TRANSFER SALTS OF BEDT-TTF.

by

Anthony William Graham

PhD. Thesis

University College London

A thesis submitted to the University of London for the degree of Doctor of Philosophy.

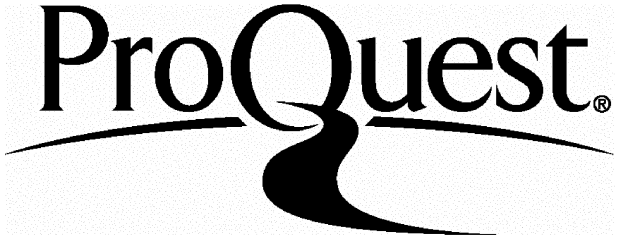

Abstract

This research project has investigated the interplay of superconductivity and magnetism in organic systems, with the ultimate aim of observing their co-existence. In order to pursue this study, a series of charge transfer salts of BEDT-TTF (BEDT-TTF = bis ethylenedithio tetrathiafulvalene) have been successfully prepared with $M(C_2O_4)_3^{3-}$ anions (M = Fe, Cr and Co). The anion has been varied to systematically monitor the effect of localised moments on the conducting properties.

Crystals with the general formula $(BEDT\text{-}TTF)_4AFe(C_2O_4)_3.C_6H_5CN$ (A = K, NH_4 or H_2O) have been electrocrystallised and identified by X - ray crystallography. In the salts where A = K or NH_4 a novel packing arrangement of the BEDT-TTF moiety is observed which involves the formation of monopositive BEDT-TTF units dimerising. These dimers are surrounded by six neutral BEDT-TTF molecules. Both of these materials are semiconductors with an activation energy of 0.14eV. Susceptibility measurements indicate that the dimers are spin paired and therefore the magnetic properties are dominated by the high spin Fe^{3+} complex. These results are reported in Chapter 3.

The A = H_2O salt is reported in Chapter 4. It is the first molecular superconductor containing localised magnetic moments, which has a transition temperature of 8.5K to the superconducting state. The BEDT-TTF molecules pack in the β" fashion, which facilitates considerable overlap of the Sulfur orbitals. Susceptibility measurements at low field verify the superconducting transition, but as the field is increased, the paramagnetic signal from the Fe^{3+} becomes more dominant. At fields greater than 1 Tesla, the superconductivity is destroyed and the material obeys the Curie - Weiss law to 2K. A contribution from the conduction electrons is also observed. Band structure calculations suggest two dimensional metallic behaviour.

Chapter 5 collates other compounds which have been prepared from solutions of BEDT-TTF and $M(C_2O_4)_3^{3-}$ (M = Fe, Cr, Co) in Benzonitrile. This has resulted in several new phases being isolated but due to multiple twinning, their structures have not yet been determined. Crystals grown from the solution where M = Cr are semimetallic to ~ 150K at which temperature it undergoes a transition to the insulating state. The solvent has also been modified to include 5% Methanol. This has resulted in a superconducting phase whose lattice parameters have been determined. Efforts are currently being made to determine the full crystal structure. SQUID measurements indicate a T_c of 7.5K.

Acknowledgements

I would like to thank my supervisor Peter Day for giving me such an interesting project to work on. He has been a constant source of support and encouragement throughout both the highs and the lows of this research programme . For this I am extremely grateful.

I should also like to thank the other members of the Day group throughout my time at The Royal Institution. Mo has been a source of expertise in the area of synthetic metals and his steady hands have helped in the mounting of the tiniest of crystals. Simon has always been willing to offer advice on susceptibility experiments, computers and the best beer available at The Duke of Albemarle, where we have had many fruitful discussions concerning this project. In the early days of the oxalates, I also had many helpful discussions with Chris about honeycombs and κ-phase materials. It has also been good to share a lab with Martin over the last year, allowing us to reminisce over old times in Bangor.

The other groups at The Royal Institution have also shown a great willingness to help in whatever way they can. I would particularly like to thank Dewi, Rob and Dave for teaching me how to use Insight II; Mark for shooting down most problems with the Macintosh and Phil, Yvonne, Jason, Ashley, Robin, Dean, Julian, Shyam, Phil, Sankar, Eddie, Sharon and Sarah for their friendship over the last three years.

I must also thank the members of other laboratories who I have collaborated with over the last three years. Simon Coles and Mike Hursrhouse always gave me a warm welcome in Cardiff and worked tirelessly in trying to get the structures of my invariably twinned crystals. In Bordeaux, Phillipe Guionneau and Laurent Ducasse taught me how to perform Band Structure Calculations and attempted pressure measurements were performed in collaboration with Helmut Becker in Cambridge.

Finally, I would like to thank my Mum and Dad and the rest of my family for their continued support (both emotional and financial) throughout my student career. I've finally given in to you and got a real job!

Table of Contents

List of Figures

List of Tables

Chapter 1

Introduction and Theory.

Chapter 1. Introduction and Theory

1.1 Introductory Remarks

A superconductor is a medium through which an electric current can be passed without experiencing any resistance. Other properties which arise from the superconducting state are; a change in the specific heat; a decrease in entropy; and perhaps as fascinating as having no resistance, a superconductor also acts as a perfect diamagnet. It is the intention of this chapter to give the reader a historical perspective of superconductivity, in particular organic superconductors; a brief explanation of the theoretical aspects of magnetism and superconductivity; and to state the aims of this research project.

1.2 The history of Superconductors.

1.2.1 Metals.

The resistivity of a metal decreases with temperature. The liquefaction of Helium by Kamerlingh Onnes in 1908 enabled the electrical transport of metals to be studied to lower temperatures. Studies into this temperature regime led to the discovery of superconductivity by the same author in a freshly distilled sample of mercury [1]. At a critical temperature (T_c) of 4.2K, the electrical resistance vanished completely (Figure 1.1) and the science of superconductivity was born.

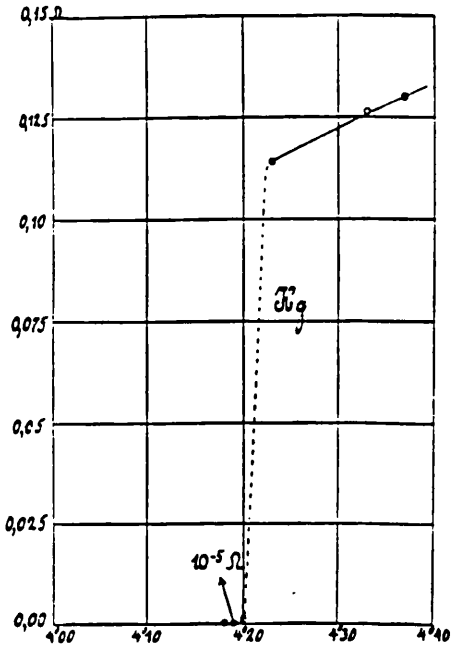

Figure 1.1 The discovery of superconductivity in mercury by Onnes.

This discovery initiated the search for superconductivity in other metals which resulted in the unearthing of several other superconductors and the raising of T_c to 9.5K in Niobium. However, in order for a superconductor to be practically viable, it is necessary to have transition temperatures which are considerably higher than those observed in metals. One strategy employed to achieve this goal was to prepare alloys of different metals and this approach led to the raising of T_c to 23K in a 3:1 alloy of Niobium and Germanium [2]. It is interesting to note that Germanium metal does not superconduct.

1.2.2 Other Superconducting Families

Since the discovery of superconductivity in metals, many other more elaborate superconducting systems have been developed. A summary of these families is given in Table 1.1, from which the diversity of Chemistry involved in achieving the superconducting state can be fully appreciated. These materials range from Ceramics to Organics with an equally large spread in the value of T_c. It is out of place to discuss

the details of these systems in a thesis concerned with organic superconductors. However, it would be incomplete to omit the advances in this area of science in recent years, in particular the ceramic systems which have led to the discovery of high temperature superconductivity. Therefore, a brief discussion will follow on ceramic superconductors. For greater insight into these materials, the reader is guided towards the relevant references.

Family	T_c (K)	Example	Reference
Ceramics	156	$HgBa_2Ca_2Cu_3O_{8+\delta}$	5
Fullerenes	33	Rb_2CsC_{60}	6
Alloys	23	Nb_3Ge	7
Chalcogenides	15	$PbMo_6S_8$	8
Organics	12.8	$(BEDT\text{-}TTF)_2Cu[N(CN)_2]Cl$	9
Borides	11.7	$ErRh_4B_4$	10
Atomic Elements	9.3	Nb	11
Silicides	7.6	$(Ln)_2Fe_3Si_5$	12
Intercalates	6	$SnSe_2[Co(C_5H_5)_2]_{0.33}$	13

Table 1.1 Examples of superconducting families.

One of the most exciting discoveries in the solid state over the last decade was the classic publication by Bednorz and Müller who discovered superconductivity at 40K in $Ln_{2-x}Ba_xCuO_4$[3]. This system allowed the Lanthanide to be varied and therefore a systematic approach for increasing T_c to even higher values could be employed. This encouraged the belief that the electronics industry would be revolutionised by the discovery of room temperature superconductors and hence it initiated an explosion in this area of research. In 1987, Chu discovered superconductivity in the electron deficient $YBa_2Cu_3O_{7-\gamma}$ compound with a T_c of 90K [4]. This was the first material to

superconduct above the boiling point of liquid Nitrogen and thus the use of expensive liquid Helium was no longer required to achieve the superconducting state. This rapid increase in T_c resulted in predictions that a room temperature superconductor would soon be prepared. However, the increase of T_c with time did not remain constant. Despite this, T_c has been raised to 156K (under pressure) in the $HgBa_2Ca_2Cu_3O_{8+\delta}$ system [5] and there is still a concentrated research effort in achieving even higher transition temperatures.

The structures of the cuprate superconductors have one common feature. That is they consist of planes of CuO_2 which are slightly doped away from a charge of Cu^{2+}. The extra holes generated by the doping change the electrical properties from being insulating to becoming superconducting.

Another exciting discovery was the observation of superconductivity in Fullerenes. Charge transfer salts of C_{60} have been prepared with alkali metal cations to achieve transition temperatures as high as 40K in Cs_3C_{60}.

The following sections will concentrate on Organic superconductors, in particular those based upon BEDT-TTF.

1.2.3 Organic Superconductors

The possibility of organic superconductivity was first postulated in 1911 by Moore and McCoy [14]. This was expanded further in 1956 when Little predicted that high temperature superconductivity might be realised in organic systems [15]. However, it was not until 1971 that the first organic metal was reported. It was a charge transfer salt containing the TTF and TCNQ moieties [16]. This material remained metallic to 54K, at which temperature it underwent a phase transition to a semi conducting state.

By the end of the decade, organic superconductivity had been realised (see section 1.2.3.1).

Today, there are numerous organic molecules whose charge transfer salts possess superconducting properties. In order to avoid quoting long and awkward organic names, these materials have acronyms which are summarised in Figure 1.2. The following sections will give a historical account of organic superconductors and will concentrate on the BEDT-TTF system which is the focal point of this project.

DONORS

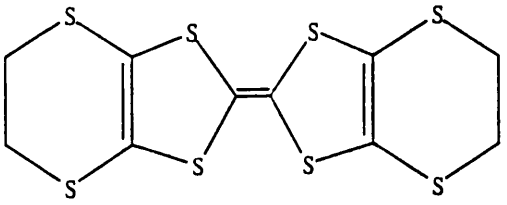

BEDT-TTF (ET)

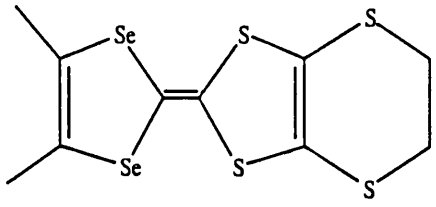

DMET

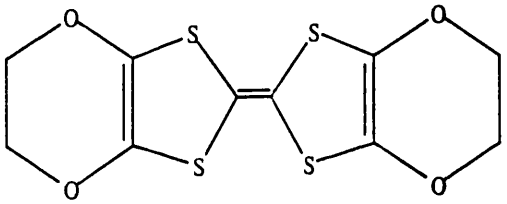

BEDO-TTF

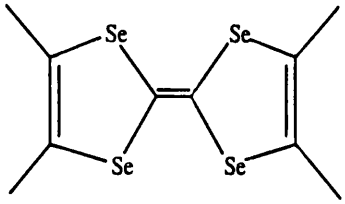

TMTSF

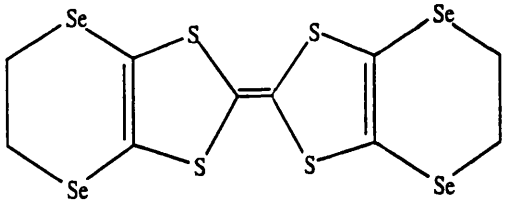

BEDSe-TTF

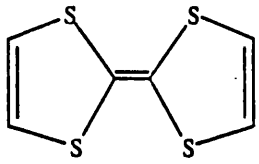

TTF

ACCEPTORS

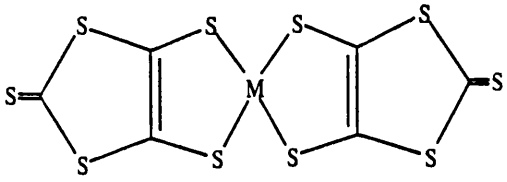

$M(dmit)_2$

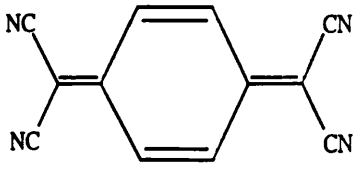

TCNQ

Figure 1.2 Structures of various organic donor and acceptor molecules.

1.2.3.1 Bechgaard Salts

The breakthrough for organic superconductivity came in 1979 when Bechgaard started to use small monovalent inorganic anions instead of larger organic systems in order to form the charge transfer salts [17]. These salts were grown electrochemically, and the precedent was set for the electrocrystallisation of this class of materials. This technique is described in section 2.2.4.

Bechgaard formed charge transfer salts of the organic donor molecule TMTSF with tetrahedral and octahedral monovalent anions. The appropriate $[NBu_4]^+$ salt was dissolved in an organic solvent and acted as the electrolyte during the electrocrystallisation procedure. These experiments yielded the first organic superconductors, albeit ones with very low transition temperatures (~1K). They also required the application of large hydrostatic pressure for the superconducting state to be realised, with the exception of the perchlorate salt which was the first ambient pressure organic superconductor. These results are summarised in Table 1.2 [18].

TMTSF Superconductor	T_c (K)
$(TMTSF)_2ClO_4$	1.4
$(TMTSF)_2PF_6$	1.4 (6.5kbar)
$(TMTSF)_2AsF_6$	1.4 (9.5kbar)
$(TMTSF)_2SbF_6$	0.38 (10.5kbar)
$(TMTSF)_2TaF_6$	1.35 (11kbar)
$(TMTSF)_2ReO_4$	1.2 (9.5kbar)
$(TMTSF)_2FSO_3$	3 (5kbar)

Table 1.2 Superconducting charge transfer salts of TMTSF.

The stoichiometery of these compounds is always $(TMTSF)_2^+ X^-$ (X = monovalent anion), resulting in a 3/4 filled electronic band. This leads to metallic properties, but due to lattice instabilities, semi conducting behaviour is often observed [19].

1.2.3.2 BEDT-TTF Salts

One dimensional metals become unstable to lattice instabilities as temperature is lowered. In order to reduce its energy, the material will undergo a phase transition involving the opening of a band gap at the Fermi Level resulting in a metal - insulator transition. It is necessary to apply pressure to the Bechgaard salts in order to surpress such a transition to the insulating state. Therefore, there was a drive to increase the dimensionality of the conduction network.

In 1982, Mizuno *et al* prepared BEDT-TTF [20]. This is a symmetrical donor molecule which consists of two inner organo sulfur five membered rings joined together by a carbon - carbon double bond (TTF). On the outside of these rings is an additional six membered organo - sulfur ring. (see Figure 1.2). There is a C_2 rotation axis perpendicular to the central carbon carbon double bond.

There are now eight sulfur atoms in the donor molecule with close intermolecular sulfur - sulfur contact distances. When charge transfer salts of BEDT-TTF are formed the structures generally consist of stacks of the donor molecules being separated by stacks of the acceptor molecule. The packing observed in the BEDT-TTF layer facilitates considerable overlap of the Sulfur orbitals and this results in the electrical properties being more two dimensional in nature.

A further effect of adding the additional organo sulfur rings is that the planarity of the molecule has been destroyed. The saturated outer rings can adopt many different conformations with respect to each other. For example, both rings may be in the more

stable chair conformation and staggered with respect to each other. Alternatively, they may be eclipsed or one or both rings may be in the boat conformation. This structural diversity enables BEDT-TTF based materials to adopt many different conformations and consequently packing motifs. This will be discussed in more detail later in this section.

Table 1.3 collates BEDT-TTF based superconductors. This indicates that anions of different sizes, shapes, charges, and magnetism can be used in the preparation of superconducting organic materials. The variety of compounds obtained has resulted in the discovery of many new ambient pressure superconductors, higher T_c's and, as will be reported in this thesis, the first molecular superconductor containing localised moments.

Table 1.3 Superconducting charge transfer salts of BEDT-TTF.

BEDT-TTF Superconductor	T_c (K)	Reference
κ-(BEDT-TTF)$_2$Cu[N(CN)$_2$]Cl	12.8 (0.3kbar)	21
κ-(BEDT-TTF)$_2$Cu[N(CN)$_2$]Br	11.6	22
κ-(BEDT-TTF)$_2$Cu[N(CN)$_2$]CN	11.3	23
κ-(BEDT-TTF)$_2$Cu[N(CN)$_2$]Cl$_{0.5}$Br$_{0.5}$	11.2	24
κ-(BEDT-TTF)$_2$Cu(NCS)$_2$	10.4	25
κ-(BEDT-TTF)$_2$M(CF$_3$)$_4$).S	3.8 - 10.2	26
(M = Cu, Ag, Au; S = trihaloethylene)		
β" (BEDT-TTF)$_4$(H$_2$O)Fe(C$_2$O$_4$)$_3$.C$_6$H$_5$CN	8.5	27
β*(BEDT-TTF)$_2$I$_3$	8 (0.5kbar)	28
α_t-(BEDT-TTF)$_2$I$_3$	7-8	29
(BEDT-TTF)$_4$Hg$_3$Cl$_8$	5.3 (29kbar)	30

BEDT-TTF Superconductor	T_c (K)	Reference
β-(BEDT-TTF)$_2$AuI$_2$	5.0	31
κ-(BEDT-TTF)$_2$Ag(CN)$_{2.}$H$_2$O	5.0	32
(BEDT-TTF)$_4$Hg$_{2.89}$Br$_8$	4.3, 6.7 (3.5kbar)	33
κ-(BEDT-TTF)$_2$Cu(CF$_3$)$_4$).TCE	4.0	34
κ-(BEDT-TTF)$_2$Cu$_2$(CN)$_3$	3.8	35
κ-(BEDT-TTF)$_2$I$_3$	3.6	36
θ-(BEDT-TTF)$_2$(I$_3$)$_{1-x}$(AuI$_2$)$_x$ (x<0.02)	3.6	37
β-(BEDT-TTF)$_2$IBr$_2$	2.8	38
γ-(BEDT-TTF)$_3$(I$_3$)$_{2.5}$	2.5	39
(BEDT-TTF)$_2$ReO$_4$	2.0 (4.5kbar)	40
(BEDT-TTF)$_4$Pt(CN)$_4$.H$_2$O	2.0 (6.5kbar)	41
(BEDT-TTF)$_3$Cl$_2$.2H$_2$O	2.0 (16kbar)	42
β-(BEDT-TTF)$_2$I$_3$	1.4	43
(BEDT-TTF)$_4$Pd(CN)$_4$.H$_2$O	1.2 (7kbar)	44
α-(BEDT-TTF)$_2$NH$_4$Hg(SCN)$_4$	1.15	45

The following sections will give a brief overview of the work which has been undertaken on BEDT-TTF charge transfer salts.

Superconductivity was first realised in BEDT-TTF based compounds in 1983 when Parkin *et al* synthesised (BEDT-TTF)$_2$ReO$_4$, which is an ambient pressure superconductor with a T_c of 2K [40]. This discovery led to the preparation of other analogues to the Bechgaard salts, but no other superconducting phases were isolated. The breakthrough came in 1984 when Williams *et al* prepared (BEDT-TTF)$_2$I$_3$. Again, this material was an ambient pressure superconductor, with a T_c of 1.4K [43]. The BEDT-TTF molecules pack in the β - phase, which affords considerable overlap of the BEDT-TTF Sulfur orbitals. Many other phases of (BEDT-TTF$_2$I$_3$ have also

been isolated and thus organic superconductors containing the same molecules, with the same stoichiometeries now had a range of transition temperatures from 1.4 - 8K. The difference between these materials is how the BEDT-TTF molecules pack with respect to each other and consequently, the nature of the sulfur and carbon orbital overlap. The organic molecules can pack in many different formations, and two examples which are relevant to this thesis, the β - phase and the κ - phase are illustrated in Figure 1.3.

The phases are identified by viewing the BEDT-TTF layer along the long molecular axis. For clarity the charge compensating anionic layer is removed from the diagram to obtain a clearer perspective of the organic layer.

The β-phase consists of BEDT-TTF molecules which stack directly on top of each other. However, the next stack is translated so that the two stacks are not side to side to each other. Within the stack, the BEDT-TTF molecules are slightly dimerised which results in short Sulfur - Sulfur contact distances. However, band structure calculations indicate that the primary direction of electronic transport is between stacks.

The κ- phase has led to the discovery of the highest T_c organic superconductors (excluding Fullerenes). The BEDT-TTF molecules form face to face dimers which again results in the overlap of sulfur orbitals between dimer pairs. Adjacent dimer pairs are orthogonal to each other and according to band structure calculations, there is very little electronic interaction between them. The primary network for the electrical conduction thus comes from the dimer. However, two dimensional behaviour is observed, as there is sufficient interaction for the electrons to travel between the dimer pairs.

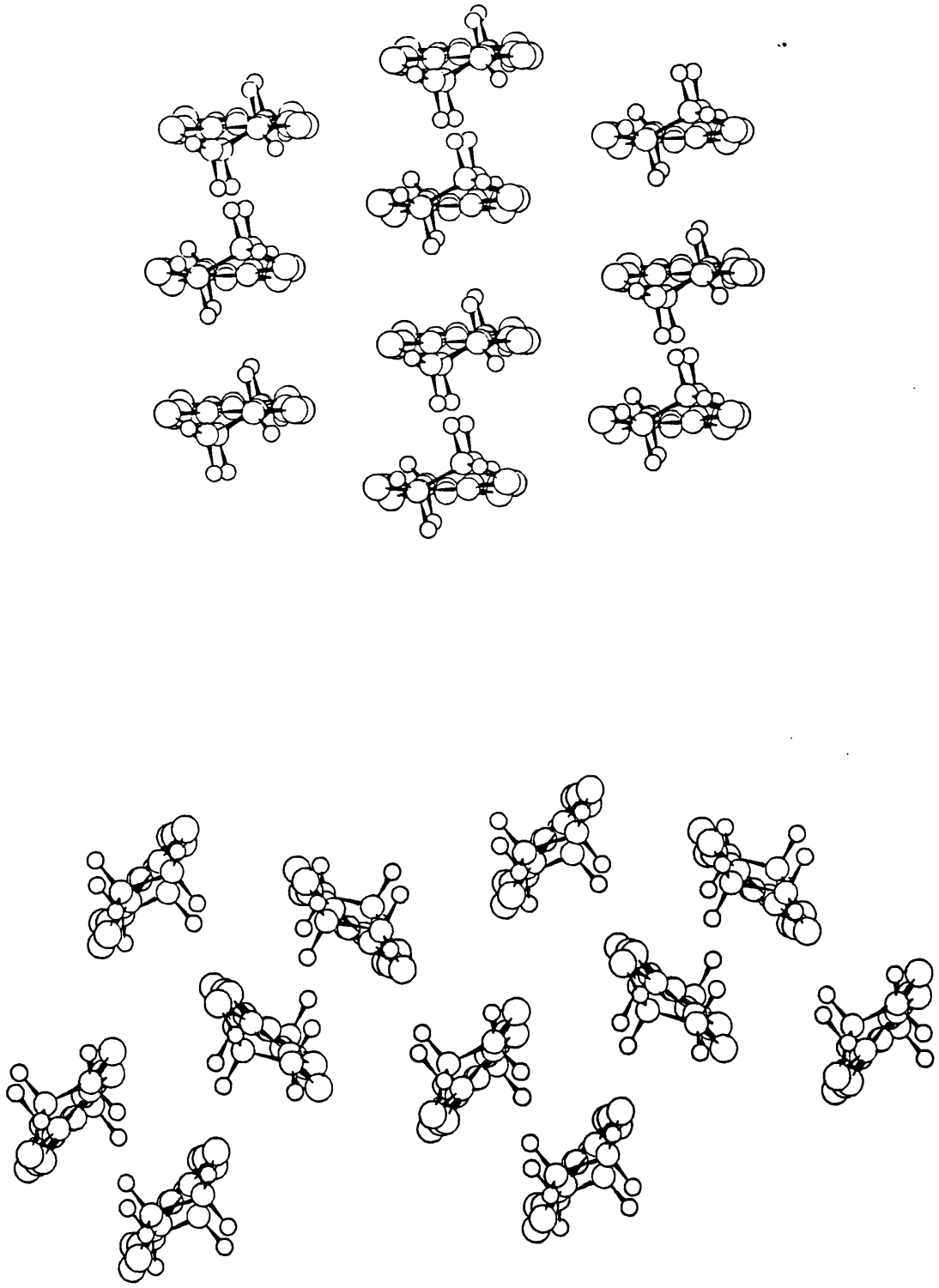

Figure 1.3 The BEDT-TTF layer illustrating the β-phase (top) and the κ-phase (bottom).

Further to the discovery of novel crystalline phases of BEDT-TTF, the discovery of superconductivity in $(BEDT\text{-}TTF)_2I_3$ also enabled a systematic investigation into the superconducting state. BCS theory (Section 1.3.3.1) states that by increasing the density of states at the Fermi level the transition temperature to the superconducting state will increase. This can be achieved by using longer anions than I_3^-, which would decrease the overlap of the sulfur orbitals thereby increasing the density of states (Section 1.3.2.1). This theory was examined by preparing compounds of $(BEDT\text{-}TTF)_2X$ where X = IBr_2, AuI_2, $Cu(NCS)_2$, $Cu[N(CN)_2]Br$ and $Cu[N(CN)_2]Cl$. Williams *et al* observed that there was a linear relationship between the unit cell volume and the value of T_c in the β - phase materials [46]. This trend has also been realised in the κ - phase materials and in superconducting C_{60} charge transfer salts [47]. However, it is important to note that not all $(BEDT\text{-}TTF)_2X$ salts where X is a linear anion are superconductors.

Monovalent anions are not the only acceptor molecules which have been utilised to produce superconducting phases. A study undertaken by Mori *et al* led to the discovery of superconductivity in $(BEDT\text{-}TTF)_4M(CN)_4.H_2O$ where M = Pt or Pd. These compounds have transition temperatures of 2K (6.5kbar) [42] and 1.2K (7kbar) [44] respectively under high applied pressure. An interesting point to come out of this study was that the anhydrous salts underwent a broad metal - insulator transition at about 250K which could not be suppressed by the application of pressure [48]. Therefore, the presence of water in these materials is crucial to achieving the superconducting state. The authors of these publications postulated that the Hydrogen bonding interactions between the Nitrogen atoms on the anion to the Hydrogen atoms on the water, and the Hydrogen atoms on the terminal ethylene groups of the BEDT-TTF to the Oxygen atom on the water are crucial to the existence of the superconducting state. Other hydrated salts are now known, in which the water molecule forms Hydrogen bonds with both the donor and acceptor ions, resulting in the formation of a superconducting material (see Table 1.3).

Yamochi *et al* have proposed that Hydrogen bonding interactions between BEDT-TTF and the anion layer are critical in determining the packing of the BEDT-TTF molecules [49]. Their studies were concerned with κ - phase superconducting salts of (BEDT-TTF)$_2$Cu(CN)[N(CN)$_2$] and (BEDT-TTF)$_2$Cu$_2$(CN)$_3$. They demonstrate that the Hydrogen atoms of the BEDT-TTF molecules reside in a cavity of the anion layer and their position is determined by Hydrogen bonding interactions. This in turn drives the packing of the cation layer. Therefore, the docking of the BEDT-TTF molecule onto the anion layer is crucial for determining the phase of the charge transfer salt.

1.2.3.3 Other Organic Systems

As has been discussed, there have been a multitude of superconducting phases prepared with the BEDT-TTF cation. A challenge for synthetic chemists has therefore been to prepare other organic molecules whose charge transfer salts would form superconducting phases. This research has taken a three pronged approach. Firstly, to replace the Sulfur atoms in the BEDT-TTF molecule by other atoms such as Selenium (BEDT-TSF) [50] or Oxygen (BEDO-TTF) [51]; secondly to form hybrid structures of well known donor molecules (DMET)[52] ; and thirdly to extend the length of the existing molecules [53]. One series of compounds not yet covered in this short overview are the M(dmit)$_2$ (M = Ni, Pt or Pd) systems, which are the only organic superconductors based upon acceptor molecules [54].

Organic Superconductor	T_c (K)	Reference
$(BETSe\text{-}TSF)_2GaCl_4$	8	55
$(BETSe\text{-}TSF)_2GaCl_3Br$	7.5	56
α'-$(TTF)[Pd(dmit)_2]_2$	6.42 (20.7 kbar)	57
$(BETSe\text{-}TSF)_{2(}GaCl_4)_{0.5}(FeCl_4)_{0.5}$	5	58
$(NMe)_4[Ni(dmit)_2]_2$	5.0 (7kbar)	59
$(MDT\text{-}TTF)_2AuI_2$	4.5	60
κ-$(DMET)_2AuBr_2$	1.9	61
α-$(TTF)[Pd(dmit)_2]_2$	1.7 (22kbar)	62
$(TTF)[Ni(dmit)_2]_2$	1.62 (7kbar)	63
$(BEDO\text{-}TTF)_3Cu_2(NCS)_3$	1.1	64
$(DMET)_2AuCl_2$	0.83	65
$(DMET)_2Au(CN)_2$	0.8 (5kbar)	66
$(DMET)_2IBr_2$	0.59	67
$(DMET)_2AuI_2$	0.55 (5kbar)	68
$(DMET)_2I_3$	0.47	69

Table 1.4 A summary of non BEDT-TTF organic superconductors.

1.3 Theoretical aspects of magnetism and superconductivity.

1.3.1 Magnetism

Within a lattice, there are many ways in which the unpaired electrons can orientate themselves with respect to each other. The following sections will briefly mention some different types of magnetism and this will be expanded to give a theoretical description of the magnetism observed within this research project.

1.3.1.1 Paramagnetism

Paramagnetism occurs when there is no interaction between the unpaired spins within the lattice. Consequently the spins are randomly aligned with respect to each other. Curie made the empirical observation that the susceptibility of paramagnetic samples is inversely proportional to temperature. Hence, the Curie Law states:

$$\chi_{(molar)} = C/T \qquad eq.1.1$$

where $\chi_{(molar)}$ represents the molar susceptibility, C is the Curie constant, and T is the temperature. This equation implies that a plot of $1/\chi$ versus temperature should result in a straight line passing through the origin with a slope of 1/C. However, Weiss noted that this is not always the case and hence the Curie Law has been modified to the Curie Weiss Law.

$$\chi_{(molar)} = C/(T-\theta) \qquad eq.\ 1.2$$

where θ, the Weiss constant, is the value at which the straight line crosses the x axis and hence has units of temperature. The value of θ also acts as an indication of the type of interaction present within the material, if any. Negative values are indicative of

an antiferromagnetic interaction whereas positive values suggest that there is a ferromagnetic interaction (see section 1.3.1.3).

A more sophisticated derivation of the Curie Law is presented below which is a lot more quantitative in its' approach.

If an atom with a magnetic moment μ is placed in a magnetic field, H, the moment will align itself with the field to reduce the interaction energy.

$$E = \mu . H \qquad \textit{eq. 1.3}$$

Alignment to the field is restricted however by thermal vibrations and thus the magnetisation (M) of the sample must involve a thermal parameter:

$$M = N\mu\overline{cos\theta} \qquad \textit{eq. 1.4}$$

where $\overline{\cos\ \theta}$ is the average value at thermal equilibrium and N is the Avagadro number. Assuming a Boltzmann Distribution, the probability of finding an atom with its magnetic moment making an angle between θ and $\theta + d\theta$ (or solid angle $d\Omega$) is given by:

$$cos\theta = \int exp\ (\ -E/kT)\ \overline{cos\theta}\ d\Omega \,/ \int exp\ (\ -E/kT)\ d\Omega \qquad \textit{eq. 1.5}$$

Integrating over all directions and substituting in equation 1.3 gives:

$$cos\theta = \int 2\pi\ exp\ (\ -\mu H\overline{cos\theta}/kT)\ \overline{sin\theta cos\theta}\ d\theta \,/ \int 2\pi\ exp\ (\ -\mu H\overline{cos\theta}/kT)\ \overline{sin\theta}\ d\theta$$

eq. 1.6

which has a solution of :

$$cos\theta = ctnhx - 1/x \qquad eq.\ 1.7$$

$$= L(x)$$

where L(x) is the Langevin function and x = μH/ kT.

Therefore:

$$M = N\mu\ (ctnh\ \mu H/ kT - kT/ \mu H) \qquad eq.\ 1.8$$

The expansion of ctnh (x) is:

$$ctnh\ (x) = 1/x + x/3 - x^3/45 + 7x^5/ 2160..... \qquad eq.\ 1.9$$

By considering the region in which mH << kT, this can be simplified to:

$$M = N\mu^2 H/ 3kT \qquad eq.\ 1.10$$

or $$\chi = N\mu^2/ 3kT \qquad eq.\ 1.11$$

Substituting in the spin only formula for a moment, $\mu = -g\mu_B\sqrt{S(S+1)}$ gives:

$$\chi = Ng^2\mu_B^2 S(S+1)/3kT \qquad eq.\ 1.12$$

and removing the constants from the equation leaves:

$$\chi = C/T$$

where C, the Curie constant is equal to $Ng^2\mu_B^2S(S+1)/3k$.

The Curie constant simplifies to:

$$C = 0.125g^2S(S+1)\ cm^3K/mol \qquad eq.\ 1.13$$

and assuming g = 2

$$2C = S(S+1) \qquad eq.\ 1.14$$

Table 1.5 summarises the expected values for the Curie constant and Bohr magneton for systems where S = 1/2, 1, 3/2, 2 and 5/2 assuming that g = 2.

Number of unpaired spins	C ($emuKmol^{-1}$)	μ_s
1	0.375	1.73
2	1	2.83
3	1.875	3.87
4	3	4.90
5	4.375	5.92

Table 1.5 Expected values of the Curie constant for systems with 1, 2, 3, 4 and 5 unpaired spins.

1.3.1.2 Magnetisation

At very low temperatures, there is a minimal amount of thermal agitation within the system. Therefore, when a field is applied the unpaired electrons will tend to align themselves to the field. Initially, as the field is increased, the magnetisation of the sample will increase linearly with the field. However, this can only happen up to a limit as there are only a given number of spins within the system. Hence, there is a

limit in which the magnetisation will saturate. This is defined in terms of a Brillouin function which is derived below.

The energy levels of a system in a magnetic field are:

$$E = m_J g \mu_B H \qquad \textit{eq. 1.15}$$

where m_J is the magnetic quantum number.

Assuming that the system consists of a single spin with no orbital moment, $m_J = \pm 1/2$ and $g = 2$:

$$E = \pm \mu_B H \qquad \textit{eq. 1.16}$$

Therefore two energy levels are generated and the occupation of these levels is governed by the Boltzmann Distribution:

$$N_1/N = exp\,(\mu_B H/kT) \,/\, exp\,(\mu_B H/kT) + exp(-\mu_B H/kT) \qquad \textit{eq. 1.17}$$

$$N_2/N = exp\,(-\mu_B H/kT) \,/\, exp\,(\mu_B H/kT) + exp(-\mu_B H/kT) \qquad \textit{eq. 1.18}$$

The resultant magnetisation of N atoms per unit volume is thus:

$$M = (N_1 - N_2)\mu = N\mu\,(exp\,(x) - exp\,(-x)) \,/\, (exp\,(x) + exp\,(-x)) \qquad \textit{eq. 1.19}$$

where $x = \mu_B H/kT$

Therefore:

$$M = N\mu tanhx \qquad \textit{eq. 1.20}$$

In a magnetic field an atom with a moment J has 2J+1 equally spaced energy levels.

The magnetisation can now be expressed as:

$$M = NgJ\mu_B B_J(x) \qquad \textit{eq. 1.21}$$

where $x = gJ\mu_B H/kT$

and $B_J = 2J+1/2J \coth ((2J+1)x/2J) - 1/2J \coth (x/2J)$

The theoretical values for J = 1/2, 1, 3/2, 2 and 5/2 are plotted in Figure 1.4.

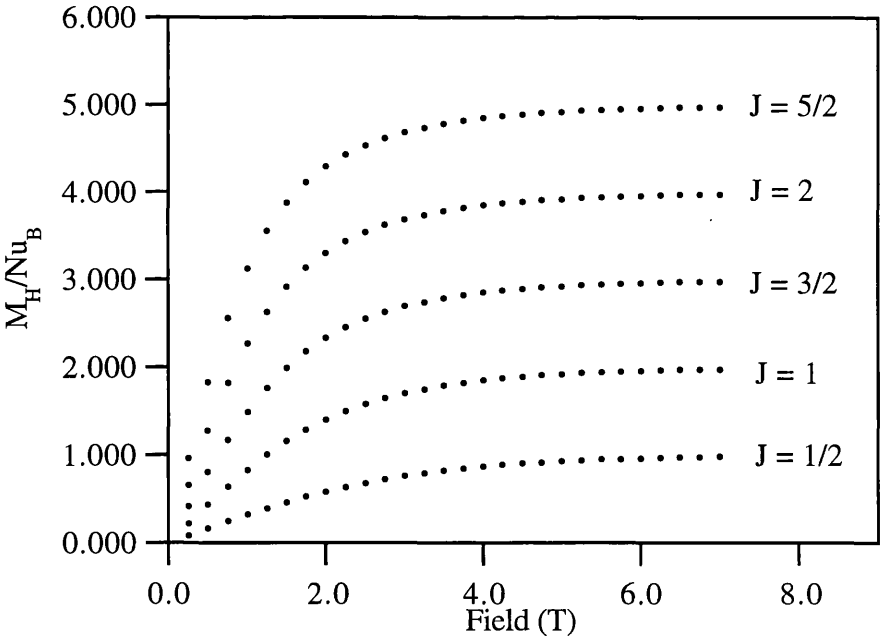

Figure 1.4 The theoretical Brillouin functions for J = 1/2, 1, 3/2, 2 and 5/2.

1.3.1.3 Ferromagnetism and Antiferromagnetism

Ferromagnetism occurs when the adjacent spins within the lattice align themselves parallel with respect to each other.

At high temperatures, the spins are usually randomly oriented. However, when the lattice is cooled, the spins may start to 'see' each other and consequently align themselves. Ferromagnetic alignment can be observed by measuring the magnetic susceptibility versus temperature and at the ordering temperature, the Curie temperature, there will be a sharp rise in the susceptibility. At temperatures greater than the Curie temperature, the system will obey the Curie Weiss law. However, beneath this temperature, other models must be used to represent the ordering.

Antiferromagnetism can be considered to be the opposite of ferromagnetism. That is the adjacent spins orientate themselves antiparrallel with respect to each other.

Again this ordering will happen at a specific temperature, the Néel temperature, as the material is cooled. An antiferromagnetic transition can be observed by measuring the magnetic susceptibility versus temperature and at the Néel temperature, there will be a decrease in the susceptibility. The extent of this decrease will depend upon how the crystals are aligned with the magnetic field. The susceptibility of a crystal with the easy axis aligned parallel to the field will go to zero, whereas if the easy axis is perpendicular to the field, the susceptibility will tend towards the maximum observed susceptibility, which is given a nominal value of 1. On a randomly oriented polycrystalline sample (or a powder), the susceptibility will be an average of these two values, with two contributions from $\chi_{\text{perpendicular}}$ and one contribution from χ_{parallel}. Therefore, the susceptibility will tend towards 2/3 of the maximum susceptibility. Again at temperatures higher than the Néel temperature, the systems obey the Curie Weiss Law. However, beneath this temperature, other models must be used.

These models depend upon the anisotropy of the magnetic order. If they order in one dimension, the Ising model is used; in two dimensions (i.e. in a plane) the XY model is employed and if the moment orders in three dimensions, the Heisenberg model is applied. As this is not relevant to the current text the interested reader is guided to the literature cited in the Bibliography for a fuller explanation.

1.3.1.4 Diamagnetism

All materials show temperature independent diamagnetism as a consequence of the closed electronic shells at a lower energy than the electrons near the Fermi level. The magnitude of this term is dependent upon the atom or ion present and some of these values have been determined experimentally. This idea was first postulated by Pascal and hence they are called Pascal's constants. In order to determine the value of diamagnetism in a molecule, the Pascals constants of the constituent moieties are added together. The values which are relevant to this thesis are given in Table 1.6

Molecule	Pascal's constant ($*10^{-6}$ emu/mol)
BEDT-TTF	-187
$Fe(C_2O_4)_3^{3-}$	-85
$Cr(C_2O_4)_3^{3-}$	-86
$Fe(C_2O_2S_2)_3^{3-}$	-121
K^+	-14.9
NH_4^+	-13.3
H_2O	-13
C_6H_5CN	-85

Table 1.6. Pascals constants for materials relevant to this thesis.

The value for BEDT-TTF is a collective average of values given in the literature and the other values were obtained from the excellent texts by Carlin and Kahn which are cited in the Bibliography.

1.3.1.5 Pauli paramagnetism

In a metal the conduction electrons are delocalised throughout the solid. In the absence of a magnetic field, there will be an equal amount of spin up and spin down electrons. However, when a field is applied, more spins will align themselves to the field and hence there will be a positive susceptibility. This value is temperature independent and can be quantified by the following equation:

$$\chi_{(Pauli)} = 2\mu_B^2 N(E_F) \qquad eq.\ 1.22$$

where μ_B is the Bohr magneton and $N(E_F)$ is the density of states at the Fermi level (see section 1.3.2.1).

1.3.1.6 Magnetisation of dimer pairs

If two ions, A and B, each have one spin which interact with each other, the quantum numbers are S = 0 (singlet state) and S = 1 (triplet state). These two spin pair states will be of a different energy and are thus separated by an energy gap, J.

$$J = E\ (S = 0) - E\ (S = 1)$$

It is not obvious which one of these two states will be the Ground State. It has been shown in cases where E (S = 0) is the Ground State, the interaction will be antiferromagnetic and J will be negative. However, when E (S = 1) is the Ground State, the interaction will be ferromagnetic and J will be positive.

The energy required to promote an electron from E (S = 0) to E (S = 1) is given as -J. This is the energy which transforms a singlet state into a triplet state hence changing the susceptibility of the system.

This type of situation is common in Copper (II) dinuclear compounds and an expression relating the susceptibility to J was derived by Bleaney and Bowers [70]:

$$\chi_{(molar)} = 2Ng^2\mu_B^2 / \{kT[\ 3 + exp\ (-2J/kT)]\} \qquad eq.\ 1.23$$

1.3.2 The Electronic Structure of Solids.

1.3.2.1 Bloch Functions

In the solid state, rather than considering the combination of just two atomic orbitals to form a molecular orbital, the combination of N unit cells, where N is approximately the Avagadro number, must be considered. To solve such a problem would involve huge amounts of computer time, but this is alleviated by utilising the translational symmetry of crystals.

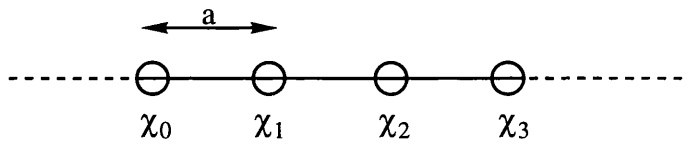

Figure 1.5 A one dimensional lattice.

Figure 1.5 illustrates a lattice with points 0, 1, 2, 3... and at each lattice point, there is an atomic orbital $\chi_0, \chi_1, \chi_2, \chi_3$....These orbitals can be combined (LCAO) by employing a Bloch Function:

$$\Psi_k = \sum e^{\,ikna}\,\chi_n \qquad eq.\ 1.24$$

where a is the lattice spacing between the sites and **k** is a wavevector, which is defined below.

Electrons travelling through a crystal are mathematically expressed as waves, which are normally expressed in terms of frequency and wavelength. However, in the solid state, it is usual to express the waves in terms of a wavevector, **k**. It is related to the wavelength, λ by the following equation:

$$\mathbf{k} = 2\pi / \lambda \qquad \textit{eq. 1.25}$$

Therefore, **k** space is the reciprocal of normal space. The combination of two wavevectors, $\mathbf{k}_1$ and $\mathbf{k}_2$ has the resultant wavevector of $\mathbf{k}_1 + \mathbf{k}_2$.

By employing the Bloch function for a one dimensional chain of s orbitals, the variation of E with **k** can be easily observed:

$\mathbf{k} = 0$ $\qquad \Psi_0 = \sum e^{0}\chi_n \quad = \chi_0 + \chi_1 + \chi_2 + \chi_3 + \chi_4 \ldots\ldots$

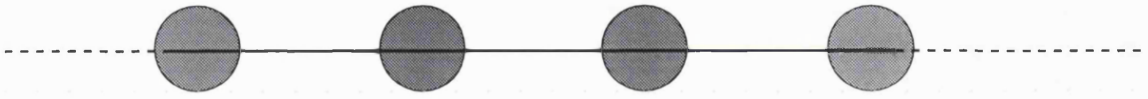

$\mathbf{k} = \pi/a$ $\qquad \Psi_{\pi/a} = \sum e^{\pi i n}\chi_n \quad = \chi_0 - \chi_1 + \chi_2 - \chi_3 + \chi_4 \ldots\ldots$

Therefore, there is an increase in energy from going from $\mathbf{k} = 0$ to $\mathbf{k} = \pi/a$.

However, in the case of a one dimensional chain of p orbitals, we have:

at $\mathbf{k} = 0$

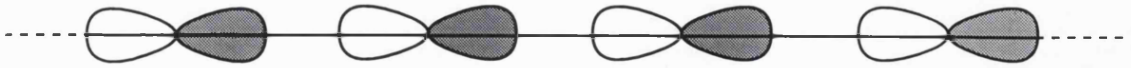

and at $\mathbf{k} = \pi/a$

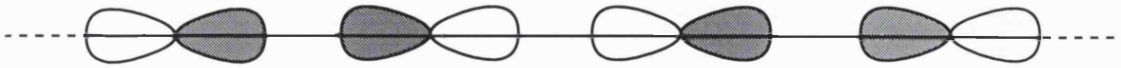

and therefore, there is a decrease in energy in going from $\mathbf{k} = 0$ to $\mathbf{k} = \pi/a$. Hence, the energy dispersion of an electronic band is dependent upon the topology of the participating orbitals.

A further point to address is the dispersion of the energy bands between the zone centre and the zone edge. This is determined by the overlap of the participating orbitals and in general, the greater the overlap, the greater the dispersion. Therefore, the band width can be increased with the application of pressure on the solid. This would in turn change the concentration of electronic states within a given energy interval, an entity which is known as the *Density of States*. It is defined as being the number of energy levels between E to E + dE and is calculated by integrating the band structure. In general, the flatter the energy band, the greater the density of states.

The energy dispersions for the one dimensional s and p orbitals are plotted in Figures 1.6 and 1.7 respectively.

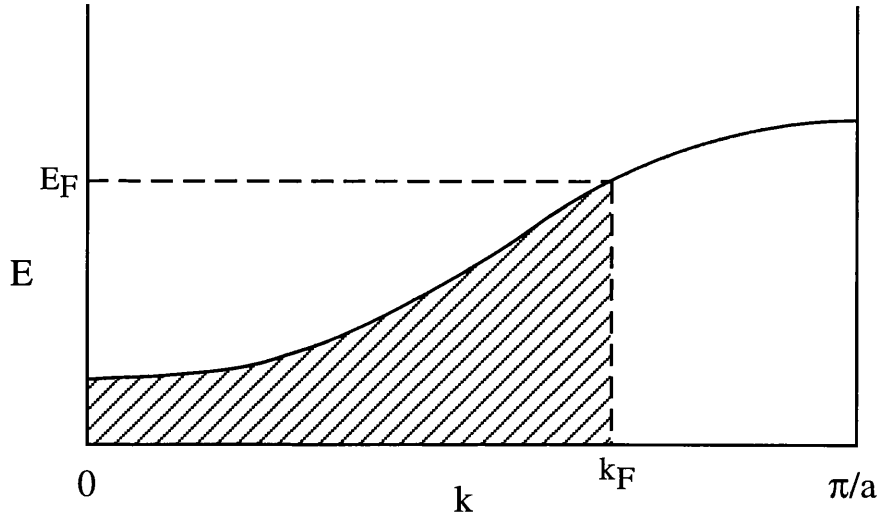

Figure 1.6 The dispersion of an energy band for one dimensional s orbitals.

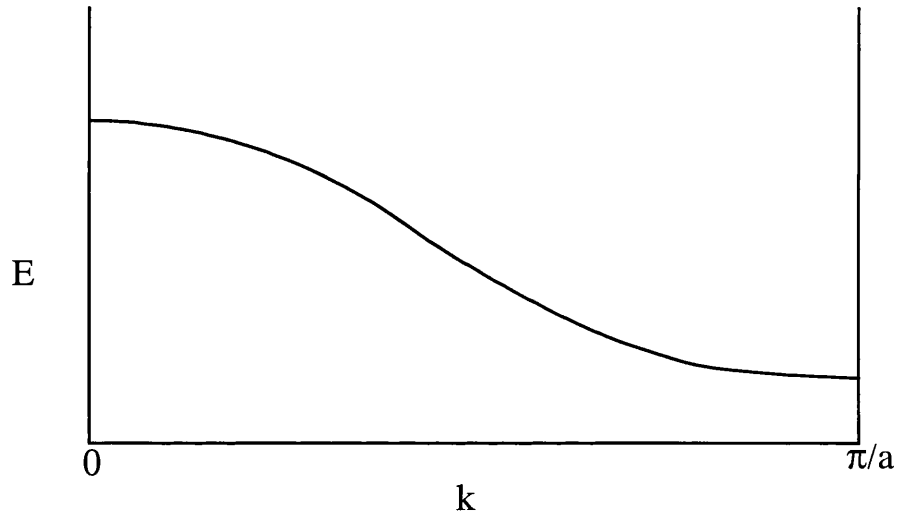

Figure 1.7 The dispersion of an energy band for one dimensional p orbitals.

The filling of these energy levels is critical to the electronic properties of the solid. Electrons will begin to fill an energy band at the point of lowest energy and will continue to do so until:

1) There are no more electrons.

2) The band is full in which case they will begin to fill the next highest energy band.

The highest occupied energy level within an energy band at 0K which is occupied by an electron is the *Fermi Level, E_F.* and the value of **k** which corresponds to E_F is the *Fermi wavevector, k_F* (see Figure 1.11). If the Fermi level cuts an energy band, metallic behaviour will be observed.

In order to examine the band structure at the Fermi level, special points of the Brillouin zone (section 1.3.2.5) are designated in order to reduce it to a two dimensional picture. This is known as the *Fermi Surface*. The points of interest are represented by the labels Γ, X, Y and M which have general co-ordinates of (k_x, k_y). Γ is the zone centre and hence has the co-ordinates (0, 0); X is (π/a, 0); Y is (0, π/a); and M is the midpoint which has co-ordinates of (π/a, π/a).

1.3.2.2 Brillouin Zones and k space

A Brillouin Zone is a Wigner - Seitz cell in reciprocal space. Therefore, a description of the construction of a Wigner - Seitz cell will be given followed by a discussion on the construction and significance of a Brillouin Zone.

A Wigner - Seitz cell is a primitive cell. It is constructed by joining together lattice points to nearby lattice points. At the midpoint and perpendicular to these lines, a new line is drawn, and where these lines bisect each other, a volume is enclosed, which is the Wigner - Seitz cell.

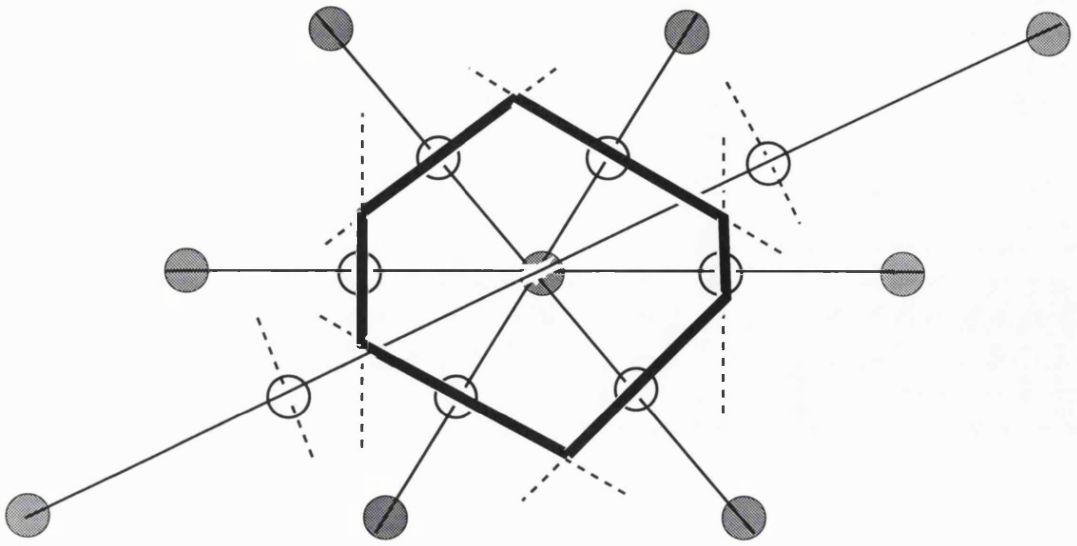

Figure 1.8. The construction of a Wigner - Seitz cell.

The lattice points are represented by the shaded circles and the midpoint between lattice sites is represented by open circles. The dashed lines are drawn perpendicular to the lines joining together the lattice sites.

A Brillouin Zone is constructed in the same way, only using the lattice points of the reciprocal lattice instead of those of the real lattice. The significance of a Brillouin Zone in the solid state is huge, as all Bloch sums of the atomic orbitals are generated without repetition. A proof of this is given below.

The LCAO coefficient for an atom n with a lattice spacing a is defined as:

$$c_n(k) = exp(ikna) \qquad eq.\ 1.26$$

Let g equal a multiple of $2\pi/a$

$$g = 2p\pi/a\ ;\ p = 0; \pm1; \pm2\ ....$$

Therefore:

$$c_n(k+g) = exp(inka + i2pn\pi) \qquad eq.\ 1.27$$
$$= c_n(k)$$

Hence, if **k** has a range of $2\pi/a$, all distinct values of c_n (k) can be generated. Thus, by spanning $-\pi/a$ to π/a all values of **k** are considered. This area is known as the First Brillouin Zone.

1.3.2.3 The Dimensionality of the Fermi Surface.

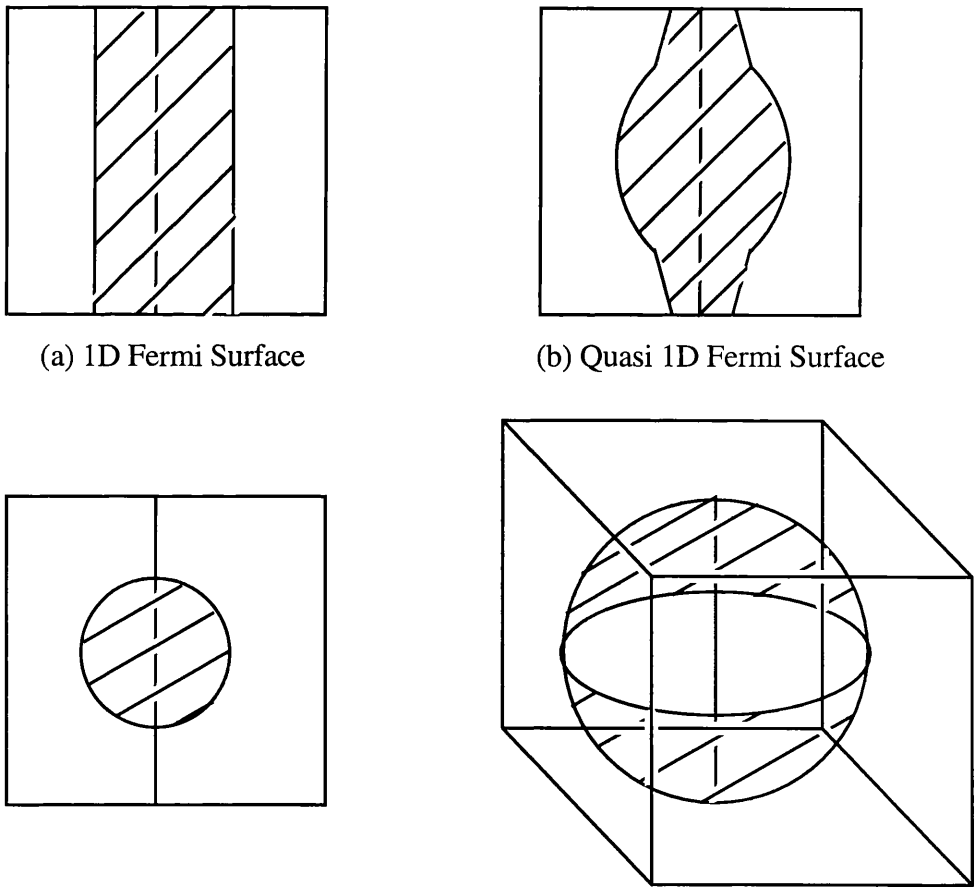

(a) 1D Fermi Surface (b) Quasi 1D Fermi Surface

(c) 2D Fermi Surface (d) 3D Fermi Surface

Figure 1.9 The Fermi surfaces of one dimensional, quasi one dimensional, two dimensional and three dimensional systems.

Figure 1.9(a) is a diagram of an idealised one dimensional Fermi Surface. However, in real materials, there will always be interactions in the other directions (albeit small) and therefore quasi 1D behaviour is observed. Examples of quasi 1D systems (Figure 1.9(b)) are observed in the charge transfer salts of TMTSF. The electrical transport is predominately along the stacking axis of the TMTSF molecules and therefore the Fermi Surface is one dimensional in nature. There are however slight interactions in other directions and hence quasi 1D behaviour is observed.

Two dimensional behaviour (Figure 1.9(c)) is reported in metallic BEDT-TTF salts and an extended discussion of this will follow in section 1.3.2.4. The BEDT-TTF layer consists of a plane of organic molecules whose chalcogenide orbitals overlap in both directions. Hence, the electrical transport is two dimensional in nature.

Three dimensional Fermi Surfaces are observed in the simple metals, like for example Copper. Electronic interactions occur in all directions and hence the anisotropy of the electrical behaviour is limited.

1.3.2.4 Band Structure Calculations

In order to simplify the problem, a three dimensional orthorhombic lattice is considered with lattice parameters of a, b and c. The position of each lattice site is defined by the co-ordinates m, n and p and a single orbital χ occupies each site. The orbital at the origin is defined as χ_{000} and its nearest neighbours are defined as χ_{100}, χ_{010} and χ_{001} respectively. The allowed energy levels which the lattice can have are given by the Bloch orbitals:

$$\phi\,(k_a, k_b, k_c) = N^{-1/2} \sum\sum\sum \exp(i\mathbf{k}_a ma)\exp(i\mathbf{k}_b nb)\exp(i\mathbf{k}_c pc)\chi_{mnp} \qquad \textit{eq. 1.28}$$

where $\mathbf{k}_a$, $\mathbf{k}_b$ and $\mathbf{k}_c$ are wavevectors along the a, b and c directions respectively and the exponential terms define the coefficients for the site orbital χ_{mnp}. It is only necessary to consider the wavevectors within the first Brillouin Zone. i. e.

$$-\pi/a \leq k_a \leq \pi/a$$

$$-\pi/b \leq k_b \leq \pi/b$$

$$-\pi/c \leq k_c \leq \pi/c$$

The energies of the Bloch orbitals can now be expressed as:

$$E(k_a, k_b, k_c) = \frac{< \phi\,(k_a, k_b, k_c) | H^{eff} | \phi\,(k_a, k_b, k_c) >}{\phi\,(k_a, k_b, k_c) \mid \phi\,(k_a, k_b, k_c)} \qquad \textit{eq. 1.29}$$

where H^{eff} is the effective Hamiltonian.

Assuming that the only interactions of interest are between nearest neighbours, equation 1.29 can be re - written as:

$$E(k_a, k_b, k_c) = \frac{\alpha + 2\,(\beta_a \cos k_a a + \beta_b \cos k_b b + \beta c \cos k_c c)}{1 + 2\,(S_a \cos k_a a + S_b \cos k_b b + S_c \cos k_c c)} \qquad \textit{eq. 1.30}$$

where:

$$S_a = < \chi_{000} \mid \chi_{100} > \qquad \alpha = < \chi_{000} \mid H^{eff} \mid \chi_{000} >$$

$$S_b = < \chi_{000} \mid \chi_{010} > \qquad \beta_a = < \chi_{000} \mid H^{eff} \mid \chi_{100} >$$

$$S_c = < \chi_{000} \mid \chi_{001} > \qquad \beta_b = < \chi_{000} \mid H^{eff} \mid \chi_{010} >$$

$$\beta_c = < \chi_{000} \mid H^{eff} \mid \chi_{001} >$$

and S_x are the nearest neighbour overlap integrals, α is the Coulomb integral and β_x are the nearest neighbour hopping integrals in the respective directions.

In going from one orbital per site to many orbitals per site, the total wavefunction at the lattice site must be considered and hence equation 1.29 becomes:

$$E_i(k) = \frac{< \Psi_i(\mathbf{k}) \mid H^{eff} \mid \Psi_i(\mathbf{k})>}{< \Psi_i(\mathbf{k}) \mid \Psi_i\,(\mathbf{k})>} \qquad \textit{eq. 1.31}$$

In this theory, the atomic orbital basis consists of all of the valence atomic orbitals of the constituent atoms. The Coulomb integrals (α) are taken as being the ionisation potential of the respective atom.

1.3.2.5 Fermi Surfaces of BEDT-TTF Superconductors

The multiphasic packing of BEDT-TTF charge transfer salts has already been discussed in section 1.2.3.2. Despite all of these packing motifs, the BEDT-TTF molecules normally pack in a two dimensional array and a highly conducting layer is formed as a result of the intermolecular S - S Van der Waals interactions. Consequently, band structures of BEDT-TTF salts exhibit predominately two dimensional character. Perpendicular to the conducting planes, there is a very limited dispersion in the E(k) versus k diagram and hence, nearly cylindrical Fermi surfaces are formed and therefore, the electrons move in a closed orbit.

A discussion of the Fermi surfaces of two well known BEDT-TTF superconductors, κ-(BEDT-TTF)$_2$Cu(NCS)$_2$ and β-(BEDT-TTF)$_2$I$_3$, will follow, which will confirm the two dimensional nature of two superconductors which have different packing motifs. It is interesting to note that the theoretical predictions from band structure calculations are confirmed by high field magnetoresistance measurements, with the observation of Shubnikov de Haas oscillations. However, it is beyond the scope of

this thesis to discuss the physics of superconductors and hence this discussion will be limited to the Fermi Surfaces derived from band structure calculations.

The band structure of κ- (BEDT-TTF)$_2$Cu(NCS)$_2$ has been reported by many authors and has been the focal point of much research on the Fermiology of organic superconductors [71]. In this salt, there are two independent BEDT-TTF molecules, which restricts the accuracy of the calculation as they are assumed to be equivalent. However, the results obtained are in good agreement with experiment. The calculation predicts that energy bands will cross the Fermi level between Γ - Y, M - Z and Z - Γ. This results in a Fermi surface comprising of closed orbits of overlapping circles which is characteristic of a two dimensional metal. It is interesting to note that this type of Fermi surface has also been predicted for other κ - phase organic superconductors (e.g. κ-(BEDT-TTF)$_2$I$_3$)

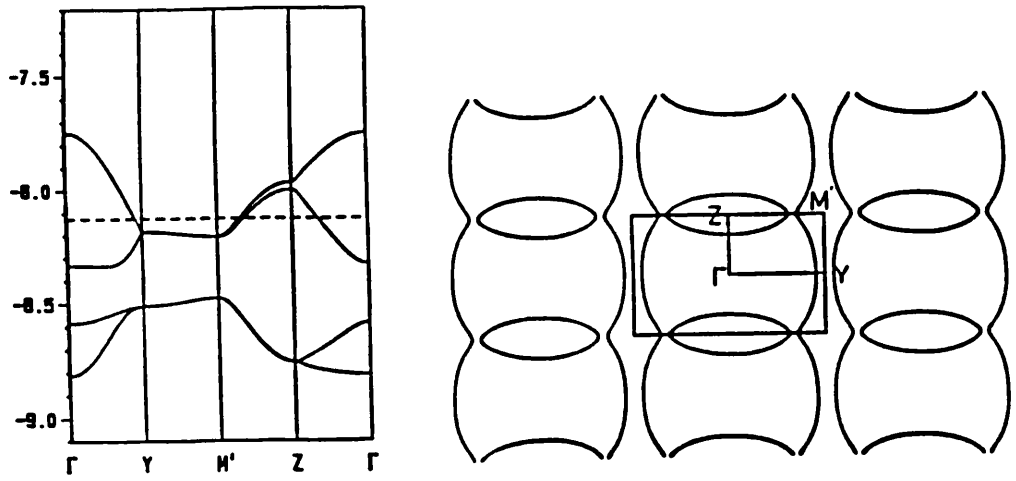

Figure 1.10 The band structure of κ-(BEDT-TTF)$_2$Cu(NCS)$_2$. From reference 71.

The band structure of β - (BEDT-TTF)$_2$I$_3$ also shows how the Fermi level is crossed by an energy band [72]. The crossing occurs between Γ - X and Y - Γ which results in a Fermi surface resembling a Rugby ball. This closed orbit is again representative of

two dimensional metallic behaviour. The band structure of β' - $(BEDT\text{-}TTF)_2I_3$ is very similar to that calculated for the β phase salt, indicating little change in the predicted electrical properties of the two salts. Both of these materials become superconducting with T_c's of 1.4 and 8K for the β and β' phases respectively.

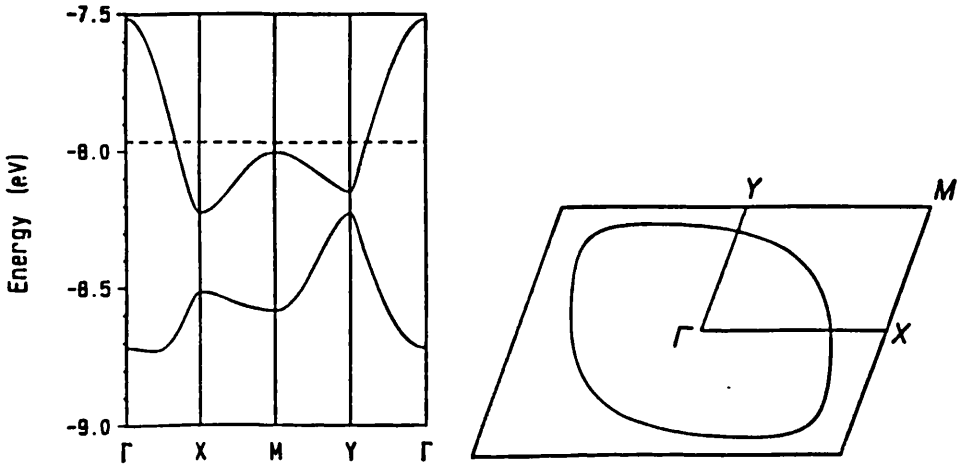

Figure 1.11 The band structure of β-$(BEDT\text{-}TTF)_2I_3$. From reference 72.

1.3.3 Superconductivity.

1.3.3.1 BCS Theory.

At low temperatures, the dominant feature causing resistance is scattering of electrons arising from impurity atoms and lattice defects. These impurities will always be present and hence the resistance cannot be zero within the quasi free electron model. Therefore, a completely new model needed to be developed in order to explain superconductivity.

The accepted theory of superconductivity was postulated by Bardeen, Cooper and Schreiffer in 1957 [73]. They give a detailed quantum mechanical description of the

superconducting state and account for the physical properties which arise from it. Many texts give a detailed explanation of this theory. Here, a simplified qualitative description will be presented.

Cooper demonstrated in 1956 that it is energetically favourable for electrons to pair up. The Coulombic repulsion between two electrons is overcome by a subtle interaction with the lattice which can be explained qualitatively in the following manner. As an electron travels through a lattice, there will be a momentary attraction to an ion which slightly distorts the lattice allowing a second electron nearby to be attracted to the same ion. Hence there is an electron - phonon - electron interaction. Cooper showed that this would be the ground state of a system at 0K and hence the electron pairs are known as *Cooper Pairs.*

In terms of wavevectors, the interaction can be expressed as follows. An electron with momentum $\mathbf{k}_1$ will be attracted to an ion, creating a virtual phonon, $\mathbf{q}$. A second electron with momentum $\mathbf{k}_2$ will also interact with the same virtual phonon. Thus:

$$\mathbf{k}_1 - \mathbf{q} = \mathbf{k}_1' \quad \text{and} \quad \mathbf{k}_2 + \mathbf{q} = \mathbf{k}_2' \qquad \textit{eq. 1.32}$$

Therefore:

$$\mathbf{k}_1 + \mathbf{k}_2 = \mathbf{k}_1' + \mathbf{k}_2' \qquad \textit{eq. 1.33}$$

and the net wavevector of the electron pair remains constant.

It has been demonstrated that the most likely pairing consists of electrons with equal and opposite wavevectors. (i.e. $+\mathbf{k}\uparrow$ and $-\mathbf{k}\downarrow$). The value of $\mathbf{k}$ in every pair is therefore zero and hence there is no net momentum. In order for current to be passed, a current must be applied so that:

$(\mathbf{k} + \delta)\uparrow$ and $(-\mathbf{k} + \delta)\downarrow$

Cooper Pairs will begin to form at T_c. As temperature is lowered, more pairs are formed until at 0K all possible electron pairs are formed. This still leaves unpaired electrons which are in the normal metallic state and thus there is an energy gap between the superconducting and the normal state electrons. This is given the value of 2Δ as each electron needs an energy Δ to be excited to the normal state. The energy associated with the impurity atoms is not great enough to scatter the electron pairs and hence a current travels unhindered throughout the lattice.

This theory thus predicts that a superconductor: will be a perfect diamagnet as it is a state which comprises of electron pairs with equal and opposite spins; there will be an energy gap at T_c between the superconducting and normal state electrons; and there will be a decrease in entropy as the system is becoming more ordered.

It also predicts the value of T_c through the following equation:

$$T_c = 1.14\ \theta\ exp\ [-1/\lambda\ D(E_F)] \qquad eq.\ 1.34$$

where θ is the Debye temperature, λ is the electron phonon interaction and $D(E_F)$ is the density of states at the Fermi level.

1.3.3.2 Type I and Type II Superconductors.

1.3.3.2.1 Type I Superconductors

A type I superconductor will expel a magnetic field up to a critical limit, which is denoted by H_c. At fields less then H_c, the material expels all of the magnetic flux and

remains superconducting. However, as soon as H_c is reached, the superconductivity is instantly destroyed, and the sample returns to the normal metallic state.

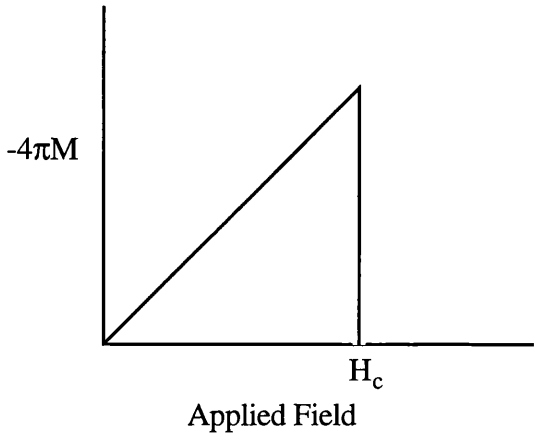

Figure 1.12 The magnetisation of a type I superconductor.

1.3.3.2.2 Type II Superconductors

A type II superconductor will expel a magnetic field up to a limit H_{c1}, at which point the field will begin to penetrate the superconductor, without destroying the superconductivity. As BCS theory predicts that a superconductor is a perfect diamagnet an explanation is required to explain how superconductivity and magnetism co-exist within the same sample. The accepted explanation is that the flux inside the sample results in parts of the sample being in the normal state. However, this is surrounded by the superconducting state and as a consequence, the superconducting current flows in vortices. Hence, this is known as the *vortex state.* The material will remain superconducting up to a second critical limit, H_{c2} where the superconductivity is destroyed.

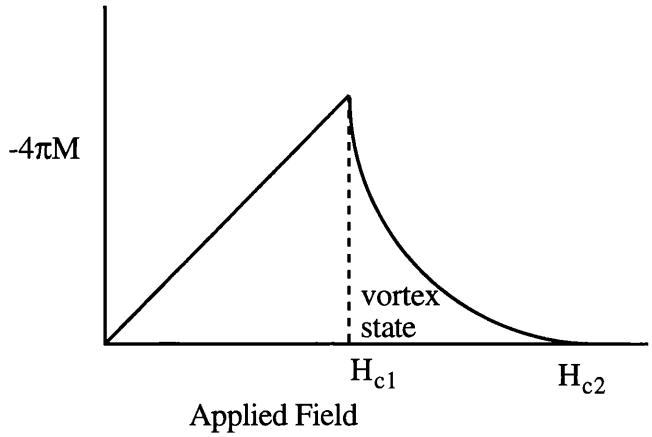

Figure 1.13 The magnetisation of a type II superconductor.

The difference between a type I and a type II superconductor, can be defined by two parameters, the coherence length (ξ) and the penetration depth (λ).

The coherence length, ξ of a superconductor is the distance within which the energy gap cannot change by a significant amount in a spatially varying magnetic field.

The penetration depth, λ is a measure of the distance which an applied magnetic field penetrates a superconducting sample.

The relationship between ξ and λ results in the two different types of behaviour. If $\lambda > \xi$, type I behaviour is evident and if $\xi > \lambda$, type II behaviour is observed.

1.3.3.3 The Meissner Effect.

If a type I superconductor is cooled in an applied field (which is less than the critical field) to below its' transition temperature, the lines of induction of the magnet will be expelled from the superconductor. This is a direct consequence of the electron pairing mechanism described by BCS theory and hence a superconductor behaves as a perfect diamagnet [74].

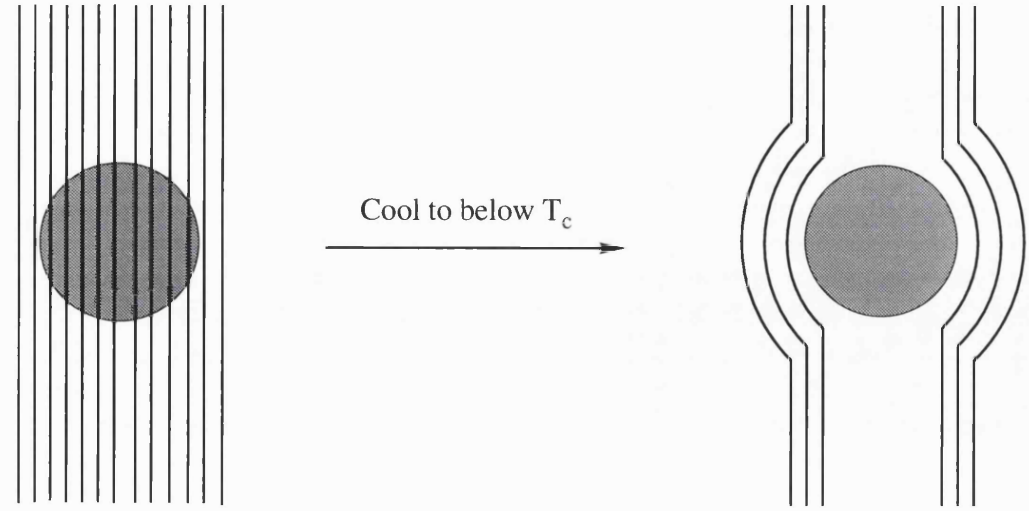

Figure 1.14 The Meissner Effect for a type I superconductor.

This can be detected by cooling the sample in zero field and measuring the susceptibility in an applied field whilst warming. The sample is then cooled in the same applied field and the susceptibility measured. Type I behaviour is observed when these two data sets are identical (Figure 1.15)

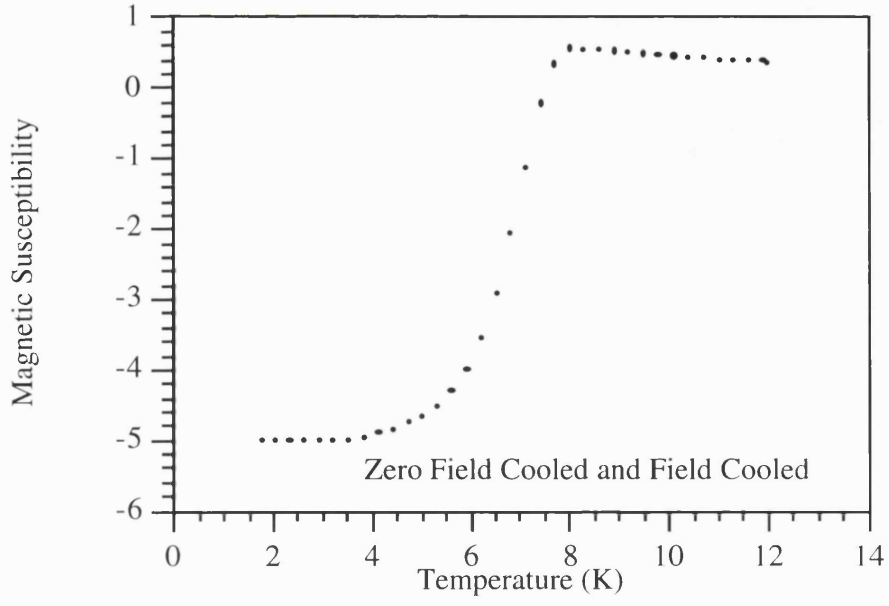

Figure 1.15 The Meissner Effect for a type I superconductor.

However, when a Type II superconductor is cooled in an applied field to below T_c, magnetic flux is trapped inside the sample. Therefore, the susceptibility of a Type II superconductor, will depend on whether it has been cooled in zero field or in an applied field. The difference between these two measurements is illustrated in Figure 1.16.

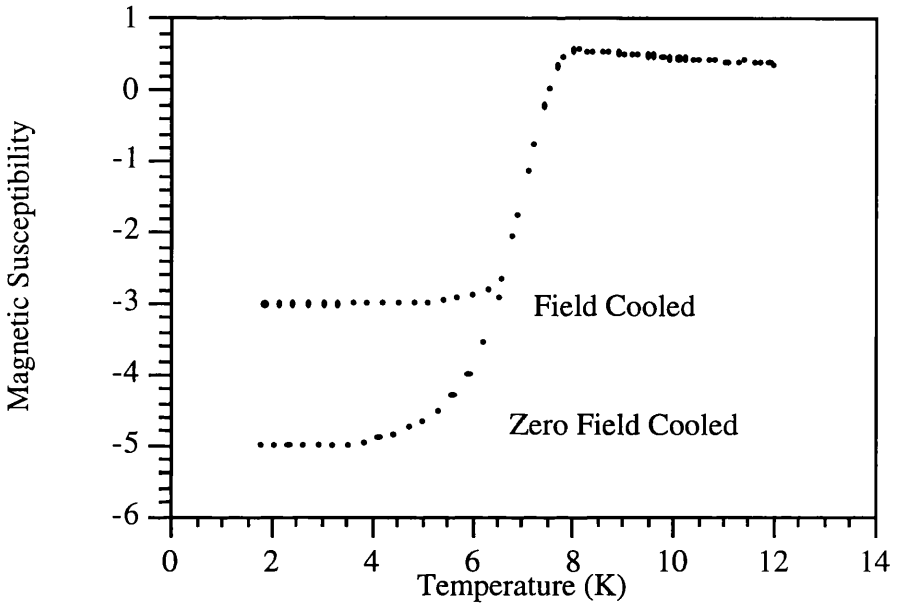

Figure 1.16 The difference in the magnetisation of a sample cooled in zero field and in an applied field, demonstrating the Meissner Effect observed in a Type II superconductor.

Cooling in zero field results in the superconductor acting as a perfect diamagnet and hence a large negative susceptibility is observed. However, when the same sample is cooled in an applied field, flux is trapped inside the sample and thus the susceptibility is less negative.

1.3.3.4 Magnetoresistance

The previous section has demonstrated how the application of a magnetic field destroys superconductivity at a critical value of H_c. At T_c, H_c will be zero. However, as temperature is lowered, the value of H_c increases. This increase is defined quantitatively in equation 1.32.

$$H_c = H_0 [\, 1 - (T/T_c)^2] \qquad eq.\ 1.35$$

where H_0 is the critical field at 0K.

A plot of H_c versus temperature for an arbitrary system is given in Figure 1.17

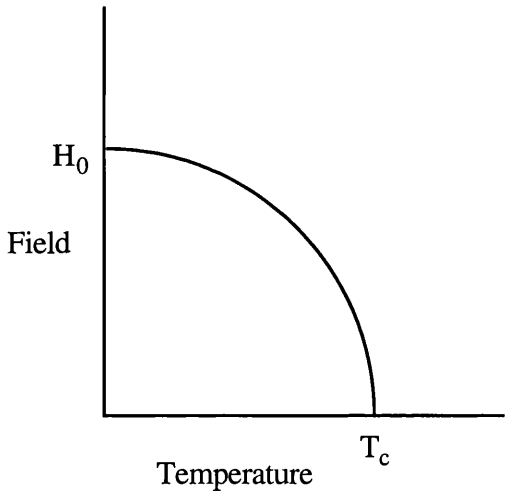

Figure 1.17 The critical field as a function of temperature for an arbitrary superconducting system.

1.4 Superconductivity and Magnetism

In the preceding sections, it has been the intention to illustrate that it is possible to observe the co - existence of superconductivity and magnetism in Type II superconductors. Magnetic flux is trapped inside the superconductor resulting in the

formation of the vortex state (section 1.3.3.2.2). However, there are examples where these two phenomena actually co - exist *within* the same compound. The superconductivity has arisen from a series of compounds, namely; $LnMo_6S_8$ [8]; $LnRh_4B_4$ [10]; LnM_3Si_5 (M = Ni or Fe) [12]; $LnNi_2B_2C$ [75]; and $LnBa_2Cu_3O_7$ [76]. The magnetic part of these materials though has always been accounted for by a rare earth ion. There is no interaction between the magnetic moments of the rare earth ions and thus they are paramagnets. The local field produced by the paramagnet is not great enough to destroy the superconductivity.

A beautiful example of the effect of magnetic interactions on superconducting properties is observed in $ErRh_4B_4$ [10]. The transition temperature to the superconducting state (8.5K) is higher than the magnetic ordering temperature (0.9K). Superconductivity is thus observed at 8.5K. However, as the sample is cooled to below the magnetic ordering temperature of 0.9K, the lattice becomes ferromagnetic resulting in the destruction of the superconductivity (Figure 1.18).

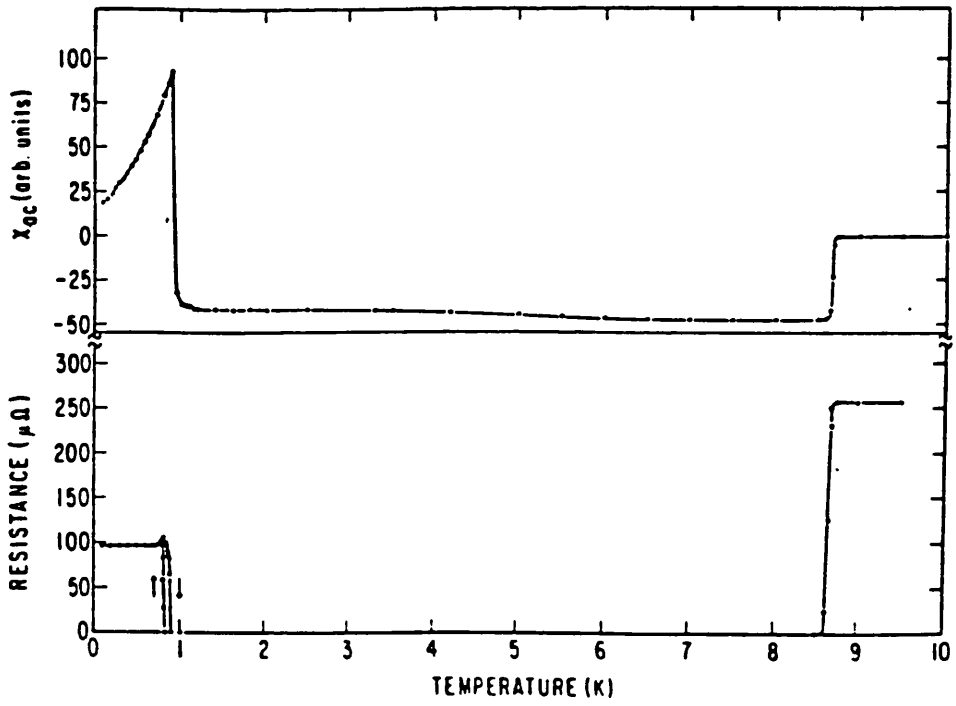

Figure 1.18 The electrical properties of $ErRh_4B_4$. Superconductivity is observed at 8.5K, but this is destroyed by the lattice becoming ferromagnetic at 0.9K.

A similar effect is also observed in $Ho_{1.2}Mo_6S_8$ [77] where the material becomes superconducting at 1.2K but returns to the normal state at 0.64K which is a consequence of ferromagnetic ordering.

Ferromagnetic ordering is not alone in destroying the superconducting state. Studies performed by Grigereit *et al* on $HoNiB_2C$ [78] revealed a superconducting transition at 7.5K but the superconductivity was destroyed as the sample was cooled to 5K. The destruction of the superconductivity was a consequence of antiferromagnetic ordering. However, when the sample was cooled even further, there was a rapid return to the superconducting state and it is claimed that both superconductivity and antiferromagnetism co - exist at temperatures lower than 5K.

1.5 Aims of Project

The aims of this research project can be categorised as follows:

1) To prepare a purely organic superconductor.
2) To prepare a compound in which both superconductivity and magnetism co - exist.
3) To engineer novel crystalline phases of BEDT-TTF charge transfer salts.
4) To increase the dimensionality of the conduction network.

The following paragraphs will give an explanation for the reasons why it is desirable to achieve each of the above aims and the strategies which were employed in order to realise these goals.

All of the organic superconductors known to date contain an inorganic complex as the charge compensating moiety. Band structure calculations indicate that the inorganic molecules are insulating and that the electrical transport occurs through the overlap of

the chalcogenide orbitals in the organic molecules. Despite this, a molecule has never been prepared in which both portions of the complex are organic.

In order to synthesise a purely organic superconductor, it is necessary to prepare a charge transfer salt with two organic moieties. The majority of superconducting organic phases contain the donor molecule BEDT-TTF and therefore a series of stable organic anions are required to form the charge transfer salts. The size, shape and charge of these anions are critical for the packing patterns observed in the BEDT-TTF layer, and hence it is desirable to keep these variables reasonably constant with known inorganic anions which form superconducting charge transfer salts with BEDT-TTF. Studies by Mori *et al* led to the discovery of superconductivity under applied hydrostatic pressure in $(BEDT\text{-}TTF)_4M(CN)_4.H_2O$ (M = Pt or Pd) [41, 44]. These were the only 4:1 organic superconductors reported, with square planar divalent anions.

In order to explore this type of system further, it would be necessary to prepare a series of organic compounds which have a similar size, shape and charge as the tetracyanometallate complexes, which can also be prepared in both hydrated and anhydrous forms. Therefore, it was one of the aims of this project to form superconducting charge transfer salts of BEDT-TTF with cyclobutadienyl (squarate) anions. A series of these anions are already known with O, S, NCN and $C(CN)_2$ functional groups attached. If a series of complexes with BEDT-TTF could be prepared, it would be possible to systematically vary the functional group (and water content) to investigate the effect on the electrical properties. Further to this, by considering the tetrathio complex, Sulfur 3p orbitals of a similar energy to those on BEDT-TTF will be introduced. Thus there is the possibility of increasing the dimensionality of the conduction network, which would surpress any lattice instabilities associated with low dimensional materials.

The co - existence of superconductivity and magnetism has been long sought after in organic charge transfer salts [79]. A pre - requisite for the co - existence of superconductivity and magnetism is to prepare a material in which the localised electrons on a metal centre do not interact with the conduction electrons. Further to this, the magnetic portion must not order at temperatures greater than the superconducting transition temperature, as this would destroy the superconductivity. Section 1.2.3.2 reports that the organic superconductors consist of segregated layers of donor and acceptor molecules and that the electrical properties of these compounds are accounted for by the organic layer. The anionic layer does not contribute to the states near the Fermi surface, and thus one or two dimensional behaviour is observed. Therefore, in this class of compounds, there is very little interaction between the donor and acceptor molecules and hence they offer a good possibility for discovering the co - existence of superconductivity and magnetism in molecular charge transfer salts. A sensible base to work from would be the organic donor molecule BEDT-TTF, as its ionic complexes have resulted in the formation of the majority of organic superconducting phases. In addition to this, the transition temperatures of these compounds to the superconducting state are appreciably higher than those observed in other organic systems. The second part of the equation is to introduce a magnetic material with non interacting localised moments, which obeys the Curie - Weiss law to very low temperatures. Therefore, it is desirable to study charge transfer salts of BEDT-TTF with well known paramagnetic anions. A series of compounds which will make this investigation possible are the metal tris oxalate systems. By varying the metal centre, the number of localised spins in the compound will vary without affecting the size, shape or charge of the anion. This will enable the effect of localised moments upon the electrical properties to be monitored systematically.

Further to this a series of compounds have been prepared with the general formula $AM(II)M(III)(C_2O_4)_3$ (A = organic cation, M = Fe, Cr or Mn) which possess interesting magnetic properties [80]. Their structures consist of the formation of

hexagonal arrays, in which the cavity of the honeycomb is occupied by the A cation. This situation is not dis-similar to the case reported for the superconducting κ-(BEDT-TTF)$_2$Cu(NCS)$_2$ salt, in which the organic molecules form orthogonally oriented dimer pairs. These pairs dock into the cavity of the anion layer created by the polymerisation of the Cu(NCS)$_2$ anion. Hence, the hexagonal array observed in oxalate materials offer a good possibility for preparing κ-phase materials.

Additionally, it also gives scope to replace the oxalate ligand with the dithiooxalate ligand, which will increase the size of the anion and also introduce sulfur atoms into the acceptor layer, which may increase the dimensionality of the conduction network. Another feature of the dithiooxalate system is that the magnetism of the iron complex changes from high spin Fe^{3+} to low spin Fe^{3+}.

Further to this, anions of this size, shape and charge have not been used in forming BEDT-TTF complexes so this may result in the formation of novel BEDT-TTF packing arrangements. A series of compounds have therefore been prepared with the general formula (BEDT-TTF)$_x$[M(C$_2$O$_4$)$_3$]$_y$ and the results obtained from these materials are the major scope of this thesis.

Chapter 2

Experimental : Synthesis and Physical Measurements.

2.1 Introduction

Literature methods were employed in the preparation of both bis(ethylene)dithiotetrathiafulvalene and the anions used to form the charge transfer salts. Some of these methods were slightly amended in order to obtain the desired starting material for the electrochemical synthesis.

A description of the electrocrystallisation technique is given in section 2.1.4. Here, it is suffice to say that the crystals were grown by applying a constant current between two platinum electrodes. Low currents were employed in order to minimise the rate of growth so that high quality single crystals could be obtained.

The following sections will describe the preparation of the anions used in this project, the preparation of BEDT-TTF and it will give a summary of the successes and failures in yielding charge transfer salts of the respective materials.

This will be followed by a section describing the theory and practicalities of the physical measurements employed to elucidate the properties of the charge transfer salts reported in this thesis.

2.2 Experimental Details

2.2.1 Preparation of BEDT-TTF [81]

Preparation of 2--oxo-1,4-dithiane (**1**) [7]

Ethanedithiol (102 cm^3), dichloromethane (1000cm^3) and triethylamine (336 cm^3) were added to a 3 litre round bottomed flask. The mixture was cooled to between 0-10 °C in an ice/ water/ acetone bath and argon was bubbled through. A solution of chloroacetyl chloride (96 cm^3) in dichloromethane was prepared and poured into a dropping funnel. This solution was added dropwise to the cooled mixture with rapid stirring. A thick white precipitate of triethylamine hydrochloride forms which was dissolved in ice/ water. The organic layer was separated and washed 4 times with water (200 cm^3 portions) and was left to dry over magnesium sulfate overnight. The drying agent was then filtered off and the solvent removed on a rotary evaporator. The product was isolated by vacuum distillation.

Preparation of 3-chloro-2-oxo-1,4-dithiane (**2**)

To a solution of **1** (2.5g) in carbon tetrachloride (40 cm^3), n-chloro succinimide (2.75g) was added. The mixture was stirred under argon for five minutes followed by heating under reflux for 30 minutes. It was then cooled in a refrigerator and the precipitated succinamide was separated by filtration. The solvent was removed on a rotary evaporator.

Preparation of 3-o-(2 propyl)dithiocarbamate-2-oxo-1,4-dithiane (**3**)

Potassium-o-(2-propyl) dithiocarbamate (3.28g) was suspended in dry acetone (75 cm^3) and **2** was filtered directly into the solution. The mixture was left to stir for 30 minutes and the solvent was then evaporated to leave a brown tar.

Preparation of 2-oxo-5,6-dihydro-1-3-dithiolo [4,5,6][1,4] dithiin (**4**)

Concentrated sulfuric acid (125 cm^3) was cooled to -10 °C in an ice/acetone bath. To the acid, dietylether (12.5 cm^3) was added dropwise. **3** was dissolved in a minimum amount of diethylether and added dropwise to the cold acid. This mixture was left to stir for 90 minutes before being slowly added to 750 cm^3 of ice/ water. It was then filtered through celite and the product allowed to crystallise from the filtrate over a period of 12 days. The product was recrystallised from ethanol.

Preparation of bis- (ethylene dithio) -tetrathia fulvalene (BEDT-TTF) (**5**)

Trimethyl phosphite was freshly distilled and **4** (0.55g) was suspended in the liquid. It was heated under reflux for 30 minutes in an inert atmosphere, after which time the precipitate had changed colour from yellow to red. The red crystals which precipitated were collected and recrystallised from chloroform.

Elemental Analysis / %

Calc. for $C_{10}H_8S_8$	C (31.23)	H (2.10)	N (0)	S (66.68)
Found	C (30.56)	H (2.06)	N (0)	S (66.28)

2.2.2 Preparation of Metal tris oxalates and dithiooxalates.

Preparation of potassium tris(oxalato)ferrate trihydrate [82]

Metal tris oxalato salts were prepared by the method described in reference 82 by Bailer and Jones, with the amendments described below in order to obtain the required salt. The products were recrystallised three times from water.

The corresponding ammonium salt was prepared by replacing the potassium and sodium oxalate for ammonium oxalate. Similarly, the sodium salt was prepared by replacing potassium oxalate for sodium oxalate. Anhydrous ammonium tris(oxalato)ferrate was obtained by drying the hydrated crystals in vacuo over P_2O_5.

Tetrabutylammonium salts were prepared by dissolving the alkali metal salts in water and adding a stoichiometric amount of tetrabutylammonium hydrogen sulfate in dichloromethane. The product was extracted into the organic layer, which is dried over $MgSO_4$. The drying agent is removed by filtration and the solvent evaporated to leave the product.

Elemental Analysis / %

$K_3Fe(C_2O_4)_3.3H_2O$

Calc.	C (14.67)	H (1.23)	N (0)
Found	C (14.50)	H (1.09)	N (0)

$(NH_4)_3Fe(C_2O_4)_3.3H_2O$

Calc.	C (16.79)	H (4.23)	N (9.81)
Found	C (17.00)	H (3.93)	N (9.94)

$Na_3Fe(C_2O_4)_3.3H_2O$

Calc.	C (16.27)	H (1.37)	N (0)
Found	C (16.00)	H (1.17)	N(0)

$[NBu_4]_3Fe(C_2O_4)_3$

Calc. for $C_{54}H_{108}O_{12}N_3Fe$	C (61.99)	H (10.40)	N (4.01)
Found	C (59.34)	H (10.52)	N (3.77)

Preparation of Potassium tris(oxalato)chromate trihydrate [82]

As of reference 82.

Elemental Analysis / %

Calc. for $C_6H_6O_{13}K_3Cr$	C (14.79)	H (1.24)	N(0)
Found	C (14.68)	H (1.02)	N (0)

$[NBu_4]_3Cr(C_2O_4)_3$

Calc. for $C_{54}H_{108}O_{12}N_3Cr$	C (62.22)	H (10.44)	N (4.03)
Found	C (60.10)	H (10.72)	N (4.11)

Preparation of Tris(tetraphenylphosphonium) Tris[(dithiooxalato-S,S') ferrate(III)].$4H_2O$ [83]

Metal tris dithiooxalato complexes were prepared by the method described by Coucouvanis in reference 83. Tetraphenyphosphonium salts were used in place of tetraphenylarsonium salts.

Yield = 3.11g (72%)

Elemental Analysis / %

Calc. for $C_{78}H_{68}O_{10}S_6P_3Fe$	C (62.19)	H (4.55)	N (0)
Found	C (61.81)	H (4.76)	N (0)

Preparation of Tris(tetraphenylphosphonium) Tris[dithiooxalato-S,S') chromate(III) monohydrate.[83]

Yield = 2.34g (53%).

Elemental Analysis / %

Calc. for $C_{78}H_{62}O_7S_6P_3Cr$	C (64.67)	H (4.31)	N (0)
Found	C (64.37)	H (4.76)	N (0)

2.2.3 Preparation of Squarates

Sodium and potassium salts of squarate complexes were prepared by a collection of methods described in the literature [85-89] and the thesis of K. P. Mann [84]. The tetrabutylammonium salts were prepared by the method described in section 2.2.2.

Preparation of 2,4- bis- (dimethylamino)-1-oxo-cyclobutenylium-3-olate (**6**) [84]

Dimethylamine solution (40%, 2.18g, 20mmol) was added to a suspension of 3,4-Dihydroxy-3-cyclobutene-1,2-dione (0.57 g, 5 mmol) in Dimethhylformamide (25 cm^3). The mixture was heated at 190 °C for 24 h in an autoclave, after which time it was allowed to cool. The solvent was then removed on a rotary evaporator to yield the crude product which was washed twice with diethylether (10 cm^3). The product was recrystallised by suspending in diethylether (20 cm^3) and adding hot ethanol dropwise until all the material had dissolved. Yield = 0.35 g (41%)

Elemental Analysis / %

Calc. for $C_8H_{12}N_2O_2$	C (57.13)	H (7.19)	N (16.66)
Found	C (57.20)	H (7.38)	N (16.66)

Preparation of disodium-cyan [3-(cyanimino)-2-oxido-4-oxo-1-cyclobutene-1-yl] amide tetrahydrate (**7**) [85]

Sodium metal was cleaned under hexane and added to absolute ethanol to prepare a 5% solution of sodium ethoxide. To this solution, **6** (840mg, 5 mmol) and cyanamide (420 mg, 10 mmol) were added. The mixture was stirrred at 50 °C for 3 hours and the precipitate was collected by filtration. The product was recrystallised from a 1:1 mixture of methanol and water.

Preparation of disodium-dicyan [3-(dicyanmethylene)-2-oxido-4-oxo-1-cyclobutene-1-yl] methanide trihydrate(**8**) [86]

Sodium metal was cleaned under hexane and added to absolute ethanol to prepare a 5% solution of sodium ethoxide. To this solution, **6** (840mg, 5 mmol) and malononitrile (660 mg, 10 mmol) were added. The mixture was heated under reflux for 2.5 hours and the orange/red crystals were collected and recrystallized from water.
Elemental Analysis / %

Calc. for $C_{10}H_6O_5N_4Na_2$	C (38.98)	H (1.96)	N (18.18)
Found	C (39.58)	H (1.95)	N (16.44)

Preparation of Dipotassium-1,3-dithio-cyclobutenylium monohydrate (**9**) [85]

Potssium metal, cleaned under hexane was added to absolute ethanol (30 cm^3) to form a 5% solution of potassium ethoxide. To this solution, **6** (340 mg, 2 mmol) was suspended and a stream of Hydrogen Sulfide was bubbled through to yield a yellow precipitate. This was collected by filtration and washed with ethanol (30 cm^3) followed by diethylether (15 cm^3). The product was recrystallised from water. The elemental analysis results indicate that some starting material is still present and therefore, the product was recrystallised again before use.

Elemental Analysis / %

Calc. for $C_4H_2O_2S_2K_2$	C (21.41)	H (0.90)	N (0.00)	S (28.57)
Found	C (21.74)	H (0.47)	N (0.94)	S (23.43)

Preparation of 3,4-dibutoxy-3-cyclobutene-1,2-dione (**10**) [87]

3,4-Dihydroxy-3-cyclobutene-1,2-dione (2.85 g, 25 mmol) was suspended in a mixture of toluene (37.5 cm^3) and butanol (37.5 cm^3). The mixture was heated to reflux using a Dean- Stark trap to remove the water from the reaction flask to prevent the reverse reaction. The reaction was stopped when two molar equivalents of water had been removed. The solution was then allowed to cool and the solvent removed on a rotary evaporator. The product was purified by vacuum distillation.

Yield = 5.20 g (92%)

Preparation of disodium-dicyan[2-(dicyanmethylene)-3-oxido-4-oxo-1-cyclobuten-1-yl] methanide trihydrate (**11**) [85]

A solution of 5% sodium butoxide was prepared by adding sodium metal (cleaned under hexane) to butanol. To this solution, **10** (1.13 g, 5 mmol) and cyanamide (420 mg, 10 mmol) were added. The mixture was heated under reflux for 1 hour and the precipitate was collected by filtration. The crude product was recrystallised from water and dried *in vacuo* .

Elemental Analysis / %

Calc. for $C_6H_6O_5N_4Na_2$	C (27.71)	H (2.33)	N (21.54)
Found	C (32.42)	H (2.05)	N (21.73)

Preparation of disodium-cyan [2-(cyanamino)-3-oxido-4-oxo-1-cyclobuten-1-yl] amide monohydrate (**12**) [85]

A solution of 5% sodium butoxide was prepared by adding sodium metal (cleaned under hexane) to butanol. To this solution, **10** (1.13 g, 5 mmol) and malononitrile (660 mg, 10 mmol) were added. The mixture was heated under reflux for 2 hours and the precipitate was collected by filtration. The crude product was recrystallised from water.

Elemental Analysis / %

Calc. for $C_{10}H_2O_3N_4Na_2$	C (44.14)	H (0.74)	N (20.59)
Found	C (44.65)	H (0.97)	N (20.31)

Preparation of 3,4-di-n-butoxy-3-cyclobutene-dithione (**14**) [88]

To a solution of **10** (3.4 g, 15 mmol) in diethylene glycol dimethyl ether (50 cm^3), phosphrous pentasulfide (14 g, 31.5 mmol) and sodium hydrogen carbonate (2.6 g, 31 mmol) were added. The mixture was left to stir at room temperature overnight. It was then poured onto water (50 cm^3) and the product was extracted with two portions of dichloromethane (50 cm^3). The organic phases were combined and dried over sodium sulfate, before being evaporated. The product is impure but is damaged by distillation and is of sufficient purity for the next steps.

Preparation of 2,4-bis (dimethylamino)-1-thioxo-cyclobutenylium-3-thiolate(**15**) [84]

Phosphrous pentasulfide (0.9g, 2mmol) was added to a suspension of **6** (0.85 g, 5 mmol) in diethylene glycol dimethyl ether (25 cm^3).To this, sodium hydrogen carbonate (1.25 g, 15 mmol) was added and the mixture was heated under reflux for one hour with stirring. The resulting solution was poured onto cold water (250 cm^3) to yield a yellow/orange precipitate. The product was collected by filtration and recrystallised from nitromethane.

Yield = 0.46 g (45%)

Preparation of dipotassium- tetrathiosquarate-monohydrate (**18**) [89]

Potassium metal, cleaned under hexane was slowly added to absolute ethanol to prepare a 5% solution of potassium ethoxide. To this, **15** (0.3g) was added to form a suspension and was left stirring for five minutes. Hydrogen sulfide was then bubbled through whilst the mixture was gently heated. The solution changed colour from orange to dark red to signify that the product had formed. The product was recrystallised by suspending it in hot ethanol and adding water dropwise until it had all dissolved.

Elemental Analysis / %

Calc. for $C_4H_2OS_4K_2$	C (17.65)	H (0.74)	S (47.06)
Found	C (17.94)	H (0.72)	S (45.49)

2.2.4 Preparation of Charge Transfer salts.

Charge transfer salts of BEDT-TTF X where X is an anion were prepared by electrocrystallisation techniques using Platinum electrodes. The electrodes are prepared for the synthesis by cleaning with aqua regia followed by immersing them in dilute sulfuric acid and applying a current across them for a few minutes. Gases are evolved at both electrode surfaces. The potential is then reversed. The electrodes are then washed with distilled water followed by methanol and thoroughly dried.

The electrochemical cell consists of three compartments, each separated by a glass frit. BEDT-TTF (~10mg) is placed in the anode compartment of the cell, to which an electrolyte which contains the desired anion (100mg) in an appropiate solvent (50cm^3) is added. The solvents are freshly distilled and degassed before use. A constant current (1μA) is then applied between the electrodes. The BEDT-TTF slowly dissolves into the solution resulting in a high concentration gradient at the anode, where it is oxidised. The oxidised material can then readily react with the anions in solution to form charge transfer salts, which grow from the anode.

The crystals are harvested by carefully removing them from the anode with a scapel blade and washing with acetone.

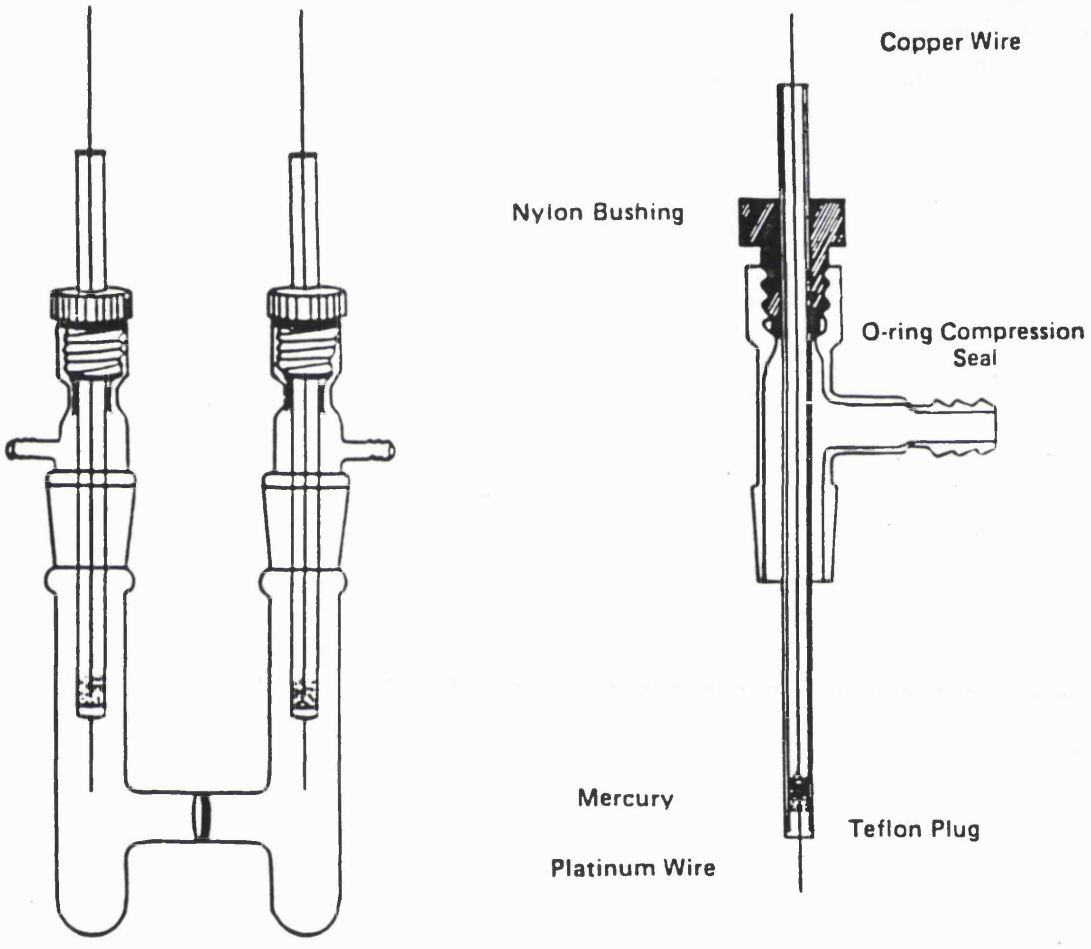

Figure 2.1 The electrochemical cell used by the Williams group.

Electrolyte	Solvent	Current	Product	Morphology
$K_2C_4O_4 + {}^{18}C_6$	C_6H_5CN	1.5μA	None	N/A
$K_2C_4O_4 + {}^{18}C_6$	CH_2Cl_2	1.5μA	Yes	Plate
$K_2C_4S_4.H_2O + {}^{18}C_6$	C_6H_5CN	1.5μA	Yes	Needle
$K_2C_4S_4.H_2O + {}^{18}C_6$	C_6H_5CN	0.2 - 2μA	None	N/A
$K_2C_4S_4.H_2O + {}^{18}C_6$	CH_2Cl_2	0.2 - 2μA	None	N/A
$K_2C_4S_4.H_2O + {}^{18}C_6$	TCE	0.6, 0.8, 1.0μA	None	N/A
$K_2C_4S_4.H_2O + {}^{18}C_6$	THF	1.0, 1.5μA	None	N/A
$[N(C_4H_9)_4]_2C_4S_4.H_2O$	C_6H_5CN	1.5μA	None	N/A
$[N(C_4H_9)_4]_2C_4S_4.H_2O$	CH_2Cl_2	1.0μA	None	N/A
$[N(C_4H_9)_4]_2C_4S_4.H_2O$	TCE	1.0μA	None	N/A
$[N(C_4H_9)_4]_2C_4S_4.H_2O$	THF	1.0μA	Yes	Needle
$[C_6H_5NH_2]_2C_4S_4.H_2O$	C_6H_5CN	1.5μA	None	N/A
$[C_6H_5NH_2]_2C_4S_4.H_2O$	CH_2Cl_2	1.0μA	None	N/A
1,2-$K_2C_4O_2S_2.H_2O + {}^{18}C_6$	C_6H_5CN	1.0μA	None	N/A
1,2-$K_2C_4O_2S_2.H_2O + {}^{18}C_6$	CH_2Cl_2	1.0μA	None	N/A
1,2-$K_2C_4O_2S_2.H_2O + {}^{18}C_6$	TCE	1.0μA	None	N/A
1,2-$[N(C_4H_9)_4]_2C_4O_2S_2.H_2O$	C_6H_5CN	1.5μA	None	N/A

Electrolyte	Solvent	Current	Product	Morphology
1,2-$[N(C_4H_9)_4]_2C_4O_2S_2.H_2O$	CH_2Cl_2	1.0μA	None	N/A
1,2-$[C_6H_5NH_2]_2C_4O_2S_2.H_2O$	C_6H_5CN	1.0μA	None	N/A
1,2-$[C_6H_5NH_2]_2C_4O_2S_2.H_2O$	TCE	1.0μA	None	N/A
1,3-$K_2C_4O_2S_2.H_2O$ + $^{18}C_6$	C_6H_5CN	1.0μA	None	N/A
1,3-$K_2C_4O_2S_2.H_2O$ + $^{18}C_6$	CH_2Cl_2	1.0μA	None	N/A
1,3-$K_2C_4O_2S_2.H_2O$ + $^{18}C_6$	TCE	1.0μA	None	N/A
1,2-$[N(C_4H_9)_4]_2C_4O_2(C(CN)_2)_2$	CH_2Cl_2	0.6, 1.0μA	None	N/A
1,2-$[N(C_4H_9)_4]_2C_4O_2(C(CN)_2)_2$	C_6H_5CN	1.0μA	None	N/A
1,2-$[N(C_4H_9)_4]_2C_4O_2(C(CN)_2)_2$	TCE	0.4, 0.6, 1.0μA	None	N/A
1,2-$[N(C_4H_9)_4]_2C_4O_2(C(CN)_2)_2$	THF	1.0μA	None	N/A
1,3-$[N(C_4H_9)_4]_2C_4O_2(C(CN)_2)_2$	THF	1.5μA	Yes	Plate/Needle
1,3-$Na_2C_4O_2(C(CN)_2)_2.H_2O$ +$^{18}C_6$	CH_2Cl_2	1.5μA	None	N/A
1,3-$Na_2C_4O_2(C(CN)_2)_2.H_2O$ +$^{18}C_6$	THF	1.5μA	Yes	Plate
1,2-$Na_2C_4O_2(NCN)_2.H_2O$	CH_2Cl_2	1.0μA	None	N/A
1,2-$Na_2C_4O_2(NCN)_2.H_2O$	C_6H_5CN	1.0μA	None	N/A
1,3-$Na_2C_4O_2(NCN)_2.H_2O$	CH_2Cl_2	1.0μA	None	N/A
1,3-$Na_2C_4O_2(NCN)_2.H_2O$	C_6H_5CN	1.0μA	None	N/A

Electrolyte	Solvent	Current	Product	Morphology
$KAu(SCN)_4 + {}^{18}C_6$	CH_2Cl_2	1.0μA	Yes	Microcrystalline
$K_2Pt(SCN)_4 + {}^{18}C_6$	CH_2Cl_2	1.0μA	Yes	Microcrystalline
$K_2Pd(SCN)_4 + {}^{18}C_6$	CH_2Cl_2	1.0μA	Yes	Microcrystalline
$K_3Fe(C_2O_4)_3.3H_2O + {}^{18}C_6$	C_6H_5CN	0.3, 1.0μA	Yes	Diamond
$K_3Fe(C_2O_4)_3.3H_2O + {}^{18}C_6$	$C_6H_5CN + H_2O$	1.0μA	Yes	Plate
$Na_3Fe(C_2O_4)_3.3H_2O + {}^{18}C_6$	C_6H_5CN	1.0μA	Yes	Hexagon
$Na_3Fe(C_2O_4)_3.3H_2O + {}^{18}C_6$	C_6H_5CN	1.0μA	Yes	Spear
$[NH_4]_3Fe(C_2O_4)_3.3H_2O + {}^{18}C_6$	C_6H_5CN	1.0μA	Yes	Diamond
$[NH_4]_3Fe(C_2O_4)_3.3H_2O + {}^{18}C_6$	$C_6H_5CN + H_2O$	1.0μA	Yes	Needle
$[NH_4]_3Fe(C_2O_4)_3.3H_2O + {}^{18}C_6$	$C_6H_5CN + H_2O$	1.0μA	Yes	Plate
$[NH_4]_3Fe(C_2O_4)_3 + {}^{18}C_6$	$C_6H_5CN + H_2O$	1.0μA	Yes	Plate
$[NH_4]_3Fe(C_2O_4)_3 + {}^{18}C_6$	$C_6H_5CN + H_2O$	1.0μA	Yes	Needle
$[NH_4]_3Fe(C_2O_4)_3 + {}^{18}C_6$	C_6H_5CN	1.0μA	Yes	Diamond
$[NH_4]_3Fe(C_2O_4)_3 + {}^{18}C_6$	$C_6H_5CN + CH_3OH$	1.0μA	Yes	Needle
$[NH_4]_3Fe(C_2O_4)_3 + {}^{18}C_6$	C_6H_5CN + DMSO	1.0μA	Yes	Needle
$[N(C_4H_9)_4]_3Fe(C_2O_4)_3$	C_6H_5CN	1.0μA	Yes	Fine needle
$[(C_6H_5)_4P]_3Fe(C_2O_2S_2)_3$	C_6H_5CN	1.0μA	None	N/A

Electrolyte	Solvent	Current	Product	Morphology
$[(C_6H_5)_4P]_3Fe(C_2O_2S_2)_3$	$C_6H_5CN + H_2O$	1.0μA	Yes	Plate
$[(C_6H_5)_4P]_3Fe(C_2O_2S_2)_3$	CH_2Cl_2	1.0μA	None	N/A
$[(C_6H_5)_4P]_3Fe(C_2O_2S_2)_3$	$CH_2Cl_2 + H_2O$	1.0μA	Yes	Plate
$K_3Cr(C_2O_4)_3.3H_2O+ {}^{18}C_6$	C_6H_5CN	1.0μA	Yes	Fine needle
$K_3Cr(C_2O_4)_3.3H_2O+ {}^{18}C_6$	$C_6H_5CN + H_2O$	1.0μA	Yes	Needle
$K_3Co(C_2O_4)_3.3H_2O+ {}^{18}C_6$	C_6H_5CN	1.0μA	Yes	Spear
$K_3Co(C_2O_4)_3.3H_2O+ {}^{18}C_6$	$C_6H_5CN + H_2O$	1.0μA	Yes	Microcrystalline
$[NH_4]_3Co(C_2O_4)_3.3H_2O+ {}^{18}C_6$	C_6H_5CN	1.0μA	Yes	Diamond

Table 2.1 A summarry of the electrochemical results obtained during this research project.

2.3 Physical Measurements.

2.3.1 Conductivity.

Electrical contacts to the crystal were made by attaching gold wire (25μm) to the sample with Platinum paint (Emerton). These wires were then connected to an eight pin plug (Figure 2.1) with silver paint (Du Pont) and placed into a copper block at the bottom of the sample rod. The temperature was lowered using an Oxford instruments CF 100 continuous flow cryostat and was monitored by a Rh/Fe thermocouple which was contained within the copper block.

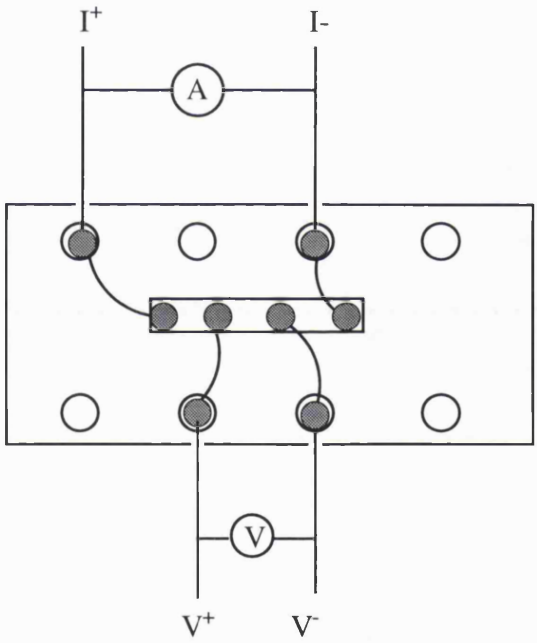

Figure 2.1. The four probe conductivity method.

The quality of the electrical contacts were checked by ensuring that:

$$R1\text{-}R4 \sim (R1\text{-}R2) + (R2\text{-}R3) + (R3\text{-}R4)$$

and that the ratio of the nested voltage (IVVI) to the unnested voltage (IIVV) was greater than 10:1.

Owing to the needle like morphology of the metallic samples prepared throughout this research project, four probes were attached to the crystal in a line, as shown in Figure 2.1. Current is passed between the outer two contacts and the potential difference is measured between the inner two probes. This set up is illustrated in Figure 2.1, where I represents the current and V the voltage.

For highly conducting samples, both A. C. and D. C. methods were employed. The A. C. measurement involved passing a constant current (10 μA) through the crystal via a home built current source and measuring the potential difference on a Brookdeal 9503-SC precision lock in amplifier. This was passed through a Hewlett- Packard 3478A digital multimeter to a Research Machines 380Z computer, where the data was collected on disk.

For semi conducting samples with a high ambient temperature resistance, two probe measurements were employed . A current is passed through the crystal using the Hewlett - Packard multimeter mentioned above and the drop in voltage is measured. This is proportional to the resistance, as described by Ohms Law (eq. 2.1). Owing to the high resistance of the sample, the contact resistance is assumed to be negligible.

$$R = V/I \qquad \textit{eq. 2.1}$$

The activation energies were calculated assuming that the electrons were thermally excited to a higher energy band according to the Boltzmann Distribution:

$$R = R_0 exp\,(E_a/kT) \qquad \textit{eq 2.2}$$

Therefore,

$$lnR / lnR_0 = E_a / kT \qquad \textit{eq 2.3}$$

Hence, a plot of lnR versus 1/T gives a straight line with a gradient equal to E_a/k. This value is divided by the elementary charge of an electron, to give the activation energy in electron volts.

2.3.2 Conductivity under pressure

Attempts to measure the pressure dependence on conductivity were performed in the Cavendish laboratory at the University of Cambridge in collaboration with Helmut Becker. The measurements were performed on single crystals of (BEDT-TTF)$_4$(H_2O)Fe(C_2O_4)$_3$.C_6H_5CN, using the four probe method described in the previous section. The electrical behaviour at ambient pressure was initially measured in order to elucidate the temperature dependent electrical properties of the particular crystal, before a hydrostatic pressure was applied. A summary of the experimental methods employed is given below.

The pressure head consists of ten pins, of which six are for the sample and four are for the manganin coil, employed to measure the pressure within the sample chamber. A teflon 'hat', filled with a 1:1 (by volume) mixture of n - pentane and i - pentane , was then placed over the pressure head. This mixture of solvents allows a glassy transition from the liquid to the solid state, thus minimising the stresses on the crystal and the contacts.

Electrical contacts to the crystal were made by evaporating gold pads onto the sample and attaching gold wire (10μm) with Dupont 4929 silver dag to the pads. The gold wires were then connected to pins on the pressure head, again by using silver dag. The pressure was obtained by compressing the teflon hat using a hydraulic press and was calculated by measuring the resistance of the calibrated manganin coil.

2.3.3 SQUID Magnetometery

Many methods have been developed to determine which type of magnetic behaviour is occurring within a given system. The most sensitve of these techniques is SQUID magnetometery and this technique has been used in order to elucidate the magnetic properties of the samples presented in this thesis.

Superconducting QUantum Interference Device (SQUID) experiments were performed on a Quantum Design MPSM7 SQUID magnetometer at The Royal Institution. Measurements were made on randomly oriented polycrystalline samples contained within a gelatine capsule. This capsule, along with several others, were placed into a non magnetic straw (see Figure 2.2). Several gelatine capsules are used so as to create an almost uniform environment over the scanning range and hence the only difference in enviromnment will be caused by the sample. The straw was then attached to a sample probe using diamagnetic tape (3M). The probe was inserted into the sample chamber, which was evacuated before the probe was lowered into the cryostat. The SQUID magnetometer is controlled by software and the experimental data was collected on a Hewlett - Packard 486/33N computer.

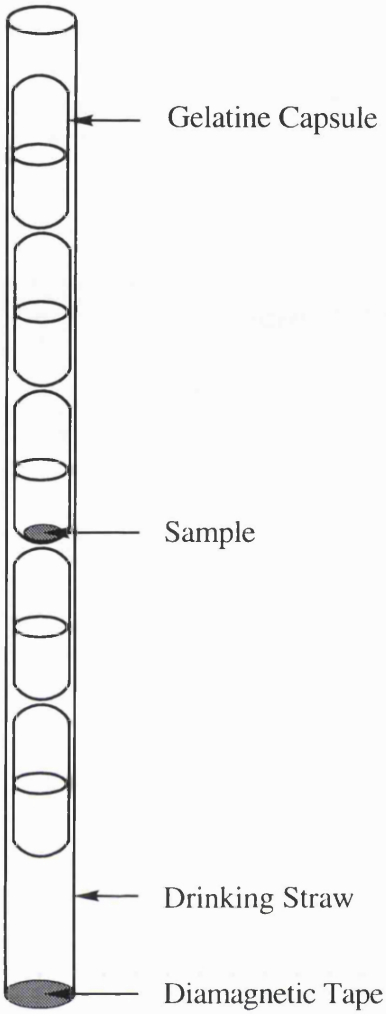

Figure 2.2 The mounting of a sample for a SQUID magnetometery experiment.

In order to accurately measure the sample, it must be centered with respect to the SQUID pick up coils. This is done by ensuring that the maximum signal (voltage) observed is at the midpoint of the scanning range. i.e. if the sample is being scanned over 4cm, the maximum voltage should be observed at 2cm. To achieve this, a small field is applied (~ 0.001T) and the SQUID response of the sample is measured. If the maximum voltage isn't observed at the midpoint of the scanning range, the sample position is adjusted (either manually or automatically) so that the maximum signal is at the centre. The sample is now in the correct position to be measured.

However, before the measurement can be performed, the field history of the magnet must be considered. As a SQUID involves the use of a superconducting magnet, flux is trapped inside, resulting in a remnant field. Most of the magnetic measurements performed in this thesis involve the sample being cooled in zero field, a field being applied and then data points being collected as the sample is warmed. The question of how zero field is achieved must therefore be addressed.

In order to obtain zero field, two methods have been employed. Firstly, before measuring the sample, the magnet is quenched in order to remove all of the trapped flux. This method is very effective, but results in the boiling off of large amounts of Helium and it is unadvisable to do very often. Hence, a second approach has been adopted which involves minimising the SQUID response from the sample. The response from the SQUID is proportional to the field applied and thus by minimsing this signal, the field will also be minimised. Therefore, after centering the sample, the magnet is set at a nominal zero field. The SQUID response is measured and depending upon its sign, a positive or negative field is applied. This procedure is repeated several times until a minimum is located. The value of the applied field at this point is taken as being zero field.

2.3.4 Fits to Magnetic Data

In this thesis, two types of fits to measured temperature dependance of the susceptibility have been used; a Curie Weiss fit for paramagnets and a Bleaney Bowers fit to a spin paired dimer. This section will describe the details of these fitting procedures.

In all cases the measured emu from the SQUID was converted to molar susceptibility via equation 2.4

$$\chi_{(molar)} = emu_{(SQUID)} * RMM / (mass\ (g) * Field\ (G) \qquad eq.\ 2.4$$

The molar susceptibility was then corrected for the core diamagnetism by subtracting the relevant Pascaal's constants from Table 1.6 for the respective materials. The data could then be fitted.

Paramagnets were fitted to the Curie Weiss law using equation 2.5

$$\chi_{(molar)} = C / (T - \theta) + \chi_{TIP} \qquad eq.\ 2.5$$

Both $\chi_{(molar)}$ and T are known from the experimental data and therefore, C, θ and χ_{TIP} are the only variables in the equation. χ_{TIP} is temperature independent and takes account of errors in the subtraction of Pascals constants, and contributions from the gelatine capsule and diamagnetic tape.

Mathematically, as C and θ are dependent upon each other, the Curie Weiss law cannot be considered to be a linear function. When an equation is dependent upon two non linear variables, the data can only be fitted accurately by solving the partial derivatives of the equation. The partial derivatives for C, θ and χ_{TIP} are given below:

$$\delta\chi_{(molar)} / \delta C = 1 / (T - \theta)$$
$$\delta\chi_{(molar)} / \delta\theta = C / (T - \theta)^2$$
$$\delta\chi_{(molar)} / \delta\chi_{TIP} = 1$$

The data is also weighted by using the errors in the meaasurement from the SQUID and converting this to a molar value as of equation 2.4

After calculating the fitted value for the paramagnetic terms in the samples, this value has been subtracted from the total susceptibility for the magnetisation of the organic layer to be analysed. As a large number is being subtracted from an even larger number to leave a small number, the errors in this will be quite significant. However, it is possible to observe the temperature dependence of any such magnetisation and see if the general form will fit any relevant equations.

For $(BEDT\text{-}TTF)_4KFe(C_2O_4)_3.C_6H_5CN$ (Chapter 3), it is appropiate to fit the magnetisation of the BEDT-TTF electrons to the Bleaney Bowers equation (section 1.3.1.6).

$$\chi_{(molar)} = ZT[3 + \exp(-J / kT) + \chi_{TIP} \qquad eq.\ 2.6$$

where Z is equal to $2Ng^2\mu_B{}^2/k$ and χ_{TIP} is again a temperature independent term employed for the same reasons given in the fitting of the Curie Weiss law.

The molar susceptibility and temperature are known from the experimental data and k is the Boltzmann constant. Therefore, the only variables in the equation are J (the energy gap) and χ_{TIP}. The data are again weighted in proportion to the molar equivalents of the measured errors from the SQUID.

2.3.5 Magnetoresistance

Magnetoresistance measurements were performed on a Quantum Design MPMS 7 SQUID magnetometer at The Royal Institution. The software for data collection was written by Dr. S. G. Carling. The experiment consisted of two single crystals of $(BEDT\text{-}TTF)_4Fe(C_2O_4)_3.C_6H_5CN$ oriented orthogonally with respect to each other. Both crystals had four gold wires (25μm) attached to them with platinum paint which were mounted as illustrated in Figure 2.3.

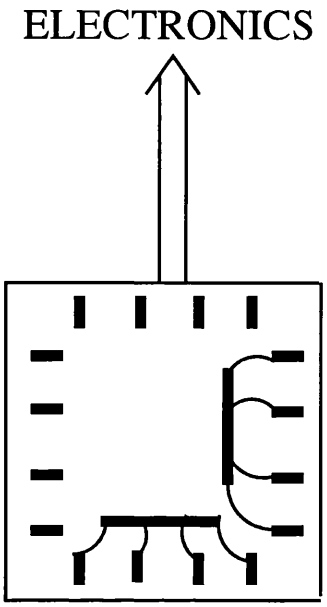

Figure 2.3 The mounting of $(BEDT\text{-}TTF)_4(H_2O)Fe(C_2O_4)_3.C_6H_5CN$ for magnetoresistance experiments.

Wires which were connected to a sample probe were then attached to the sample and the resistance could be measured via a Hewlett - Packard digital multimeter. The sample probe was then inserted into the cryostat and aligned with the magnet. Two types of measurements were performed. Firstly, the temperature was held constant and the field varied and secondly, the field was held constant and the temperature was varied. The second way proved to be the more successful.

2.3.5 Band Structure Calculations

Band structure calculations were performed at the University of Bordeaux with the expert guidance of Phillipe Guionneau and Laurent Ducasse. The tight banding method was employed, using the HOMOs of the BEDT-TTF molecules as the basis wavefunctions. The programme employed takes account of contributions from the Sulfur 3s, 3px, 3py, 3pz, the Carbon 2s, 2px, 2py, 2px and the Hydrogen 1s orbitals on the BEDT-TTF molecules, which were represented as Slater Type Orbitals (double ζ). The ionization potentials used for the Coulombic integrals are given in Table 2.2.

Orbital	Ionisation Potential (eV)
H (1s)	-13.060
C (2s)	-21.400
C (2p)	-11.400
S (3s)	-20.000
S (3p)	-13.300

Table 2.2 Ionisation potentials used for the Coulombic Integrals in Band Structure Calculations.

BEDT-TTF molecules within the plane were generated from the independant BEDT-TTF molecules within the asymmetric unit using the relevant symmetry operations. Transfer integrals for neighbouring molecules were calculated in all directions by using the dimer splitting method within the extended Huckel theory. In the case where there are two distinct types of BEDT-TTF molecules, monopositive and neutral, the energy levels of the respective HOMOs will be distinctly different. This energy difference (Δ) is accounted for in the code.

In order to account for different types of BEDT-TTF molecules the transfer integrals are averaged via the following equation:

$$t = t_1 t_2 / [(C_A/C_B) + (C_B/C_A)]$$

where t is the transfer integral and C_x are the atomic coefficients.

The Fermi level is placed at the value of the estimated band filling, which is calculated from the charge of the BEDT-TTF molecules. A full energy level will contain two electrons. By oxidising the BEDT-TTF molecule, electrons are taken out of this level (or more specifically from the energy band). In the case where the charge of BEDT-TTF is $1/2^{+}$, this means that 1/2 of an electron has been nominally removed. Therefore, this leaves 1.5 electrons in the energy level which is 3/4 the number of the original two electrons. Hence a charge of $1/2^{+}$ corresponds to a 3/4 filled electronic band.

2.3.6 X-ray Crystallography

Single crystal X-ray crystallography experiments were performed at the EPSRC service facility at the University of Wales, College of Cardiff by Simon Coles. The data were collected by attaching a single crystal to a glass capillary using araldite. This was then transferred onto a goniometer and aligned with graphite monochromated Mo $K\alpha$ (0.71069Å) radiation and cooled using an Oxford Instruments Cryostream. Data were collected on a Delft Instruments FAST TV area detector which was positioned at the window of a rotating anode FR591 generator (50kV, 40mA).

The structures were solved using the Patterson method to locate the heavy atoms, followed by successive Fourier syntheses to locate the other atoms (SHELX-S 86 software package) [90]. They were refined on a full-matrix least squares fit based

upon Fo^2. Hydrogen atoms were given idealised positions (C-H 0.97Å, HCH 109.5°) and refined with isotropic thermal parameters.

Visualisation of the structural data was performed at The Royal Institution using the Insight II package on a Silicon Graphics terminal. This enabled a detailed understanding of the crystal structures to be developed by viewing the structures in all possible orientations. Further to this specific parts of the molecules have been selected in order to determine the packing arrangements within respective layers of the materials and how these layers pack together. Finally, interaction distances have been measured, to elucidate the degree of Sulfur orbital overlap within the organic layer, the coordination present within the anionic layer and the Hydrogen bonding present within the whole molecule. These values have been confirmed by the BONDLA programme written by Jeremy Cockcroft.

Chapter 3

The Structure and Physical Properties of $(BEDT\text{-}TTF)_4AFe(C_2O_4)_3.C_6H_5CN$

A = K or NH_4

3.1 Introduction

The preparation of $(BEDT\text{-}TTF)_xM[(C_2O_4)_3]_y$ (M = Fe, Cr, Co) charge transfer salts has been described and summarised in section 2.2.4. This chapter will discuss the crystal structure, electrical properties and magnetism of two members of this family, $(BEDT\text{-}TTF)_4KFe(C_2O_4)_3.C_6H_5CN$ and $(BEDT\text{-}TTF)_4NH_4Fe(C_2O_4)_3.C_6H_5CN$. As will become evident from the forthcoming discussion, their structural and physical properties are very similar and a novel packing arrangement of the BEDT-TTF moieties is observed, which has some similarities to the high T_c κ - phase. This packing of the BEDT-TTF molecules accounts for both the electrical and magnetic properties associated with the respective compounds.

3.2 $(BEDT\text{-}TTF)_4KFe(C_2O_4)_3.C_6H_5CN$

3.2.1 The Crystal Structure of $(BEDT\text{-}TTF)_4KFe(C_2O_4)_3.C_6H_5CN$

The structural data of $(BEDT\text{-}TTF)_4KFe(C_2O_4)_3.C_6H_5CN$ are summarised in Table 3.1. The crystallographic data were collected on a single crystal with dimensions of 0.15 x 0.2 x 0.2mm and it has the empirical formula $C_{53}H_{36}O_{12}S_{32}FeK$. The unit cell was determined by at least 50 independent reflections which gives lattice parameters of a = 10.33(2)Å, b = 19.53(3)Å, c = 35.94(2)Å, $\alpha = 90°$, $\beta = 90°$, $\gamma = 90°$. The crystal has Pbcn symmetry. 4796 independent reflections were collected (16763 total) and the structure was refined on a Full matrix least squares fit on F^2 to give an R - factor of 0.0491 (wR2 = 0.1282). The atomic co-ordinates, bond lengths and bond angles are given in Appendix 1.

The asymmetric unit consists of two independent BEDT-TTF molecules, BEDT-TTF* and BEDT-TTF', and half of a $KFe(C_2O_4)_3.C_6H_5CN$ moiety. On application of the relevant symmetry operations, the full crystal structure is generated, which is

illustrated in Figure 3.1, viewed along the a axis. The diagram infers that the BEDT-TTF molecules have tetramerised in the stacking direction. The stack consists of two independent BEDT-TTF molecules which pack in a ..AABBAABB.. fashion. Between the BEDT-TTF stacks, there is an inorganic stack containing potassium iron tris oxalate and a benzonitrile molecule, as the solvent of crystallisation. This type of packing is customary within this family of molecular charge transfer salts, as was discussed in Section 1.2.3.2.

In order to elucidate the structural properties, it is necessary to examine the organic and inorganic layers separately. Upon removal of the BEDT-TTF molecules, a clearer perspective of the anion layer can be obtained. This is illustrated in Figure 3.2. It shows that the oxalate ions have formed a honeycomb structure, with the potassium cation co-ordinated to the outer oxygen atoms of the oxalate ligand. This type of hexagonal network has been previously reported in $A^{+}M^{3+}M^{2+}(C_2O_4)_3$ (M^{3+} = Fe, Cr; M^{2+} = Mn, Fe, Ni; A = NR_4^{+} or PR_4^{+}) [90] systems, in which there is a strong magnetic interaction between the metal centres. More recently, there have been reports on $A^{+}M^{3+}M^{1+}(C_2O_4)_3$ complexes [91], which do not possess such interesting magnetic properties, but still exhibit a honeycomb like structure. It is interesting to note that the structure of $(NH_4)_3Fe(C_2O_4)_3.3H_2O$ does not consist of a hexagonal array [92]. All of the $Fe(C_2O_4)_3$ moieties within the layer are of the same chirality. However, the chirality alternates from one inorganic layer to the next and therefore the molecule is not optically active.

The hexagon is comprised of three iron tris oxalate moities and three potassium ions. The solvent molecule resides in the cavity of this hexagon. The aromatic ring of the solvent molecule is in the same plane as the iron and potassium ions with a slight twist angle of 0.3°. However, the nitrile functional group is out of the plane by ~ 13°. The nitrogen atom on the benzonitrile molecule has two fold disorder and is also co-ordinated to the potassium ion. Therefore, the potassium has an overall co-ordination

number of seven (six oxygen atoms and one nitrogen). The bond distances associated with this co-ordination are given in Table 3.2.

K(1) - O(2) *2	2.861Å
K(1) - O(6) *2	2.879Å
K(1) - O(5) *2	2.826Å
K(1) - N(1) *2	2.952Å

Table 3.2. The coordination of the potassium cation in $(BEDT\text{-}TTF)_4KFe(C_2O_4)_3.C_6H_5CN$.

The co-ordination distances of the oxygen atoms to the potassium ion are all very similar and define a site symmetry of C_2. These distances indicate that there is only a minimal distortion of the octahedral array, which is a consequence of the disordered benzonitrile molecule.

A corresponding perspective of the BEDT-TTF layer can be obtained by removing the $KFe(C_2O_4)_3.C_6H_5CN$ moiety and viewing the structure along the long molecular axis. Figure 3.1 indicates that the BEDT-TTF molecules form tetramers. However, closer analysis of the BEDT-TTF layer reveals that the BEDT-TTF molecules have formed as orthogonal face to face dimers in one direction, as observed in the κ - phase materials (Section 1.2.3.2), but parallel face to face dimers perpendicular to this direction. This packing motif also differs from the κ - phase as the dimers are surrounded by six other undimerised BEDT-TTF molecules (Figure 3.3). This mode of packing has only been observed in the two structures reported in this chapter. A closer analysis of the organic layer reveals a difference in charge of the respective BEDT-TTF molecules. The face to face dimers both have a central C - C bond length of 1.381(7)Å, which from Table 3.3 is associated with $(BEDT\text{-}TTF)^+$ and the corresponding bond length in the surrounding BEDT-TTF moieties is 1.342(8)Å, indicating neutral BEDT-TTF. Therefore, the monopositive BEDT-TTF ions have

dimerised and are surrounded by six neutral BEDT-TTF molecules. The implications of this for the physical properties of the title compound will be discussed in Section 3.2.2.

Compound	Formal Charge	C=C distance (Å)
BEDT--TTF	0	1.32
β-$(BEDT\text{-}TTF)_2I_3$	+1/2	1.35
α-$(BEDT\text{-}TTF)_2IBr_2$	+1/2	1.35
$(BEDT\text{-}TTF)_2FeCl_4$	+1/2	1.36
γ-$(BEDT\text{-}TTF)_3(BrO_4)_2$	+2/3	1.37
γ-$(BEDT\text{-}TTF)_3(ClO_4)_2$	+2/3	1.37
$(BEDT\text{-}TTF)(ReO_4)(THF)_{0.5}$	+1	1.38

Table 3.3 The determination of charge on BEDT-TTF from the central C - C bond length. [102]

The packing in this layer affords considerable overlap of the Sulfur orbitals, both between the dimer pair and between the dimer and neutral BEDT-TTF molecules. These distances were calculated using the BONDLA programme written by Jeremy Cockcroft [93] and are summarised in Table 3.4.

S(1) - S(16)	3.391Å	S(6) - S(15)	3.425Å
S(2) - S(11)	3.475Å	S(7) - S(10)	3.431Å
S(2) - S(15)	3.510Å	S(8) - S(9)	3.501Å
S(3) - S(16)	3.192Å		

Table 3.4. Close Sulfur - Sulfur contact distances in $(BEDT\text{-}TTF)_4KFe(C_2O_4)_3.C_6H_5CN$.

The Van der Waals radii of two Sulfur atoms is 3.6Å and as can be seen from the table, there are many interactions within this distance. Of particular interest is the S(3) - S(16) interaction distance of 3.192Å, which is an extremely short contact distance in BEDT-TTF based materials. The other contact distances ranging between 3.4 - 3.5Å also result in considerable overlap of the Sulfur orbitals between the independent BEDT-TTF molecules.

The packing together of the two layers is depicted in Figure 3.4. For clarity only the potassium and iron ions of the oxalate layer are drawn and these are joined together by a line to form a hexagonal array. The organic layer is shown in full detail. This perspective clearly shows that the hexagons of the two layers are shifted with respect to each other. One of the BEDT-TTF molecules from the dimer pair resides above tris oxalato moeity and is parallel to the line of the hexagon. The neutral BEDT-TTF molecules reside above the cavity of the hexagon i.e. above the benzonitrile molecule.

Figure 3.5 shows the two independent BEDT-TTF molecules in greater detail. From this analysis it becomes apparent that the conformations of the terminal ethylene groups differ according to the BEDT-TTF molecule being considered. The charged species, $BEDT\text{-}TTF^{+}$ has ethylene groups eclipsed with respect to each other, whereas in the neutral BEDT-TTF molecules, these groups are staggered. Both ethylene groups are in the chair conformation. It is postulated that this arrangement is necessary in order to accomodate the packing pattern observed in the organic layer.
Hydrogen bonding interactions are assumed to be present when the distance between the two constituent atoms is less then the sum of the Van der Waals radii [94]. These distances are given in Table 3.5.

Interaction	Van der Waals Radii (Å)
O - H·····O	2.8
O - H·····N	2.9
N - H·····O	2.9
C - H·····O	3.0
N - H·····S	3.4

Table 3.5 The Van der Waals radii of Hydrogen bonded systems. From reference 94.

Table 3.6 collates the Hydrogen bonding distances observed within the lattice. There are interactions between the Hydrogen atoms on the BEDT-TTF molecules to the Oxygen atoms on the Oxalate ligand and also from the Hydrogen atoms from the solvent molecule to the same Oxygen atoms. H1 - H20 represent Hydrogen atoms from the BEDT-TTF molecules and H25 - H26 are from the Benzonitrile molecule.

H(2A) - O(5)	2.771Å	H(12B) - O(3)	2.634Å
H(2B) - O(5)	2.478Å	H(12B) - O(5)	2.729Å
H(9A) - O(3)	2.876Å	H(19B) - O(1)	2.732Å
H(9A) - O(4)	2.687Å	H(19B) - O(2)	2.460Å
H(10A) - O(6)	2.664Å	H(20B) - O(4)	2.641Å
H(11A) - O(6)	2.470Å	H(25) - O(6)	2.868Å
H(12A) - O(1)	2.664Å	H(26) - O(4)	2.750Å

Table 3.6 Hydrogen - Oxygen distances in $(BEDT\text{-}TTF)_4KFe(C_2O_4)_3.C_6H_5CN$.

The anion layer is stabilised by the formation of Hydrogen bonds between the benzonitrile molecule and the oxalate ligands, suggesting that the solvent is acting as a

template. The shortest Hydrogen bonding distances are observed between the donor and acceptor layers (e.g. H(2B) - O(5) 2.478Å). This offers evidence that the packing of the BEDT-TTF layer is controlled by the Hydrogen bonding between the two layers and hence the honeycomb packing of the anion layer is mirrorred in the BEDT-TTF layer. The docking of the Hydrogen atoms onto the oxalate ions shows how a pair of Hydrogen atoms reside above an oxygen atom of the oxalate ligand (Figure 3.6), in contrast to the κ - phase where the corresponding Hydrogen atoms sit in the holes of the anion layer [49]. As was discussed in section 1.2.3.2, the packing of the BEDT-TTF molecules in κ - phase materials is governed by the holes in the anion layer. The Hydrogen atoms on the terminal ethylene group of the organic molecule dock in the holes and this drives the phase of the BEDT-TTF layer. Figure 3.6 illustrates the docking of the Hydrogen atoms onto the oxalate layer in (BEDT-TTF)$_4$KFe(C_2O_4)$_3$.C_6H_5CN. The large circles represent the Oxygen atoms of the oxalate ligand and the smaller circles represent the Hydrogen atoms from BEDT-TTF. Rather than sitting in the holes of the anion layer, the Hydrogen atoms are positioned above the Oxygen atoms. The Hydrogen bonding interactions present in this material have already been discussed and it is proposed that it is this interaction which is driving the packing of the organic layer.

Empirical Formula	$C_{53}H_{36}O_{12}S_{32}FeKN$
Formula Weight	1999.70
Temperature (K)	120(2)
Wavelength (Å)	0.71069
Crystal System	Orthorhombic
Space Group	Pbcn
Unit Cell dimensions	a = 10.33(2) Å
	b = 19.53(3) Å
	c = 35.94(2) Å
Volume	7252(15) $Å^3$
Z	4
Density (calculated)	1.832Mg/m^3
Absorption coefficient	1.247 mm^{-1}
F(000)	4056
Crystal size	0.15 x 0.2 x 0.2 mm
θ range for data collection	2.09 to 25.07°
Index ranges	$-10 \leq h \leq 11$ $-15 \leq k \leq 15$ $-39 \leq l \leq 23$
Reflections collected	16763
Independent reflections	4796 [R(int) = 0.0564]
Refinement method	Full-matrix least-squares on F^2
Data / Restraints / Parameters	4786 / 0 / 462
Goodness of fit on F^2	1.059
Final R indices [$I > 2\sigma(I)$]	R1 = 0.0491, wR2 = 0.1282
R indices (all data)	R1 = 0.0596, wR2 = 0.1418
Largest diff. peak and hole	0.700 and -1.180 $e.A^{-3}$

Table 3.1 Crystal data for $(BEDT\text{-}TTF)_4KFe(C_2O_4)_3.C_6H_5CN$.

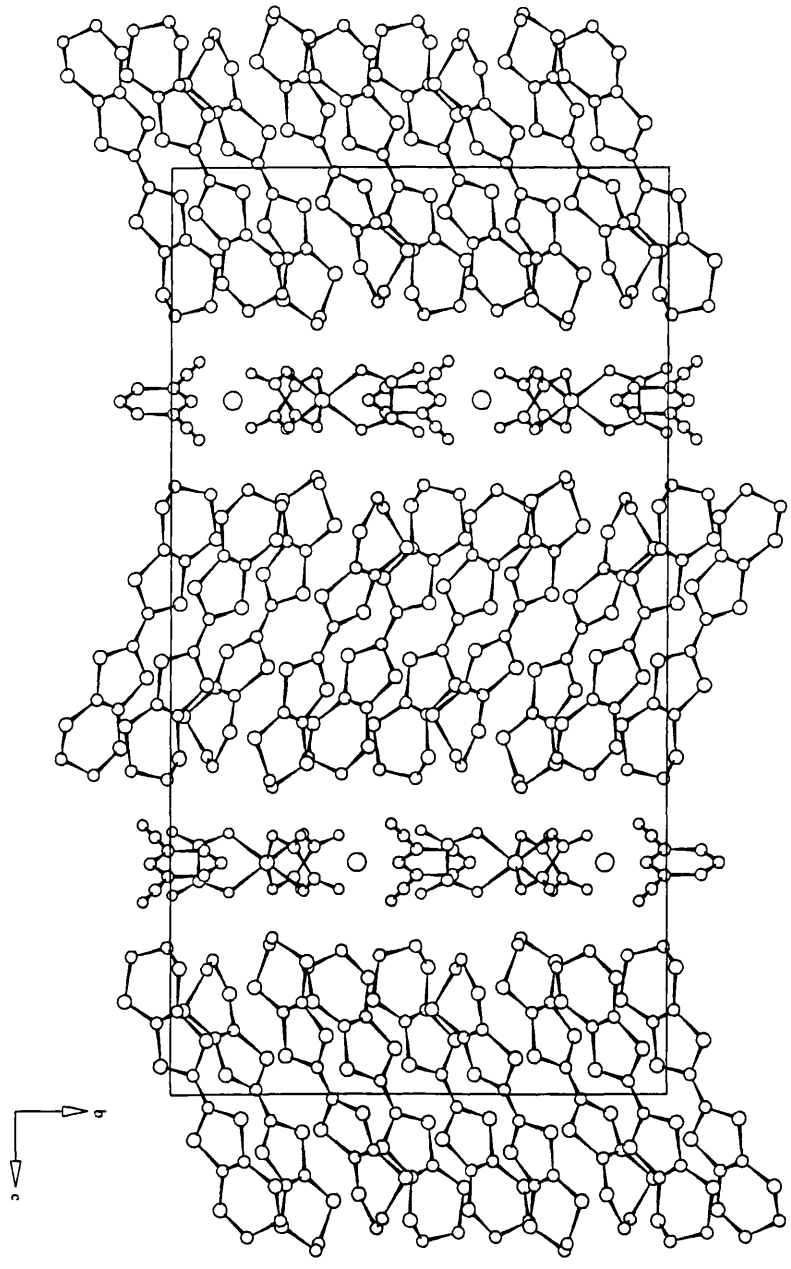

Figure 3.1 The crystal structure of (BEDT-TTF)$_4$KFe(C_2O_4)$_3$.C_6H_5CN viewed along the a axis.

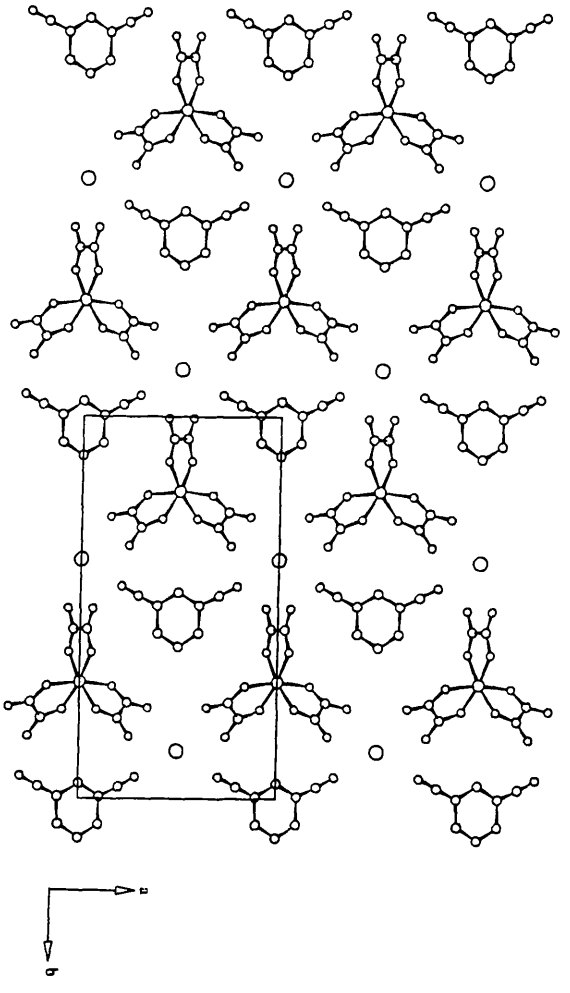

Figure 3.2 The anion layer of $(BEDT\text{-}TTF)_4KFe(C_2O_4)_3.C_6H_5CN$.

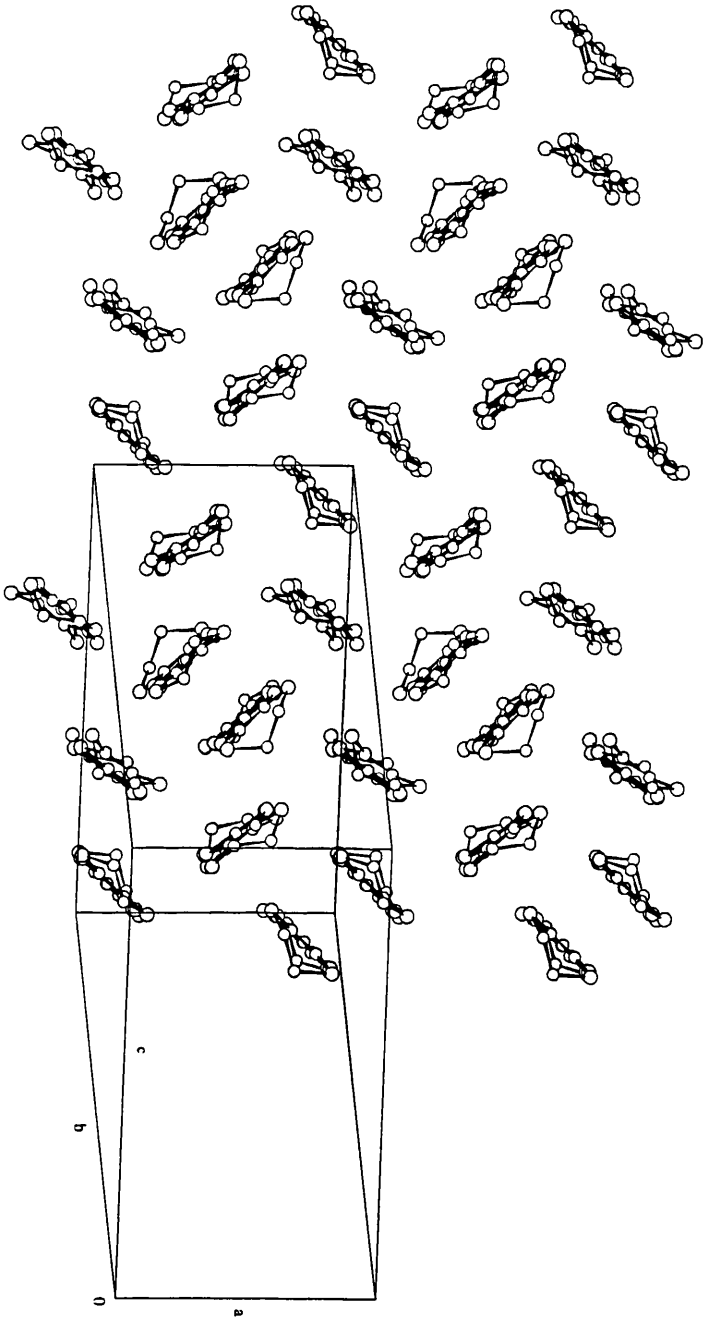

Figure 3.3 The cation layer of (BEDT-TTF)$_4$KFe(C_2O_4)$_3$.C_6H_5CN viewed along the long molecular axis.

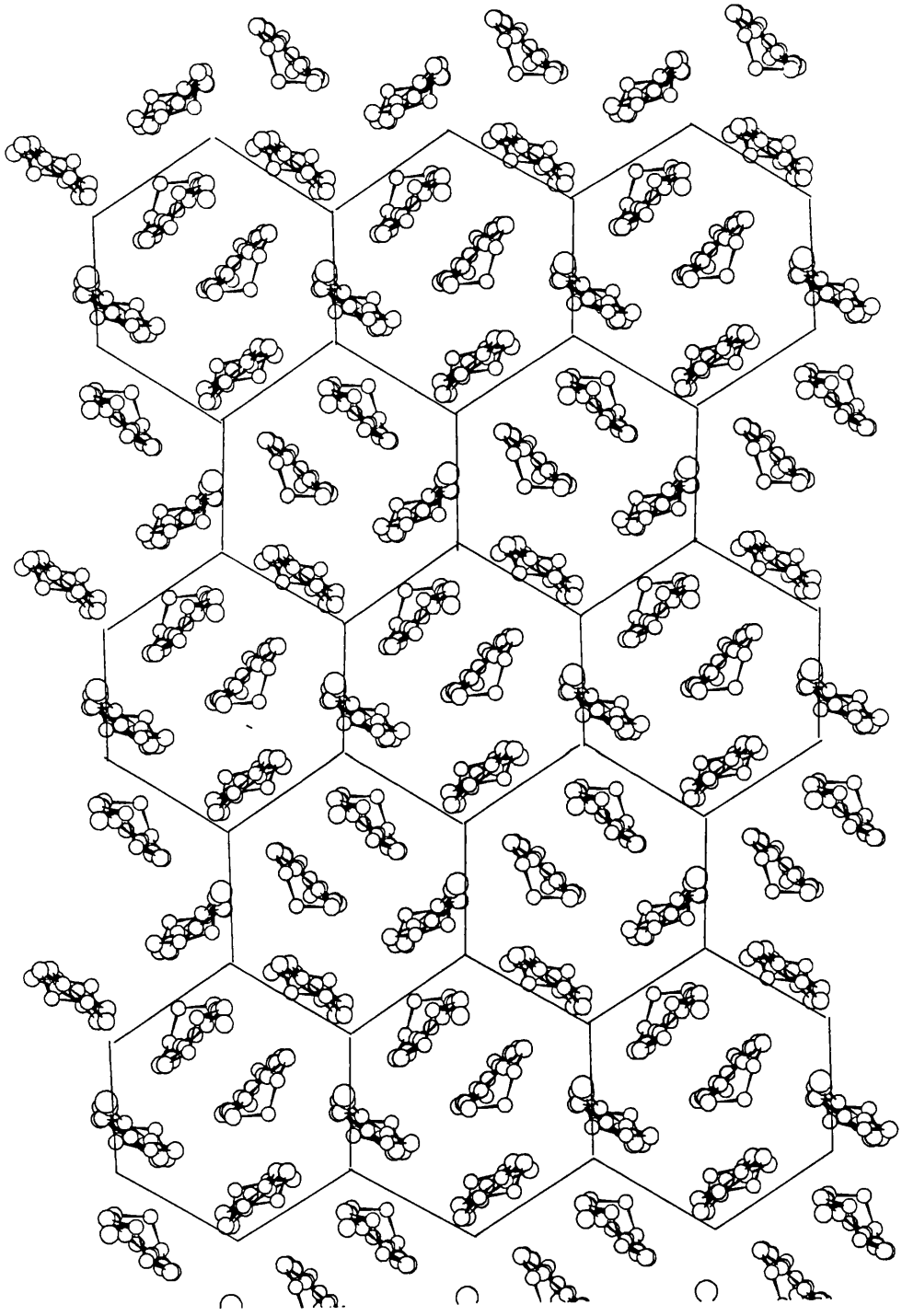

Figure 3.4 The packing together of the organic and inorganic layers in

(BEDT- TTF)$_4$KFe(C_2O_4)$_3$.C_6H_5CN.

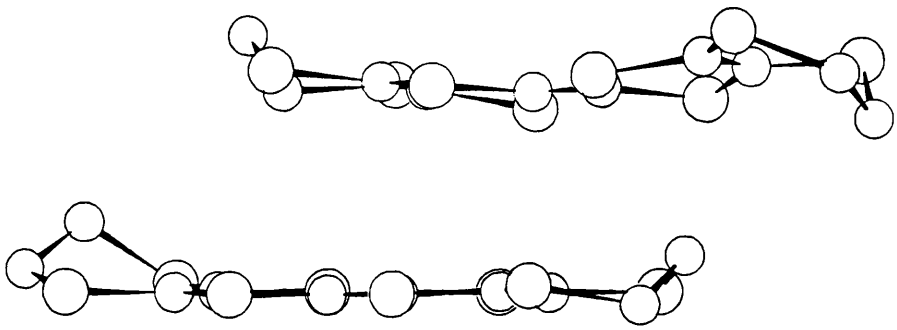

Figure 3.5 The conformations of the ethylene groups in $(BEDT\text{-}TTF)_4KFe(C_2O_4)_3.C_6H_5CN$.

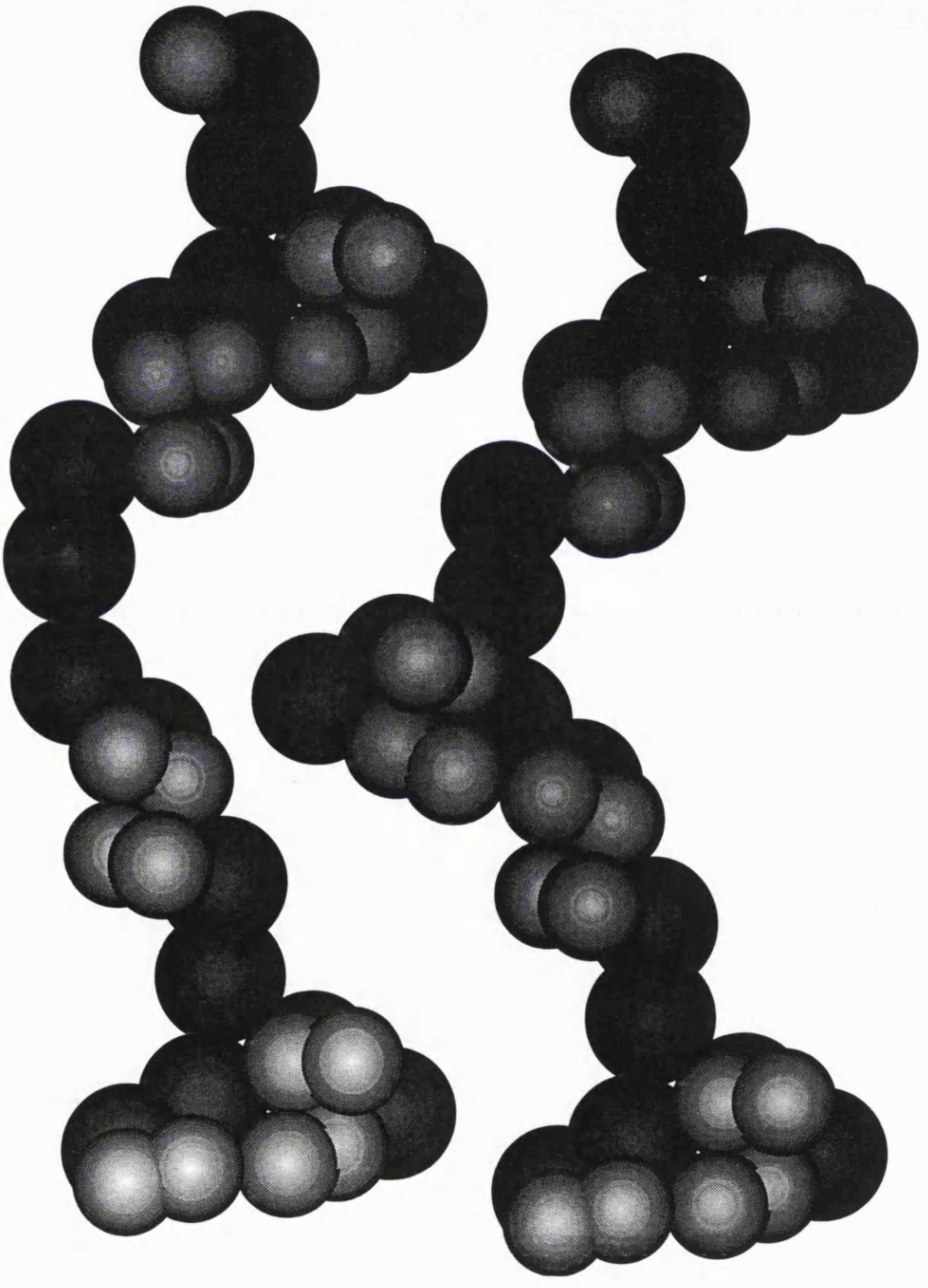

Figure 3.6 The docking of hydrogen atoms (small circles) from BEDT-TTF onto oxygen atoms (large circles) of the oxalate ligand in $(BEDT\text{-}TTF)_4KFe(C_2O_4)_3.C_6H_5CN$.

3.2.2 Electrical Transport

Electrical transport measurements were performed along the three crystal axes by attaching six gold wire (25μm) probes to a single crystal with Platinum paint, as depicted in Figure 3.7. The crystal was cooled from room temperature to 140K, recording the resistance every 1K.

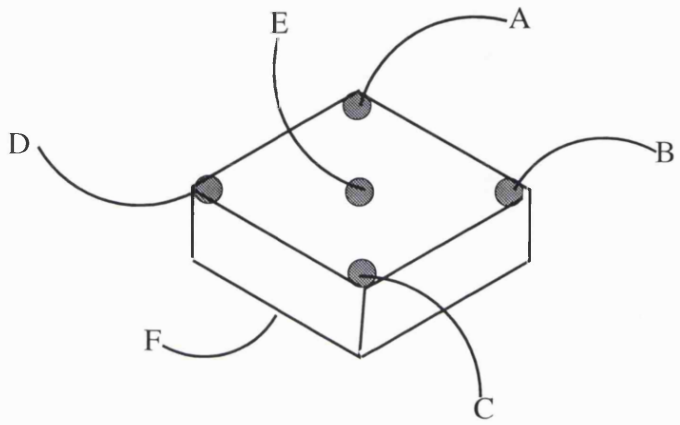

Figure 3.7 The crystal mounting in three dimensions for (BEDT-TTF)$_4$KFe(C_2O_4)$_3$.C_6H_5CN for conductivity experiments.

The resistance was calculated via Ohms Law. The measurements were performed along the three crystal axes, between A to B; B to C and E to F and the results are depicted in Figure 3.8. The room temperature conductivity is ~10^{-4}Scm^{-1}, and this value decreases with temperature, indicating semi conducting behaviour. The plots of ln resistivity vs 1000/T give three straight lines which are parallel to each other, signifying that the activation energy is equal in all three directions. Least squares fits to the slope of these lines gives an activation energy of 0.14eV.

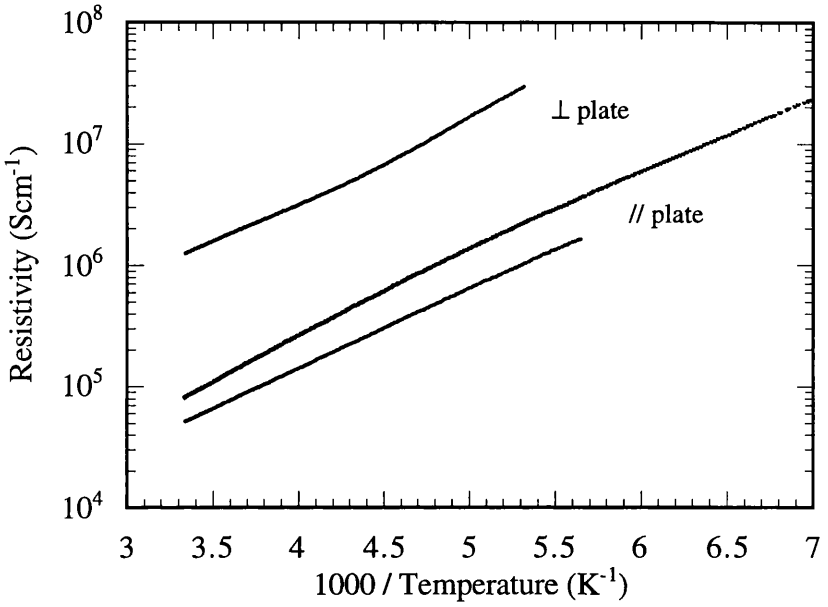

Figure 3.8 The ln resistivity versus inverse temperature for (BEDT-TTF)$_4$KFe(C_2O_4).C_6H_5CN along the three crystal axes.

A description why semi conducting behaviour is observed is given below.

There are two types of BEDT-TTF moieties in the crystal structure, (BEDT-TTF)$^+$ and (BEDT-TTF)^0. The neutral species will have a filled electronic shell (HOMO), the monopositive species will have a half filled HOMO which could result in metallic properties, but as can be observed from the crystal structure, the monopositive BEDT-TTF ions have dimerised.

This dimerisation results in the formation of a full and empty electronic band separated by an energy gap. Therefore, the conductivity will be thermally activated and semiconducting behaviour will prevail.

3.2.3 Band Structure

Band structure calculations were performed assuming that the only significant contribution to the electronic conduction was from the BEDT-TTF layer. In order to calculate the transfer integrals, it was necessary to generate all the BEDT-TTF molecules within the unit cell via the two independent BEDT-TTF molecules (A and B) in the asymmetric unit using the relevant symmetry operations. The operations which correspond to BEDT-TTF molecules in the same layer are the identity, I (x, y, z) and (1/2+x, 1/2-y, -z) which is denoted by the label II in Table 3.7 and Figure 3.9. Application of these operations yielded all of the BEDT-TTF molecules within the unit cell and these are labelled and depicted in Figure 3.9. This labelling scheme is maintained in Table 3.7.

Table 3.7 gives the transfer integrals for the organic semi conductor (BEDT-TTF)$_4$KFe(C_2O_4)$_3$.C_6H_5CN. These results would be intuitively expected from both the conductivity and susceptibility data. They indicate very strong dimerisation of the BEDT-TTF ions with little interaction between them and the neutral BEDT-TTF molecules.

A	-I (A) + c	+563	B	-I (B) + c + b	+45
A	-II (B) - b	-110	B	II (A) +c -a	0
A	-II (B) + c	0	B	II (A) + c	0
A	B - b	0	B	-II(A)	-106
A	II (B) +c -a	0	B	II(B) +c+b	+58
A	I + a +c	+11	B	II(B) + c-a+b	+58
-I (A)	II(B) + c - a	0	-II(B)	II(B) +c + b	+45

Table 3.7 Calculated transfer integrals (meV) for (BEDT-TTF)$_4$KFe(C_2O_4)$_3$.C_6H_5CN.

The only type of the latter interaction is between the moieties at A and $\Pi^{(B)}$-b, which despite a value of 110meV is still only 1/5 of the interaction between the molecules in the dimer. However, it is probably this interaction which affords semi conducting rather than insulating behaviour. The values of these transfer integrals offer further evidence of the importance in the way in which the participating orbitals overlap and the energy match between them in determining the transfer integrals. Crystal structure data show that both types of BEDT-TTF moieties are in close proximity to each other, and indeed the closest S - S contact distance is between independent BEDT-TTF molecules (S(3) - S(16) (3.192Å)). However, the transfer integrals give us more of an indication of the overlap of the Sulfur orbitals. A comparison can be drawn with the κ-phase materials whose structures contain orthogonal face to face dimers. These salts exhibit large (200-300meV) intra dimer transfer integrals but small inter dimer transfer integrals [95]. This offers further evidence of the similarity between these two phases. The band structure is illustrated in Figure 3.10 and clearly indicates an energy gap between the HOMO band and the LUMO band, which is consistent with the experimental data of the electronic properties.

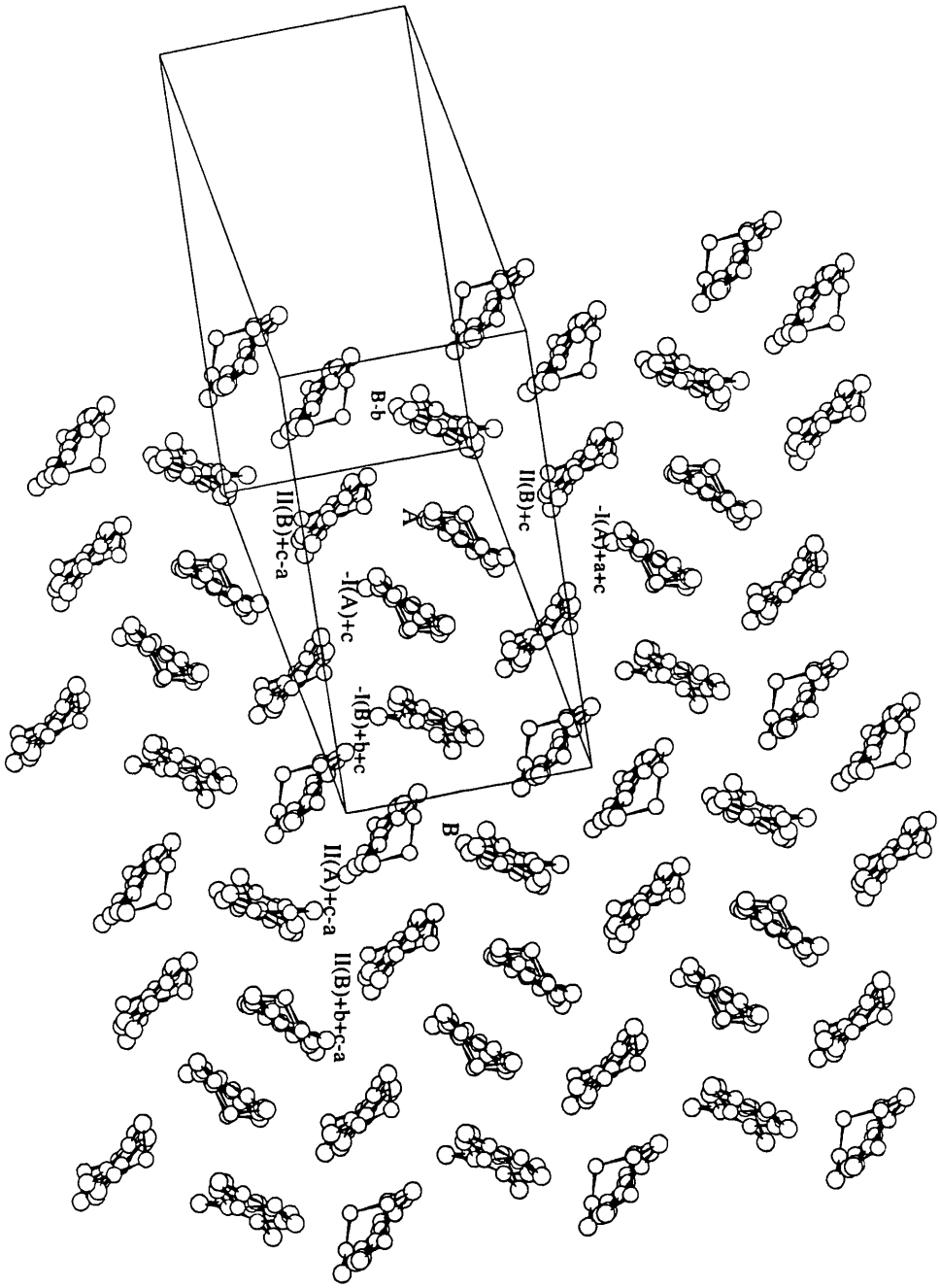

Figure 3.9 Symmetry related BEDT-TTF molecules in $(BEDT\text{-}TTF)_4KFe(C_2O_4)_3.C_6H_5CN$.

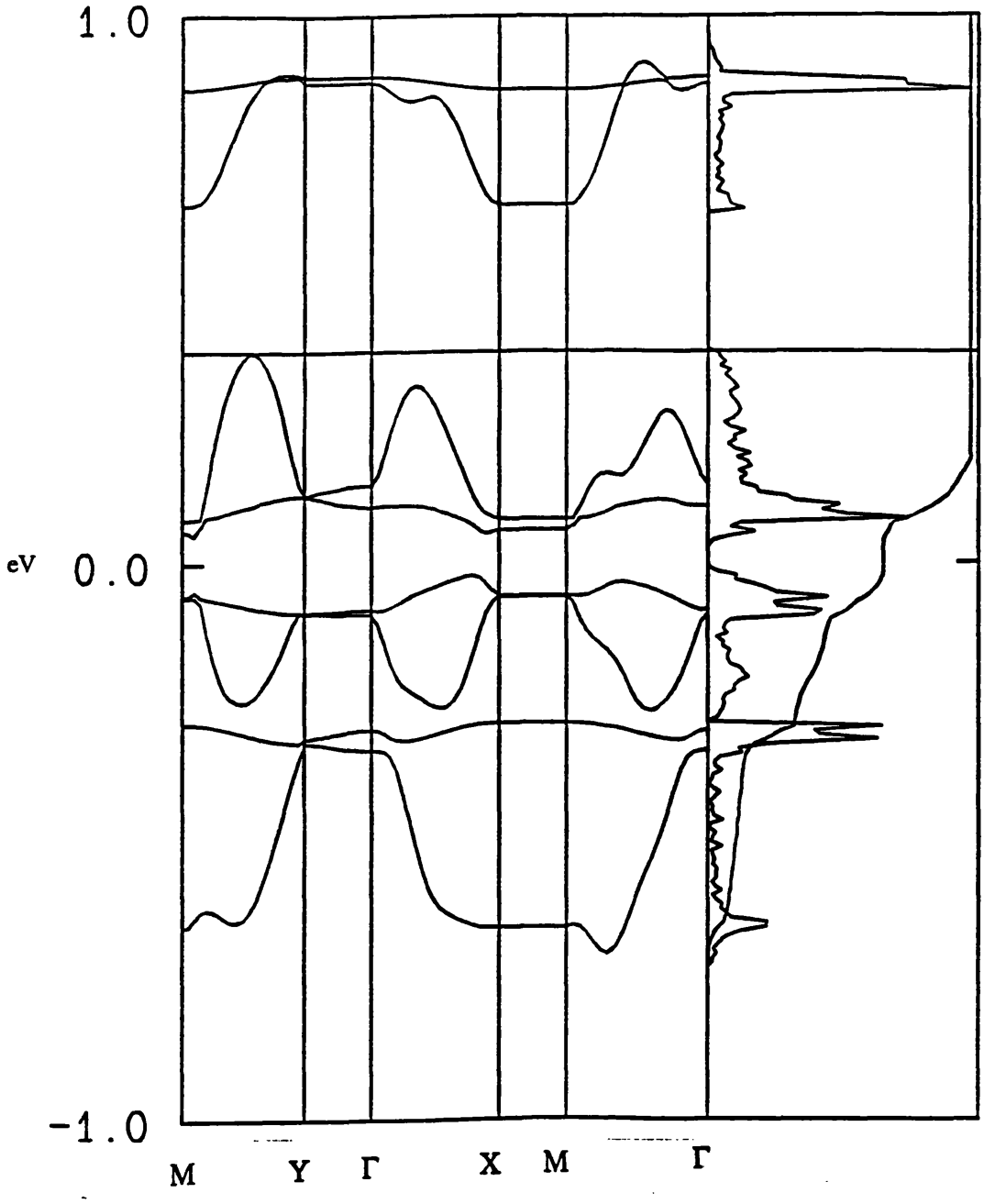

Figure 3.10 The Band Structure of $(BEDT\text{-}TTF)_4KFe(C_2O_4)_3.C_6H_5CN$.

3.2.4 SQUID magnetometery

3.2.4.1 Susceptibility.

The temperature dependent magnetic susceptibility of a polycrystalline sample is shown in Figure 3.11. The data were collected by cooling the sample in zero field to 2K and then applying a field of 1T. The sample was then warmed and the data were collected every 0.5K between 2 to 25K, every 1K between 25 to 50K and at 5K intervals between 50 to 300K. A plot of $1/\chi$ versus temperature (Figure 3.11) clearly indicates that the material is a paramagnet and fits to the Curie Weiss law give C = 4.44 emuKmol^{-1} and θ = -0.26K. The theoretical value of C for a S=5/2 system is 4.375, indicating a very good agreement with the experimental data which suggests that the susceptibility is dominated by the high spin Fe^{3+} ion in the anion layer.

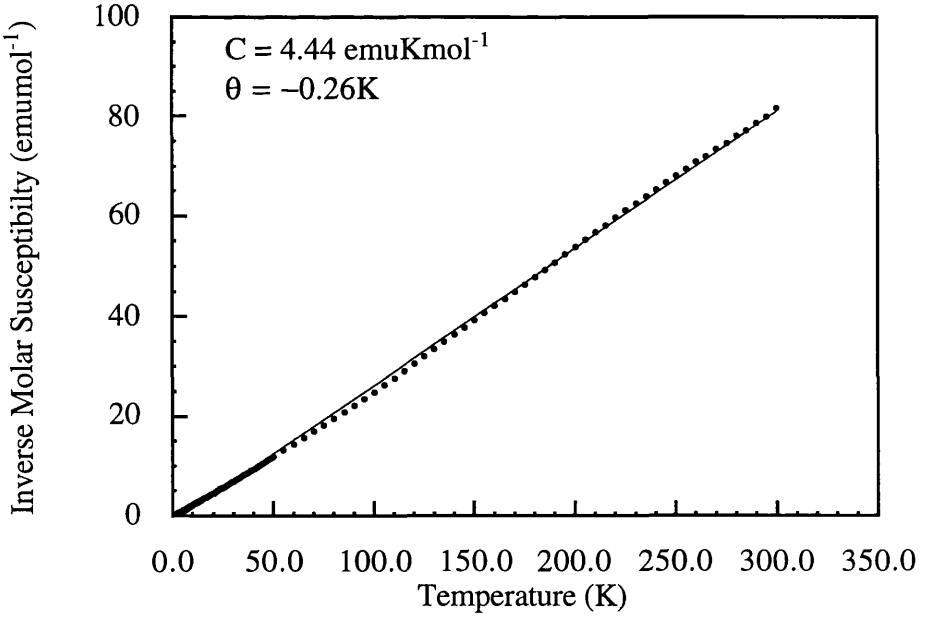

Figure 3.11 Curie Weiss fit to the molar susceptibility of (BEDT-TTF)$_4$KFe(C_2O_4)$_3$.C_6H_5CN. Data recorded at 1T.

The susceptibility of the BEDT-TTF can be calculated by subtracting the calculated value for the contribution of Fe^{3+} from the total susceptibility as in equation 3.1:

$$\chi_{(BEDT\text{-}TTF)} = \chi_{(TOTAL)} - \chi_{(Fe^{3+})} \qquad eq.\ 3.1$$

The $\chi_{BEDT\text{-}TTF}$ is the susceptibility associated with the electrons of the organic layer. This is illustrated in Figure 3.12. The diagram shows a small temperature dependent susceptibility which could be accounted for by the electrons of BEDT-TTF.

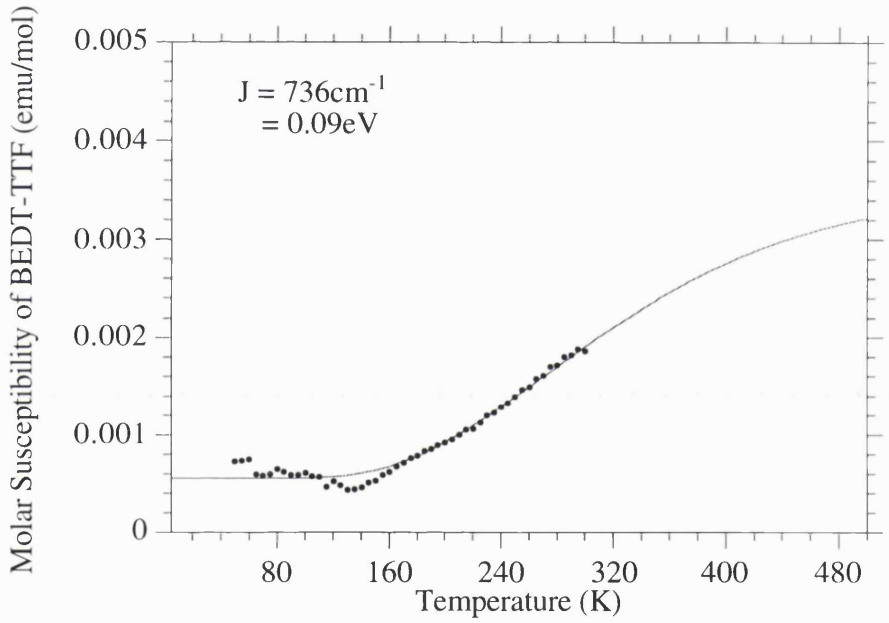

Figure 3.12 Bleaney Bowers fit to the susceptibility of BEDT-TTF in (BEDT-TTF)$_4$KFe(C$_2$O$_4$)$_3$.C$_6$H$_5$CN.

This can be explained by considering the electrical and crystallographic properties of the compound. Each $(BEDT\text{-}TTF)^+$ ion will donate one electron to the electronic band. If one of the dimer molecules donates an electron with a spin up and the other donates an electron with spin down, a singlet is formed and the net susceptibility from the dimer pair will be zero. Therefore, at 0K there will be no contribution to the susceptibility from the organic layer. However, when the system is warmed, electrons

will be excited to a higher energy level, resulting in the formation of a triplet state. This state will contribute to the susceptibility and the activation energy between the two states (J) can be calculated via the Bleaney Bowers equation (equation 1.23). Application of this equation gives an energy difference of 736cm^{-1} (0.09ev). This corresponds to a value of ~2000K, and therefore it must be noted that this data is fitted over a very small temperature range with respect to the energy gap.

3.2.4.2 Magnetisation

The magnetisation was measured at 2K up to a field of 7T. Data were collected every 0.25T and the results are illustrated in Figure 3.13. The theoretical values for a S = 5/2 (g = 2) system at 2K are represented by empty circles and the experimental data points collected for (BEDT-TTF)$_4$KFe(C_2O_4)$_3$.C_6H_5CN are depicted by filled circles.

The experimental data points are almost superimposable upon the calculated values, justifying the assumption that S = 5/2 and g = 2. This data indicates that the paramagnetic contribution to the susceptibility comes solely from the high spin Fe^{3+} system.

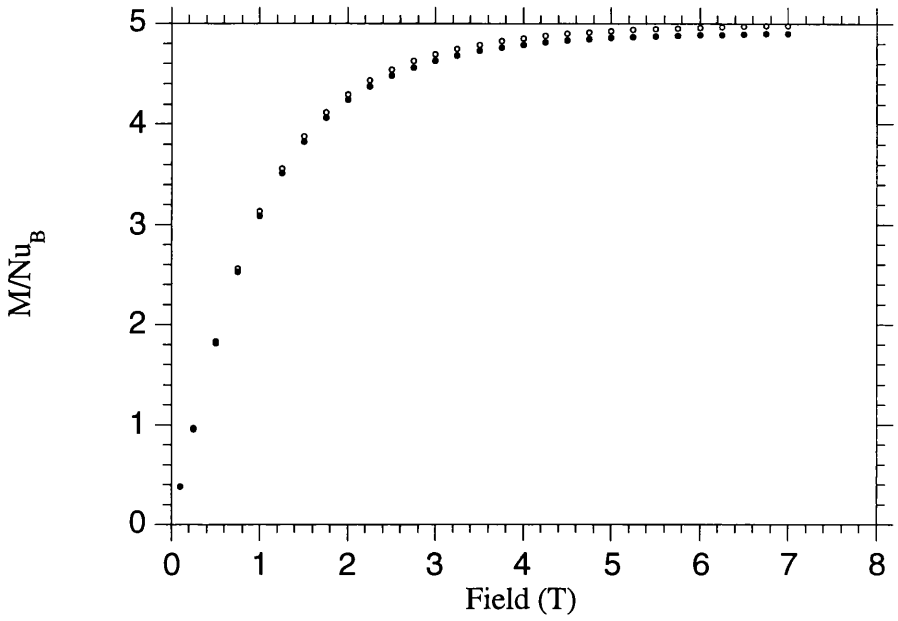

Figure 3.13 The magnetisation of (BEDT-TTF)$_4$KFe(C_2O_4)$_3$.C_6H_5CN (filled circles) and the theoretical (empty circles) Brillouin function for S = 5/2 and g = 2.

3.3 (BEDT-TTF)$_4$NH$_4$Fe(C_2O_4)$_3$.C_6H_5CN.

3.3.1 Crystal Structure

The structural details of (BEDT-TTF)$_4$NH$_4$Fe(C_2O_4)$_3$.C_6H_5CN are summarised in Table 3.8. The crystallographic data were collected on a twinned crystal with dimensions of 0.15 x 0.2 x 0.2mm and it has the empirical formula $C_{53}H_{40}O_{12}S_{32}FeN_2$. The unit cell was determined from at least 50 independent reflections which indicates lattice parameters of a = 10.370(5)Å, b = 19.588(12)Å, c = 35.790(8)Å, α = 90°, β = 90°, γ = 90°. Twinning of the crystals caused great difficulty in identifying the space group. It was assumed that the material would be isostructural to the corresponding potassium salt and thus the structure was solved assuming Pbcn symmetry. 5561 independent reflections were collected (14915 total) and the structure was refined on a Full matrix least squares fit on F^2 to give an R -

factor of 0.1557 (wR2 = 0.3831). The atomic co-ordinates, bond lengths and bond angles are given in Appendix 1.

The R - factor is high due to the twinning of the crystals, resulting in poor quality data. The structure could only be solved by using the atomic co-ordinates of (BEDT-TTF)$_4$KFe(C_2O_4)$_3$.C_6H_5CN as a basis for the refinement. The atoms were held within an isotropic sphere whilst being refined. Allowing the atoms to find their locations within an anisotropic sphere resulted in a massive increase of the R - factor, and thus the reported data is for the atoms being held within an isotropic sphere. Therefore, the bond angles and lengths cannot be considered to be of a high degree of accuracy and neither can the lattice co-ordinates. However, it can be concluded from the data that this compound is isostructural to the potassium analogue.

Consequently, the reader is referred to the discussion of the crystal structure of (BEDT-TTF)$_4$KFe(C_2O_4)$_3$.C_6H_5CN in order to understand the structure of the NH_4 compound and apart from the empirical observation that the two materials are isostructural , no detailed comparisons will be made.

Figures 3.14 - 3.16 illustrate the structure viewed along the a axis, the anion layer and the BEDT-TTF layer respectively. These diagrams confirm that the two materials are isostructural, the only difference being the replacement of a potassium ion for an ammonium ion. The ammonium cation is slightly larger than the potassium cation (1.43Å opposed to 1.33Å) [96] and hence there is the possibility of observing Hydrogen bonding within the anionic layer. As a consequence of the poor quality data though the Hydrogen atoms have not been fixed for the final refinement.

The anion layer again depicts a hexagonal array of the metal tris oxalate complexes, with the outer oxygens of the oxalate ligand being co-ordinated to the ammonium

cation and benzonitrile residing in the cavity of the honeycomb. The solvent molecule is again disordered.

The packing of the organic layer mirrors the packing of the anion layer, as was observed in the potassium compound. The BEDT-TTF molecules have formed orthogonally oriented face to face dimers, with each dimer being surrounded by six other BEDT-TTF molecules. The charges of the respective BEDT-TTF molecules cannot be accurately deduced from the bond lengths, but as will become clear from the following sections, it is postulated that the dimers are monopositive and that the surrounding BEDT-TTF molecules are neutral.

Empirical Formula	$C_{53}H_{36}O_{12}S_{32}FeN_2$
Formula Weight	1974.61
Temperature (K)	120(2)
Wavelength (Å)	0.71069
Crystal System	Orthorhombic
Space Group	Pbcn
Unit Cell dimensions	a = 10.370(5) Å
	b = 19.588(12) Å
	c = 35.790(8) Å
Volume	7270(6) $Å^3$
Z	4
Density (calculated)	1.804Mg/m^3
Absorption coefficient	1.187 mm^{-1}
F(000)	4008
Crystal size	0.15 x 0.2 x 0.2 mm
θ range for data collection	2.08 to 25.07°
Index ranges	$-11 \leq h \leq 11$ $-22 \leq k \leq 22$ $-39 \leq l \leq 8$
Reflections collected	14915
Independent reflections	5561 [R(int) = 0.0987]
Refinement method	Full-matrix least-squares on F^2
Data / Restraints / Parameters	5561 / 0 / 205
Goodness of fit on F^2	2.178
Final R indices [$I > 2\sigma(I)$]	R1 = 0.1557, wR2 = 0.3831
R indices (all data)	R1 = 0.1902, wR2 = 0.3935
Largest diff. peak and hole	2.317 and -1.516 $e.A^{-3}$

Table 3.8 The crystal data for $(BEDT\text{-}TTF)_4NH_4Fe(C_2O_4)_3.C_6H_5CN$.

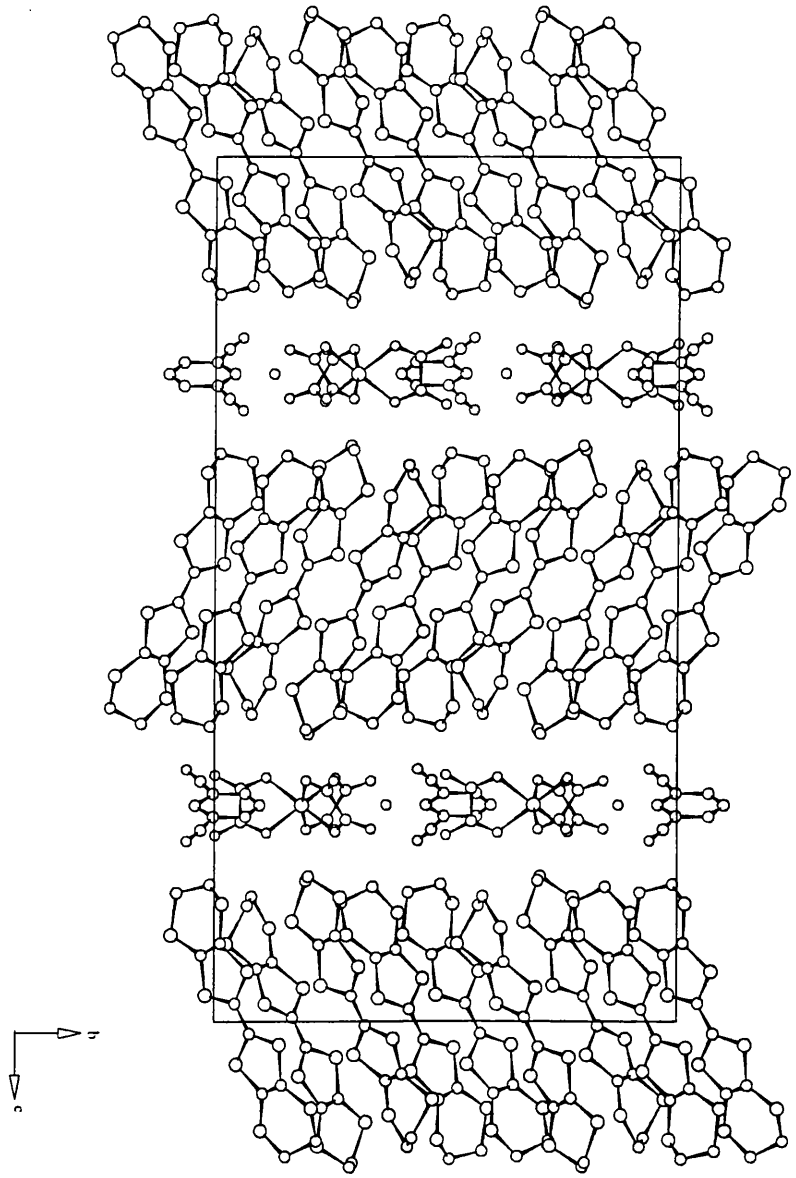

Figure 3.14 The crystal structure of $(BEDT\text{-}TTF)_4NH_4Fe(C_2O_4)_3.C_6H_5CN$ viewed along the a axis.

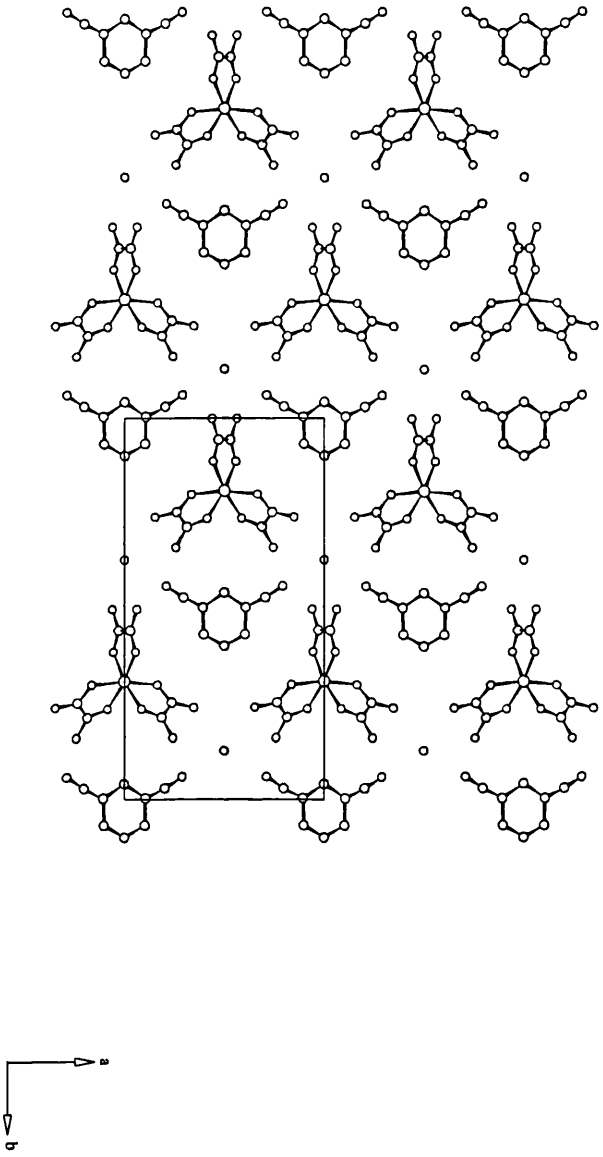

Figure 3.15 The anion layer in $(BEDT\text{-}TTF)_4NH_4Fe(C_2O_4)_3.C_6H_5CN$.

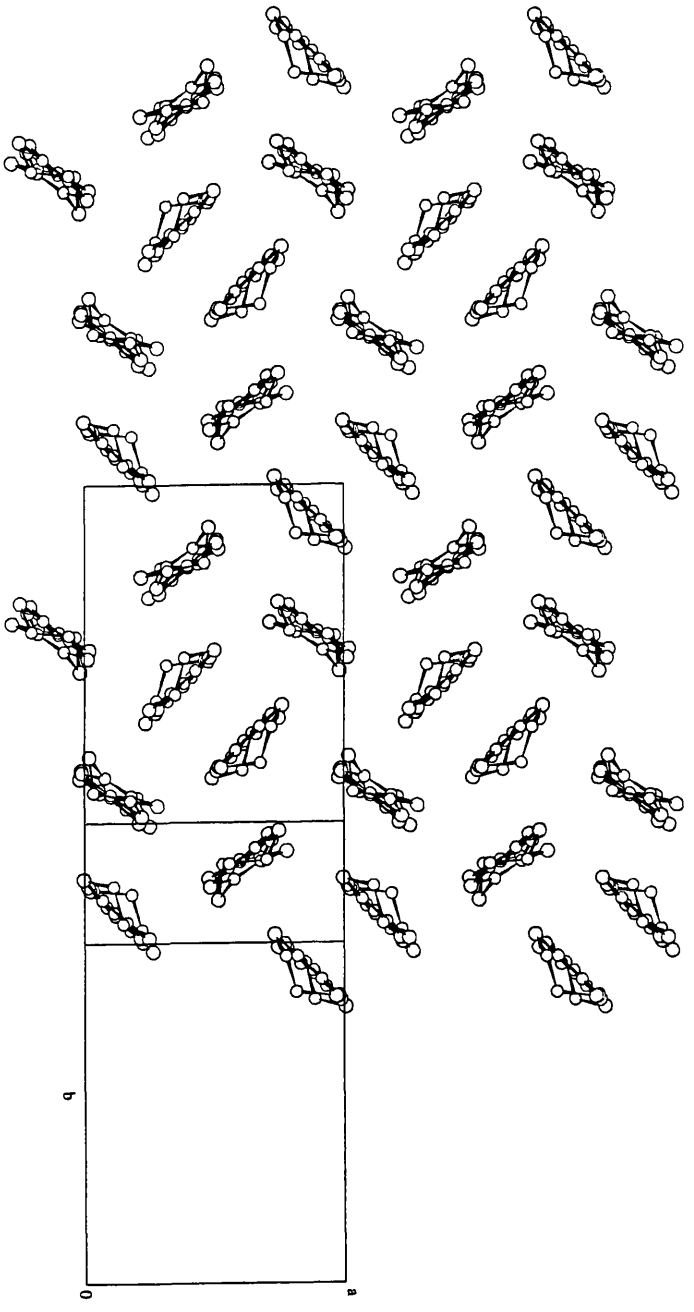

Figure 3.16 The cation layer in (BEDT-TTF)$_4$NH$_4$Fe(C$_2$O$_4$)$_3$.C$_6$H$_5$CN viewed along the long molecular axis.

3.3.2 Electrical Transport.

Conductivity measurements were performed by attaching two gold wire (25μm) probes to the crystal with platinum paint. A current was passed between the probes and the resistance was measured as a function of temperature in the range of 293 - 232K. As the room temperature resistance was very high (~10^6 Ω/cm), the contact resistance was assumed to be negligible. The data collected are illustrated in Figure 3.17.

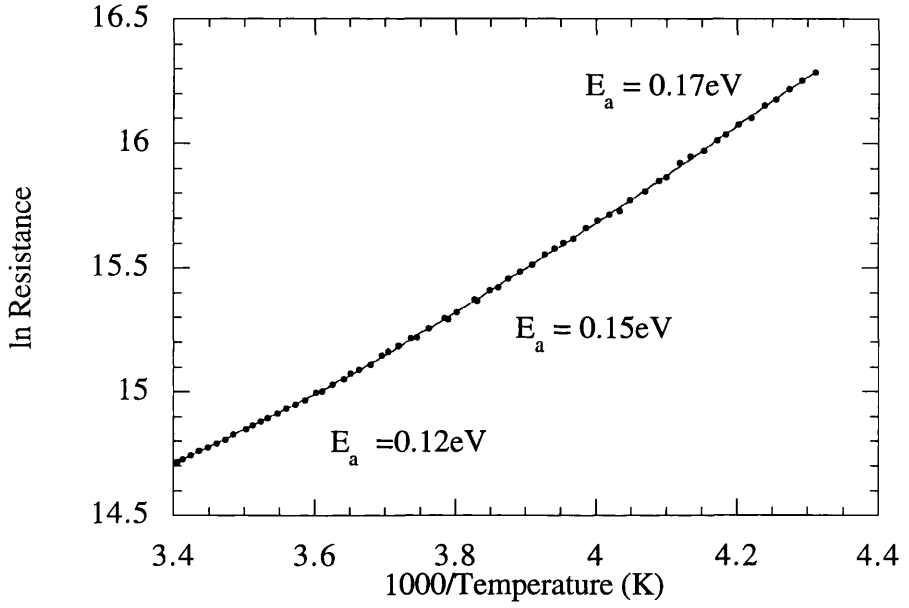

Figure 3.17 The ln Resistance versus 1000/ Temperature for (BEDT-TTF)$_4$NH$_4$Fe(C$_2$O$_4$)$_3$.C$_6$H$_5$CN.

The value of the resistance is inversely proportional to temperature, indicating semi conducting behaviour. An explanation of why the material is semi conducting was given in section 3.2.2. However, rather than the plot having a constant slope, as should be the case in a semiconductor, there is a slight curvature to the graph. A least squares fit to all the data points yields an activation energy of 0.15eV, which is very similar to the value obtained for the potassium analogue. However, a more accurate way of determining the activation energy would be to fit three straight lines in order to

account for the curvature. This yields values for the activation energy of 0.12eV between 293 - 270K, 0.15eV between 270 - 245K and 0.17eV between 245 - 232K.

Therefore, the electrical behaviour of the two compounds reported in this chapter are quite similar. This is to be anticipated as they are isostructural and the sizes of the potassium (1.33Å) and ammonium (1.43Å) cations are very similar. Therefore, there would be very little difference in the band structures of the two materials, resulting in similar electronic properties.

3.3.3 SQUID magnetometery

3.3.3.1 Susceptibility

Magnetic susceptibility data were collected on a randomly aligned polycrystalline sample (16.66mg) contained within a gelatine capsule. Data were collected at fields of 0.5 and 1T, analysis of which yielded the same values for the molar susceptibility. In all cases, the sample was cooled in zero field to 5K, at which point the field was applied and the sample warmed. Data were collected every 3K between 5 and 300K. Figure 3.18 illustrates the inverse of the molar susceptibility versus temperature for the data collected at 0.5 Tesla.

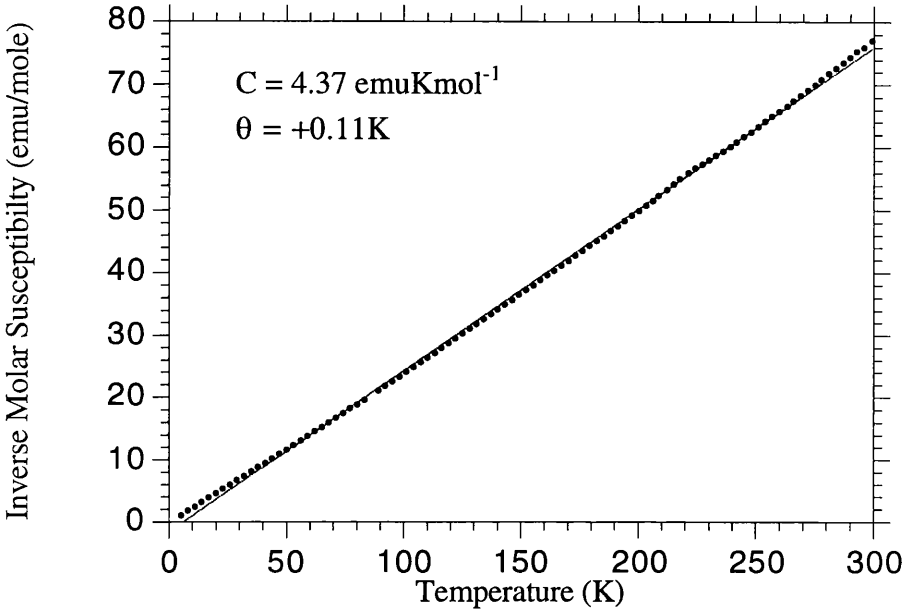

Figure 3.18 The inverse molar susceptibility as a function of temperature for (BEDT-TTF)$_4$NH$_4$Fe(C_2O_4)$_3$.C_6H_5CN. Data collected at 0.5 T.

As can be seen from Figure 3.18, (BEDT-TTF)$_4$NH$_4$Fe(C_2O_4)$_3$.C_6H_5CN is paramagnetic. Curie - Weiss fits to the molar susceptibility give a Curie constant of 4.37 emuKmol^{-1} (S = 5/2) and a Weiss constant of +0.11K, indicating that there is very little, if any interaction between the Fe^{3+} centres. Confirmation that the observed paramagnetic susceptibility is attributable only to the moments on the Fe^{3+} ion can be obtained by subtracting the susceptibility for Fe^{3+} from the total susceptibility data. These results are depicted in Figure 3.19.

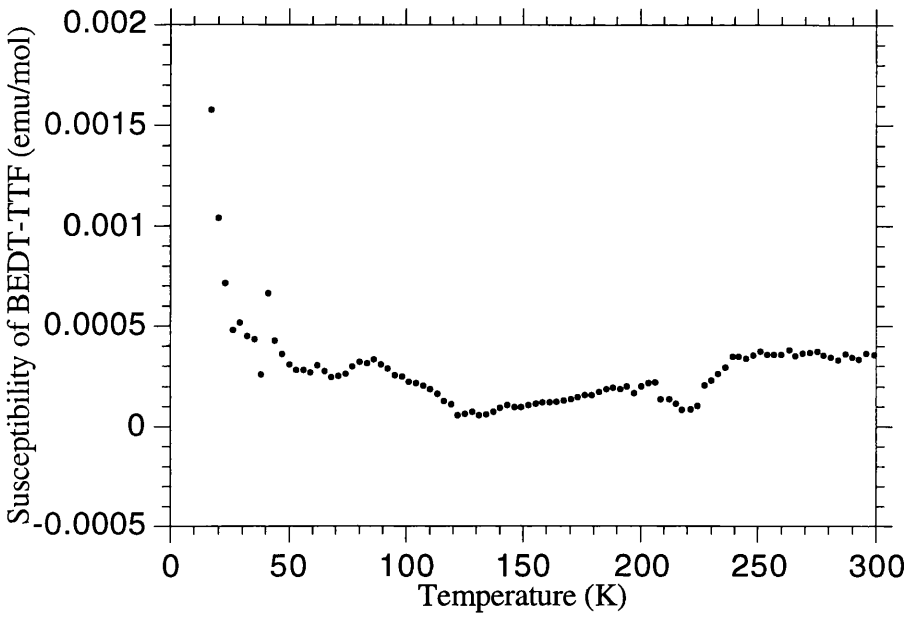

Figure 3.19 The susceptibility of BEDT-TTF in (BEDT-TTF)$_4$NH$_4$Fe(C$_2$O$_4$)$_3$.C$_6$H$_5$CN.

These data reveal that the susceptibility of the BEDT-TTF electrons has a value very close to zero, indicating no appreciable Pauli paramagnetism. However, there is a marked decrease in the susceptibility of the conduction electrons between 100 and 240K which is reproducible at different fields and in different samples. This is also the temperature at which the activation energy from the conductivity data changes. It should be noted though that the magnitude of the susceptibility is very small and therefore it is difficult to separate the signal from the noise.

3.3.3.2 Magnetisation

Magnetisation measurements were performed on the same polycrystalline sample used for the susceptibility measurements. Data were collected at 2K every 0.02T between 0.02 - 0.1T and every 0.5T between 0.5 - 7T. The results obtained are depicted in Figure 3.20.

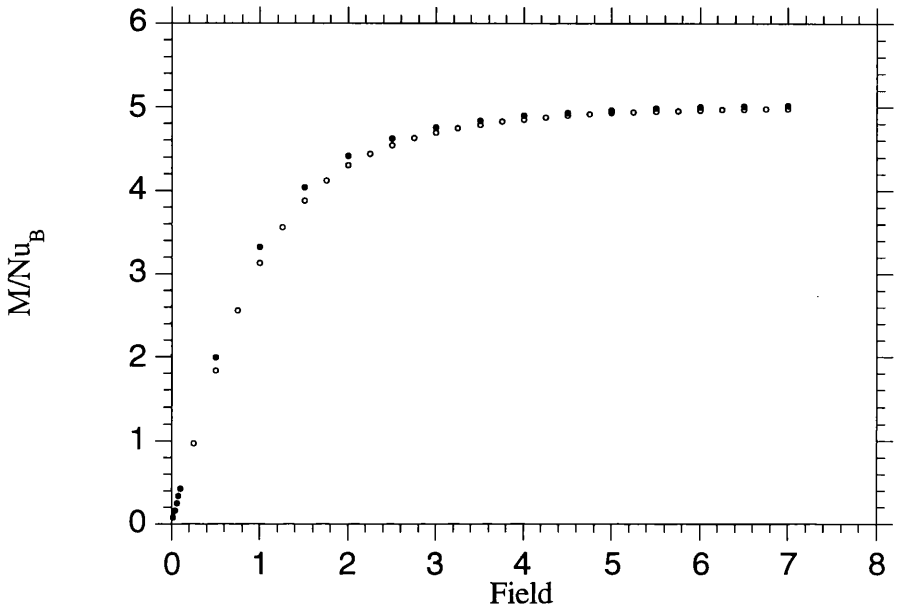

Figure 3.20 The 2K magnetisation of (BEDT-TTF)$_4$NH$_4$Fe(C_2O_4)$_3$.C_6H_5CN. (filled circles) and the theoretical Brillouin function for S = 5/2 and g = 2.

The magnetisation data (filled circles) fit very well to the theoretical values (empty circles). As was observed in the isostructural potassium complex, the magnetisation is linear with field up to 1 Tesla, above which it begins to saturate, until at 3.5T the saturation is almost complete. This offers further evidence that the paramagnetic signal observed is attributable solely to the Fe^{3+} cation.

3.4 Conclusions

A novel packing arrangement of BEDT-TTF molecules has been observed in (BEDT-TTF)$_4$AFe(C_2O_4)$_3$.C_6H_5CN (A = K and NH_4). The structure consists of orthogonal face to face dimers of (BEDT-TTF)$_2^{2+}$ surrounded by six neutral BEDT-TTF molecules. The symmetry of this packing is mirrored in the anion layer where a hexagonal network of AFe(C_2O_4)$_3$ (A = K or NH_4) has formed, reminiscent of the structures observed in $A^+M^{3+}M^{2+}(C_2O_4)_3$ complexes-. The lattice is stabilised by a benzonitrile molecule residing in the centre of the hexagon in the anionic layer. The susceptibilities are dominated by the contribution from the high spin Fe^{3+} ($3d^5$), and obey the Curie - Weiss law to low temperatures. The electrical properties reveal semi conducting behaviour which is explained by the dimerisation of the charged BEDT-TTF ions. This is predicted from band structure calculations.

Chapter 4

The Structure and Physical Properties of $(BEDT\text{-}TTF)_4(H_2O)Fe(C_2O_4)_3.C_6H_5CN$

4.1 Introduction

The two isostructural materials reported in the previous chapter yielded a novel packing arrangement of the BEDT-TTF molecules. This facilitated considerable overlap of the Sulfur orbitals, however semiconducting behaviour was observed due to the formation of spin paired dimers. In order to observe metallic behaviour, it would be necessary to change the band filling in such a way to form a partially filled electronic band. This can be achieved by replacing the A (A = K or NH_4) cation with a neutral molecule. Therefore, crystals were prepared using wet benzonitrile as the solvent in order to dope water into the sites previously occupied by the A cation.

This chapter reports the crystal structure and physical properties of (BEDT-TTF)$_4$(H_2O)Fe(C_2O_4)$_3$.C_6H_5CN. The anion layer is almost identical to those reported in Chapter 3 with the A cation being substituted for H_2O. However, there is a marked difference in the packing of the organic layer.

Conductivity measurements reveal that the material is metallic from room temperature to 8.5K at which temperature it undergoes a transition to the superconducting state. This has been confirmed by magnetic measurements, which also show that at fields above H_{c2}, the susceptibility is dominated by the contribution from high spin Fe^{3+}.

4.2 The Crystal Structure of (BEDT-TTF)$_4$(H_2O)Fe(C_2O_4)$_3$.C_6H_5CN

The crystal data of (BEDT-TTF)$_4$(H_2O)Fe(C_2O_4)$_3$.C_6H_5CN are summarised in Table 4.1. The crystallographic data were collected on a single crystal with dimensions of 0.2 x 0.2 x 0.07mm and indicate that the compound has an empirical formula of $C_{53}H_{37}O_{13}S_{32}Fe$. The unit cell was determined from at least 50 independent reflections giving lattice parameters of a = 10.232(12)Å, b = 20.04(3)Å, c = 34.97(2)Å, $\alpha = 90°$, $\beta = 93.25°$, $\gamma = 90°$. The space group was determined as C2/c.

5110 independent reflections were collected (13774 total) and the structure was refined on a Full matrix least squares fit on F^2 to give an R - factor of 0.0416 (wR2 = 0.0760).

The asymmetric unit consists of two independent BEDT-TTF molecules and half of a $(H_2O)Fe(C_2O_4)_3.C_6H_5CN$ moiety. Despite the stoichiometery of this complex being the same as that reported in $(BEDT\text{-}TTF)_4AFe(C_2O_4)_3.C_6H_5CN$ (A = K or NH_4), the arrangement of the BEDT-TTF molecules is quite different. The bond distances, bond angles and atomic co-ordinates are given in Appendix 1.

The full crystal structure is generated by the application of the relevant symmetry operations and the projection along the a axis is illustrated in Figure 4.1. The structure consists of segregated stacks of organic donor molecules (BEDT-TTF) and the anionic $(H_2O)Fe(C_2O_4)_3.C_6H_5CN$ moiety, as was reported in the previous chapter for the potassium and ammonium analogues. However, the organic stacks are different in two ways: Firstly, the BEDT-TTF molecules are equally spaced which is in contrast to the tetramisation observed in the potassium salt from the same view. Secondly alternate organic layers are twisted with respect to each other, an effect which has only been reported in one other BEDT-TTF complex, α - $(BEDT\text{-}TTF)Ag(CN)_2$, which remains metallic to low temperature, without becoming superconducting [97]. The twist angle of the BEDT-TTF molecules in different stacks is ~121° which is in excellent agreement with the angle between the oxalate ligands in $Fe(C_2O_4)_3$ (ideally 120°). It is therefore postulated that the angle between respective BEDT-TTF stacks is driven by the iron tris oxalate anion.

By removing the organic layer from the diagram, a clearer view of the anion layer can be obtained. This demonstrates that the packing within this layer is almost identical to that observed in the previous examples. That is to say a honeycomb arrangement of $Fe(C_2O_4)_3^{3-}$ and H_2O has formed with a benzonitrle molecule residing in the cavity of

this honeycomb. The benzonitrile molecule is ordered within the cavity resulting in a dipole moment within the layer. However, the adjacent anion layers have equal and opposite dipole moments and hence there is no overall moment. A further consequence of this is that the three fold symmetry has been removed. The aromatic part of the benzonitrile molecule is essentially planar, with a slight distortion out of the plane by 1.2°. The nitrile group is out of the plane by ~11°, which is comparable to the potassium salt. However, in contrast to the potassium analogue, the phenyl group is not in the same plane as the Oxygen atom from the water molecule and the iron ion.

Another feature of the alternate anion layers is the change in chirality. The iron tris oxalate anions are all of the same chirality within the layer, but the next inorganic layer is of opposite chirality. Therefore, there is no overall chirality in the unit cell. The crystals were prepared from racemic $(NH_4)_3Fe(C_2O_4)_3$ and an interesting future experiment would be to prepare crystals from resolved starting materials in order to prepare a chiral molecular superconductor.

Returning to the discussion of the crystal structure of (BEDT-TTF)$_4$(H_2O)Fe(C_2O_4)$_3$.C_6H_5CN there are other issues which must be addressed.

Firstly, the crystals were grown from a solution of $(NH_4)_3Fe(C_2O_4)_3$, C_6H_5CN and H_2O. The electron density of water and ammonium are very similar and so how can we be sure that a water molecule is co-ordinated to to the tris oxalato compound and not an ammonium ion, from the crystallography data? In order to account for this, both possibilities were considered during the structure determination. On replacing H_2O by NH_4^+, there was a large increase in the thermal parameters, thus suggesting the presence of H_2O.

The previous chapter reported two compounds in the (BEDT-TTF)$_4$AFe(C_2O_4)$_3$.C_6H_5CN family, where A is a small cation. Having established

that water is present in the structure, how do we know that a water molecule is present rather than the H_3O^+ cation. This is a very important point as the band filling of the organic layer will be directly affected. Two pieces of evidence suggest the presence of the neutral molecule. Firstly, from the bond lengths of the BEDT-TTF molecules a charge of 3^+ on the organic layer is predicted. Secondly, the surrounding environment of the oxygen atom in the water molecule has C_2 rather than C_3 symmetry. These points will be considered in greater depth in the forthcoming discussion.

The water molecule is co-ordinated to the outer oxygen atoms of the oxalate ligand to form the honeycomb, which consists of three iron tris oxalate moieties and three water molecules. The bond distances associated with this co-ordination are listed in Table 4.2.

O(7) - O(3)	2.95Å *2
O(7) - O(6)	2.93Å *2
O(7) - O(4)	2.81Å *2

Table 4.2. The co-ordination of the water molecule to the oxalate layer in (BEDT-TTF)$_4$(H_2O)Fe(C_2O_4)$_3$.C_6H_5CN.

The co-ordination consists of two short distances (2.81Å) and four longer distances (2.93Å and 2.95Å). Therefore, the octahedral environment is slightly distorted, which is an effect of the ordered benzonitrile molecule. The co-ordination of the oxygen atom is 6, with three of these sites being generated by symmetry. There is a C_2 rotation axis between C(23) - C(23'), thus indicating the presence of H_2O rather than H_3O^+.

Similarly a more detailed picture of the BEDT-TTF layer can be obtained by removing the (H_2O)Fe(C_2O_4)$_3$.C_6H_5CN moiety from the diagram and viewing the structure along the long molecular axis. This reveals a markedly different packing arrangement

to that observed in the potassium and ammonium salts. Instead of forming face to face dimers, the BEDT-TTF molecules pack parallel with respect to each other. However, rather than the organic molecules eclipsing each other, as is the case in the β - phase (section 1.2.3.2), the adjacent stacks are translated in the a direction. The inner organo chalcogenide ring of BEDT-TTF in one stack is directly above the central C - C bond of the adjacent stack. This type of packing has been observed before, most notably in β"- $(BEDT\text{-}TTF)_3Cl_2.2H_2O$, which is a pressure induced superconductor [42]. This packing arrangement facilitates three types of interactions between the two independent BEDT-TTF molecules, AA, AB and BB. The interaction present is dependent upon the direction of the BEDT-TTF stack. In the [110] (the direction of highest conductivity according to band structure calculations), the molecules stack in an ....ABABAB.... fashion. However, orthogonal to this ([001]), the molecules pack in an ....AABBAA....arrangement, as they do in the [130] direction. Consequently there are eight different types of interactions between the BEDT-TTF molecules: along [001] and [130], B**AA**B, A**AB**B and A**BB**A; and along [110], B**AB**A and **ABA**B. Four of these interactions are between independent BEDT-TTF molecules and four between equivalent BEDT-TTF molecules. The short Sulfur - Sulfur contact distances are tabulated in Table 4.3, where the Sulfur atoms with a prime indicate interactions between equivalent BEDT-TTF molecules.

S(1) - S(11)	3.44Å	S(8) - S(11)	3.61Å
S(3) - S(10)	3.63Å	S(10) - S(9')	3.37Å
S(4) - S(11)	3.48Å	S(10) - S(11')	3.50Å
S(4) - S(16)	3.61Å	S(14) - S(15')	3.50Å
S(7) - S(13)	3.33Å	S(16) - S(15')	3.37Å
S(7) - S(15)	3.31Å		

Table 4.3. The short (<3.65Å) Sulfur to Sulfur contact distances in $(BEDT\text{-}TTF)_4(H_2O)Fe(C_2O_4)_3.C_6H_5CN$.

The shortest sulfur - sulfur contact distances between the independent BEDT-TTF molecules are between S(7) and S(15) (3.31Å) and S(7) and S(13) (3.33Å). These are interactions between the Sulfur atoms in the outer chalcogenide ring of one BEDT-TTF molecule and the inner ring of the other BEDT-TTF molecule. This is to be anticipated from the packing of the organic layer. Short contact distances are also observed between equivalent BEDT-TTF molecules, most notably between S(10) and S(9') (3.37Å).

The change in the charge of the acceptor layer from 2^- to 3^- per formula unit results in a corresponding change in charge of the organic layer to 3^+, and hence there is an average charge of $3/4^+$ per BEDT-TTF molecule. This change is reflected in the bond lengths of the BEDT-TTF molecules, analysis of which reveals that there is a small difference in the charge between the two independent BEDT-TTF molecules. By considering the bond lengths of the inner rings and central carbon - carbon double bond, charges of 0.79^+ and 0.80^+ are predicted for the two independent BEDT-TTF molecules. This results in an expected charge of 3.18^+ on the organic layer, which indicates a charge of 3^+ rather than 2^+,thus offering further evidence for the presence of H_2O rather than H_3O^+.

The framework of the oxalate layer is cemented by the formation of Hydrogen bonds between the water molecule and the oxalate ligand. Hydrogen bonding is also present between the donor and acceptor stacks. Table 4.4 lists the Hydrogen bonding present within the lattice (see Table 3.5). Hydrogen atoms 1 - 20 are from the ethylene groups of BEDT-TTF and 24 - 26 from the benzonitrile.

O(1) - H(8A)	2.91Å	O(3) - H(24)	2.72Å
O(1) - H(22B)	2.93Å	O(4) - H(12A)	2.43Å
O(2) - H(8B)	2.43Å	O(4) - H(17B)	2.76Å
O(2) - H(22B)	2.58Å	O(5) - H(22B)	2.63Å
O(3) - H(7B)	2.72Å	O(5) - H(25)	2.89Å
O(3) - H(8A)	2.70Å	O(6) - H(17A)	2.49Å
O(3) - H(12A)	2.72Å	O(6) - H(26)	2.65Å
O(3) - H(13A)	2.40Å		

Table 4.4. Distances between Hydrogen atoms of BEDT-TTF and C_6H_5CN and Oxygen atoms of $C_2O_4^{2-}$ in $(BEDT\text{-}TTF)_4(H_2O)Fe(C_2O_4)_3.C_6H_5CN$.

This data offers evidence that the anion layer is stabilised by the formation of Hydrogen bonds, in particular between the oxalate ligand and the benzonitrile molecule. Thus the solvent molecule is playing a crucial templating role in stabilising the lattice. This situation is similar to that reported in $M^{3+}M^{2+}$ oxalate systems, where the lattice is stabilised by a large organic cation in the cavity of the honeycomb [98].

There is also substantial Hydrogen bonding between the donor and acceptor stacks. Short Hydrogen - Oxygen distances are observed between O(2) - H(8B), O(4) - H(12A) (2.43Å) and O(3) - H(13A) (2.40Å). It is interesting to note that both the inner and outer oxygen atoms of the oxalate ligand form Hydrogen bonds to the terminal ethylene groups of BEDT-TTF.

The packing of the two layers with respect to each other is depicted in Figure 4.4. Only the iron and water molecules of the inorganic layer are illustrated for clarity and these molecules are joined together by a solid line to form a hexagonal array. The BEDT-TTF layer is shown in its entirety. As has been previously discussed the BEDT-TTF molecules stack in three directions within layer, [001], [110] and [130].

This representation shows how the stack of BEDT-TTF molecules along [110] are parallel to the angle between the iron and water entities. However, in the other two directions, there is no corresponding pattern.

The conformation of the independent BEDT-TTF molecules is different. The terminal ethylene groups of BEDT-TTF (A) are in the higher energy boat conformation whereas in BEDT-TTF (B), they are in the chair conformation.

The importance of the docking of the Hydrogen atoms in determining the packing of the BEDT-TTF layer has already been discussed in section 3.3.1. The docking in this lattice shows greater similarity to $(BEDT\text{-}TTF)_4KFe(C_2O_4)_3.C_6H_5CN$ rather than the κ - phase materials. That is to say that the Hydrogen atoms are residing above the Oxygen atoms of the Oxalate ligand (Figure 4.5) rather than above the hole of the honeycomb (which is occupied by Benzonitrile). Despite this similarity, the packing of the organic layers is markedly different in the two salts and a more subtle approach will be required to understand this difference.

Empirical Formula	$C_{53}H_{37}O_{13}S_{32}FeN$
Formula Weight	1979.79
Temperature (K)	120(2)
Wavelength (Å)	0.71069
Crystal System	Monoclinic
Space Group	C2/c
Unit Cell dimensions	a = 10.232(12) Å
	b = 20.04(3) Å
	c = 34.97(2) Å
	β = 93.25°
Volume	7157(13) $Å^3$
Z	4
Density (calculated)	1.835Mg/m^3
Absorption coefficient	1.207 mm^{-1}
F(000)	4016
Crystal size	0.2 x 0.2 x 0.07 mm
θ range for data collection	2.33 to 24.87°
Index ranges	$-8 \leq h \leq 11$ $-22 \leq k \leq 20$ $-39 \leq l \leq 38$
Reflections collected	13774
Independent reflections	5110 [R(int) = 0.1011]
Refinement method	Full-matrix least-squares on F^2
Data / Restraints / Parameters	5094 / 6 / 454
Goodness of fit on F^2	0.661
Final R indices [$I > 2\sigma(I)$]	R1 = 0.0416, wR2 = 0.0760
R indices (all data)	R1 = 0.0982, wR2 = 0.0934
Largest diff. peak and hole	0.651 and -0.439 $e.A^{-3}$

Table 4.1 The crystal data for $(BEDT\text{-}TTF)_4(H_2O)Fe(C_2O_4)_3.C_6H_5CN$.

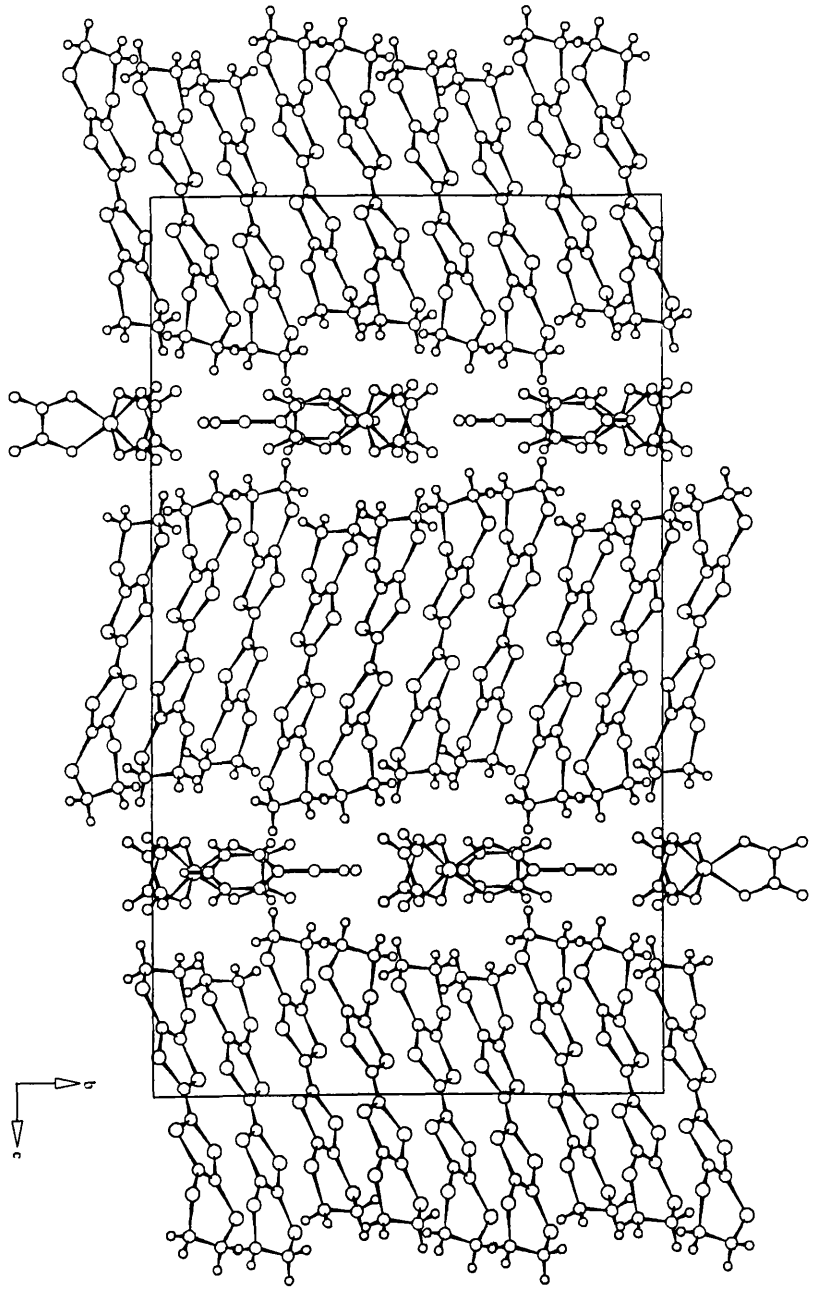

Figure 4.1 The crystal structure of (BEDT-TTF)$_4$(H_2O)Fe(C_2O_4)$_3$.C_6H_5CN, viewed along the a axis.

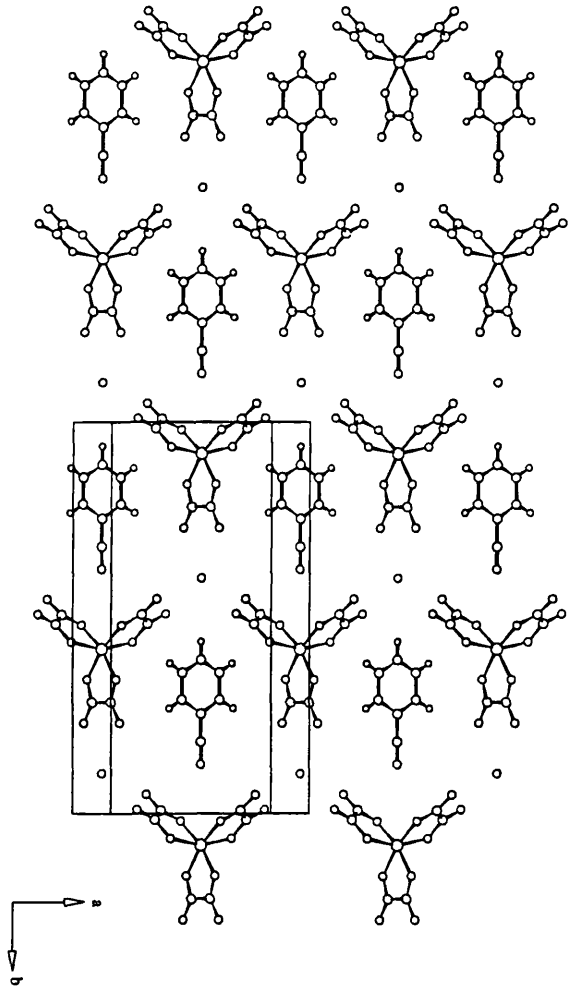

Figure 4.2 The anion layer of $(BEDT\text{-}TTF)_4(H_2O)Fe(C_2O_4)_3.C_6H_5CN$.

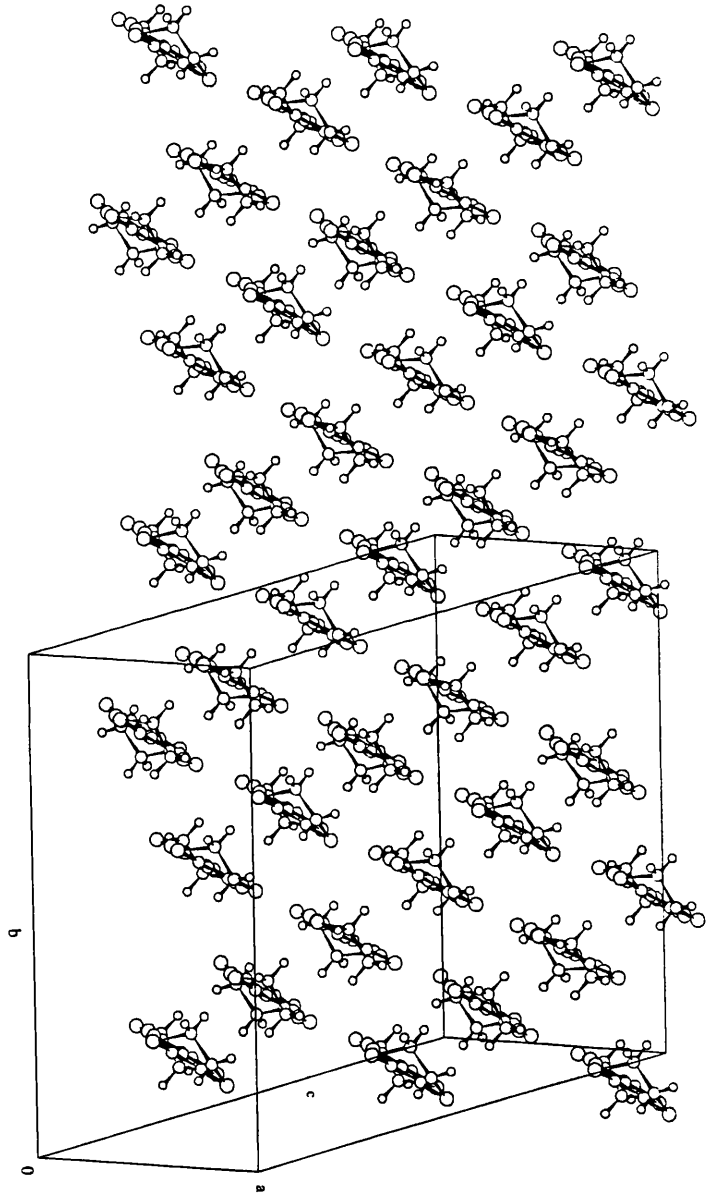

Figure 4.3 The BEDT-TTF layer of $(BEDT\text{-}TTF)_4(H_2O)Fe(C_2O_4)_3.C_6H_5CN$.

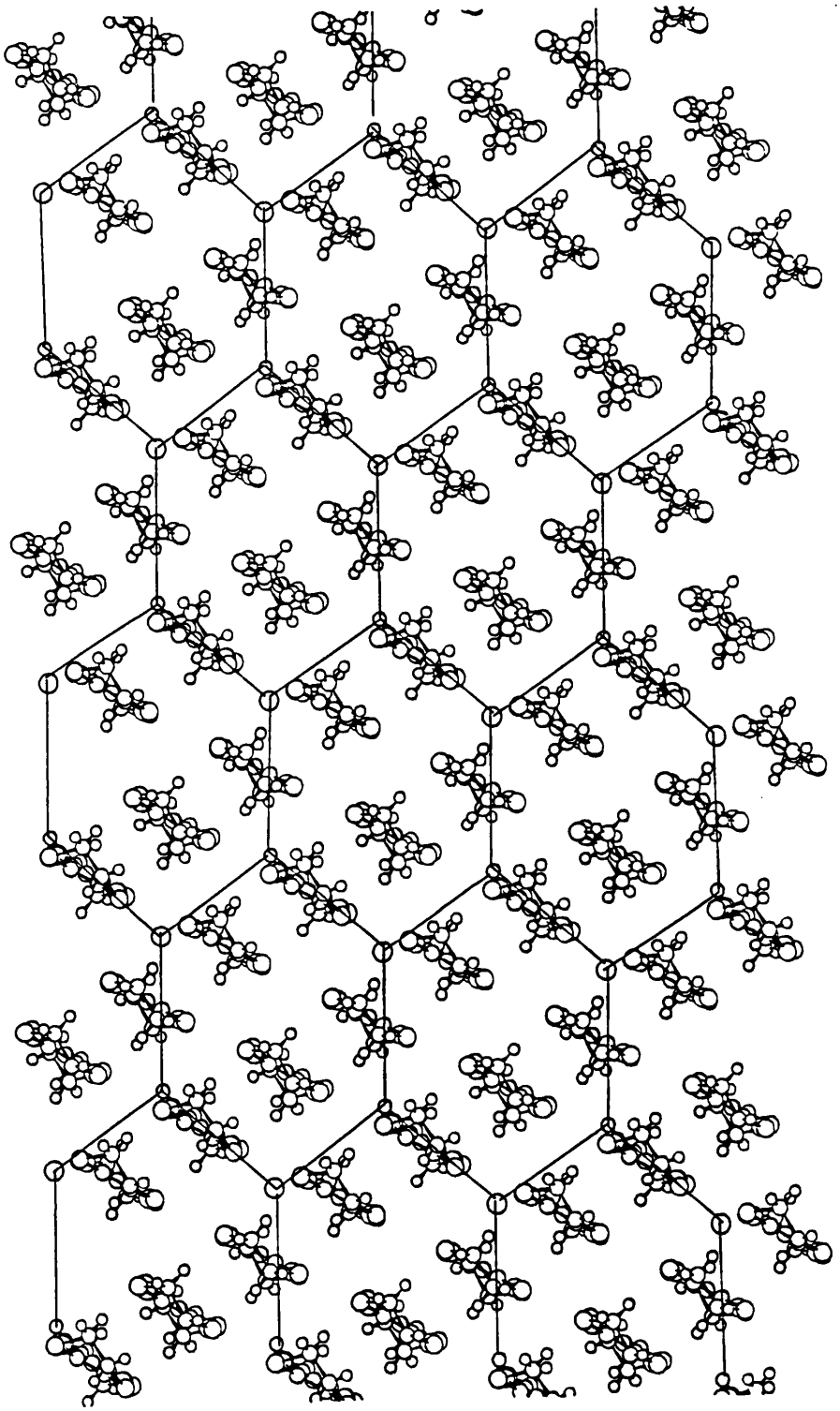

Figure 4.4 The packing together of the organic and inorganic layers in (BEDT-TTF)$_4$(H_2O)Fe(C_2O_4)$_3$.C_6H_5CN. Hexagons join large and small circles indicating Fe and O respectively.

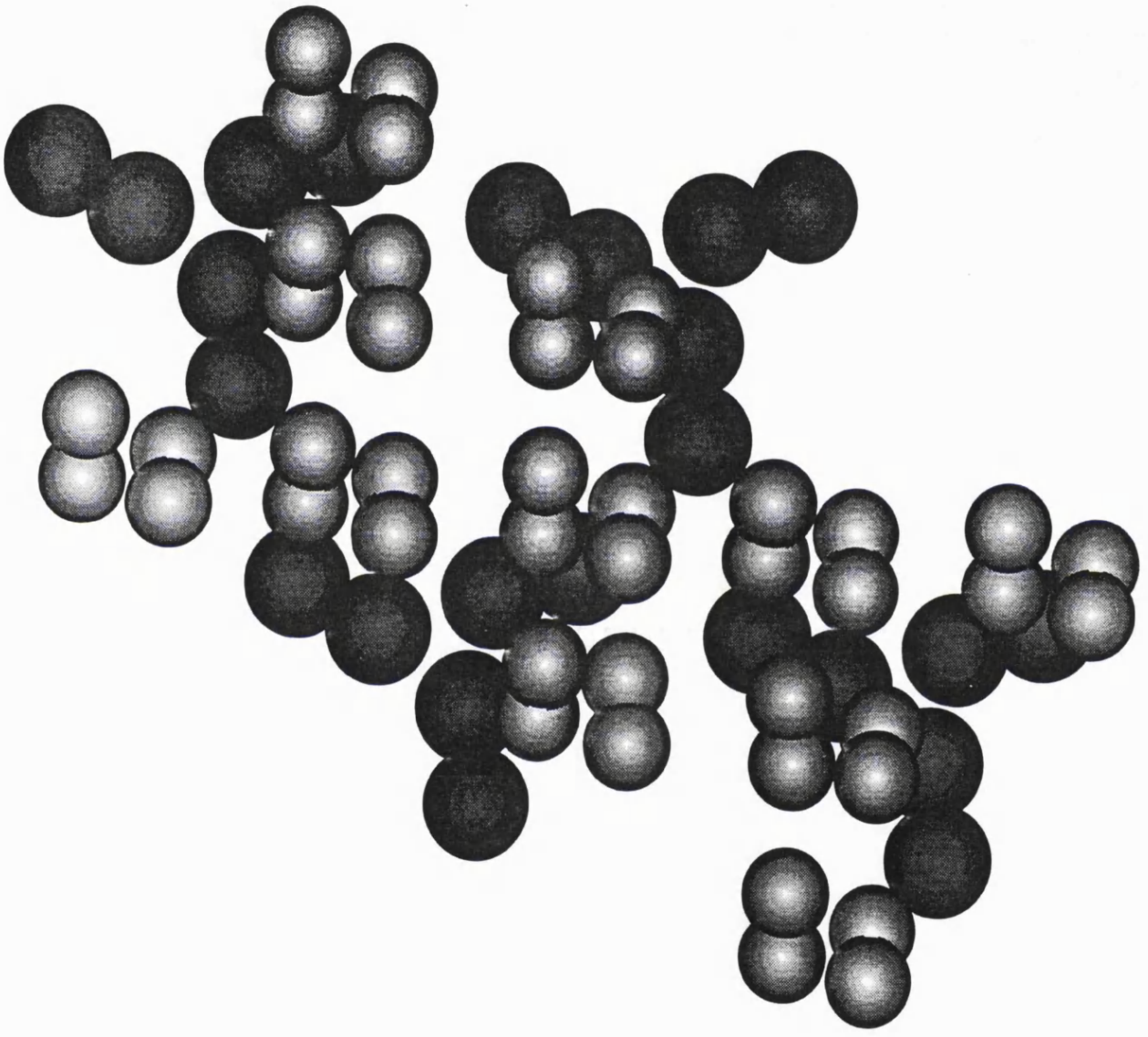

Figure 4.5 The docking of the Hydrogen atoms from BEDT-TTF onto the Oxygen atoms from the Oxalate ligand in $(BEDT\text{-}TTF)_4(H_2O)Fe(C_2O_4)_3.C_6H_5CN$.

4.3 Electrical Transport

Electrical transport measurements were performed by attaching four gold wire (25μm) probes to a single crystal with Platinum paint and measuring the resistance as described in Section 2.3.1. Owing to the needle like morphology of the crystal, it was only possible to measure the resistance in one direction. The quality of the contacts were checked by measuring the two probe resistance at room temperature and the nesting voltages. The contact resistances ranged between 10 to 100Ω and the unnested voltages were always less than 10% of the nested voltages.

Measurements were performed on several crystals. A current of 10μA was passed through the crystal and the voltage drop was measured between the inner two contacts using a precision lock in amplifier (section 2.3.1). The temperature dependent behaviour varied with sample, but the superconducting transition was observed in all crystals with a T_c of 8.5 (± 0.3K).

The results from one such measurement are depicted in Figures 4.6 and 4.7. The resistivity at 200K is ~10^{-2}Ωcm, and this value decreases with temperature to 110K, indicating metallic behaviour. The resistance then increases, probably as a result of a crack in the crystal, and it continues to gradually increase to 40K. Between 20 - 8.5K, the resistance remains reasonably constant, at which point it falls sharply to zero indicating the onset of the superconducting transition. Measurements have also been performed by Jason Caulfield and Mohamedally Kurmoo at The University of Oxford. These results show that metallic behaviour is observed all the way from room temperature to the superconducting transition. A similar temperature dependent profile has also been observed by Helmut Becker at The University of Cambridge.

The average charge per BEDT-TTF molecule is $3/4^{+\cdot}$ which leaves 1.25 electrons in the energy level corresponding to 5/8 the number of the original two electrons. Hence

the electronic band is 5/8 filled. This partially filled energy band results in metallic behaviour being observed.

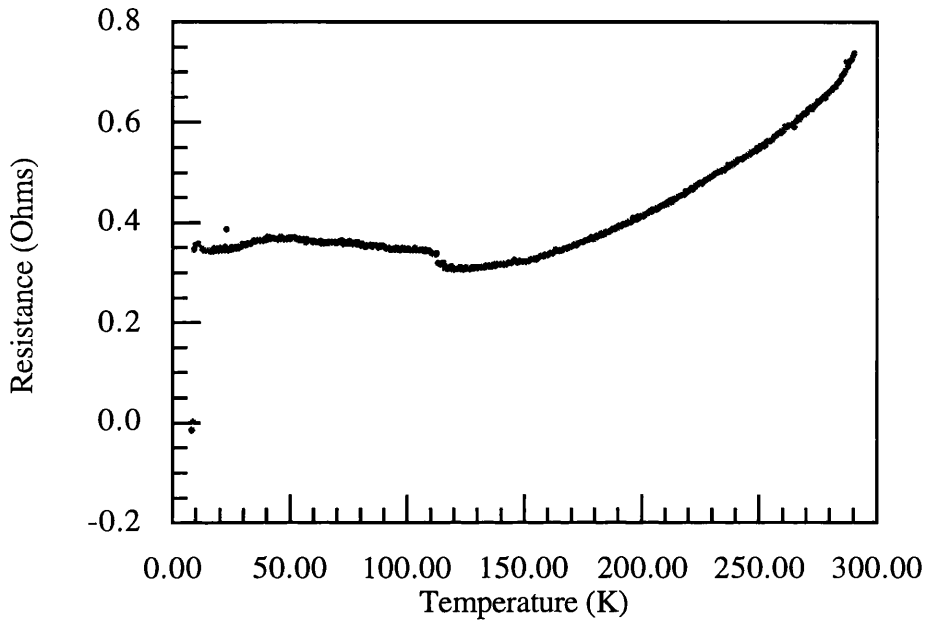

Figure 4.6 Temperature profile of the resistance in $(BEDT\text{-}TTF)_4(H_2O)Fe(C_2O_4)_3.C_6H_5CN$ from 300 - 5K.

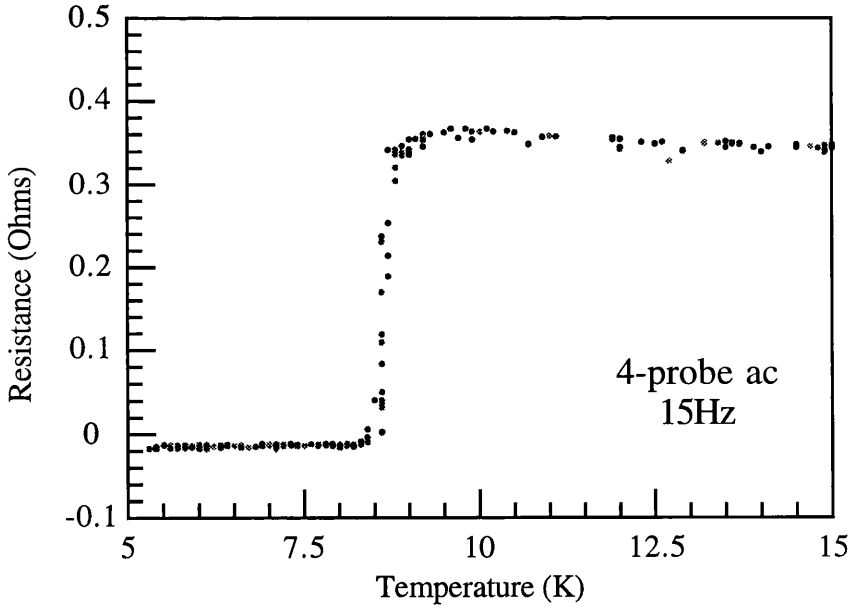

Figure 4.7 The superconducting transition in $(BEDT\text{-}TTF)_4(H_2O)Fe(C_2O_4)_3.C_6H_5CN$.

Attempts to measure the pressure dependence of the conductivity failed to produce any results. This was a consequence of the resistance rising rapidly when contacts were made by the method described in section 2.3.2. This effect has been observed on several crystals, including ones which have been shown to be superconducting using Platinum paint to make contact to the crystal. It is postulated that the reason for the high resistance is a consequence of heating the crystal to high temperature in order to evaporate gold pads onto the sample. This may have the effect of removing the water from the crystal structure and hence changing the physical properties. Single crystal X-ray experiments are planned on the pre-heated samples in order to investigate any structural change after heating. It should be noted that this effect is irreversible.

4.4 Band Structure

Band structure calculations were performed assuming that the only significant contribution to the electronic structure arises from the BEDT-TTF molecules. Thus, the organic layer was generated in a similar way to that described in section 3.2.3.The symmetry operations which serve to generate BEDT-TTF molecules within the same layer in $(BEDT\text{-}TTF)_4(H_2O)Fe(C_2O_4)_3.C_6H_5CN$ are the identity, I (x, y, z) and (1/2+x, 1/2+y, z) which is denoted by the label III in Table 4.5 and Figure 4.8.

The crystal structure of $(BEDT\text{-}TTF)_4(H_2O)Fe(C_2O_4)_3.C_6H_5CN$ yields a multitude of overlap modes depicted in Figure 4.8. This gives a variety of values for the transfer integrals corresponding to the different modes of overlap. These values are given in Table 4.5. The results suggest that the primary direction of the electronic transport will be along [110], with transfer integrals of +188 and +156meV. However, there will also be a significant contribution along [001] as well, with transfer integrals of -111meV. Therefore, two dimensional metallic behaviour is expected.

A	B	+156	B	-III(B)	-46
A	III(B)	+188	B	III - a - b	+187
A	-I(A) + a + b	-48	B	-III(A) + a	-110
A	-III(B) + a	-111	B	III(A)	-92
A	-I(A) + 2a + b	109	B	-III(B) + a	58
A	-III(B)	92			

Table 4.5 Transfer Integrals (meV) of the nearest neighbours for (BEDT-TTF)$_4$ $(H_2O)Fe(C_2O_4)_3.C_6H_5CN$.

The average charge of 3/4$^+$ per BEDT-TTF ion results in a 5/8 filled electronic band. Consequently, the Fermi level cuts an energy band resulting in hole and electron pockets between M-Γ and X-M respectively. This is clearly shown in the diagram of the Fermi surface (Figure 4.10), again indicating two dimensional behaviour

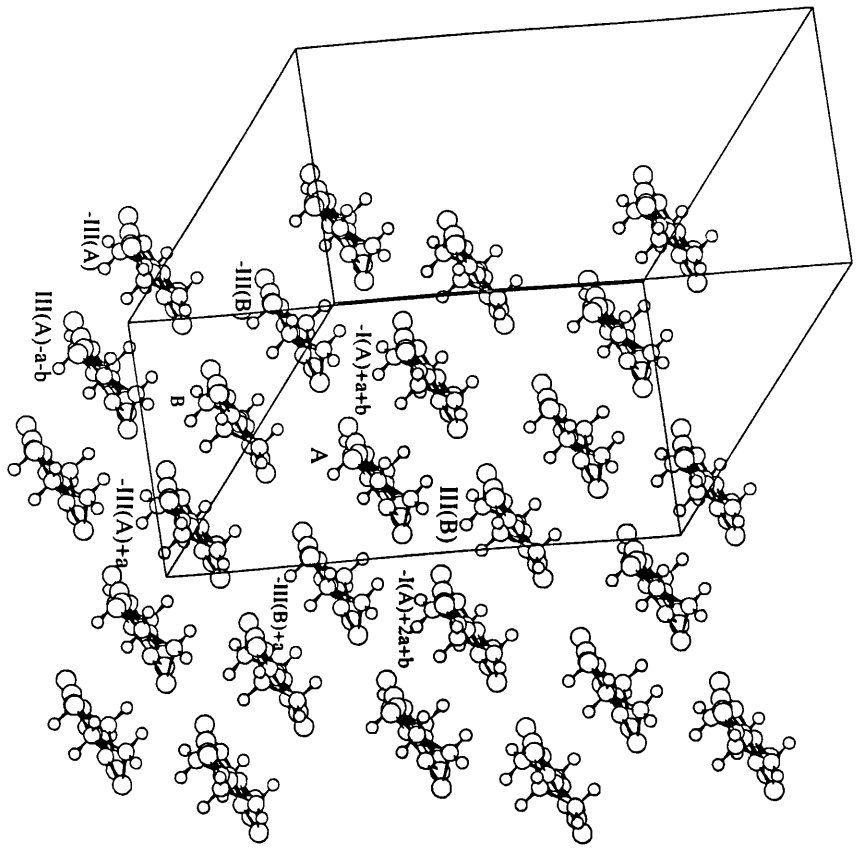

Figure 4.8 The symmetry generated BEDT-TTF molecules within the same layer in $(BEDT\text{-}TTF)_4(H_2O)Fe(C_2O_4)_3.C_6H_5CN$.

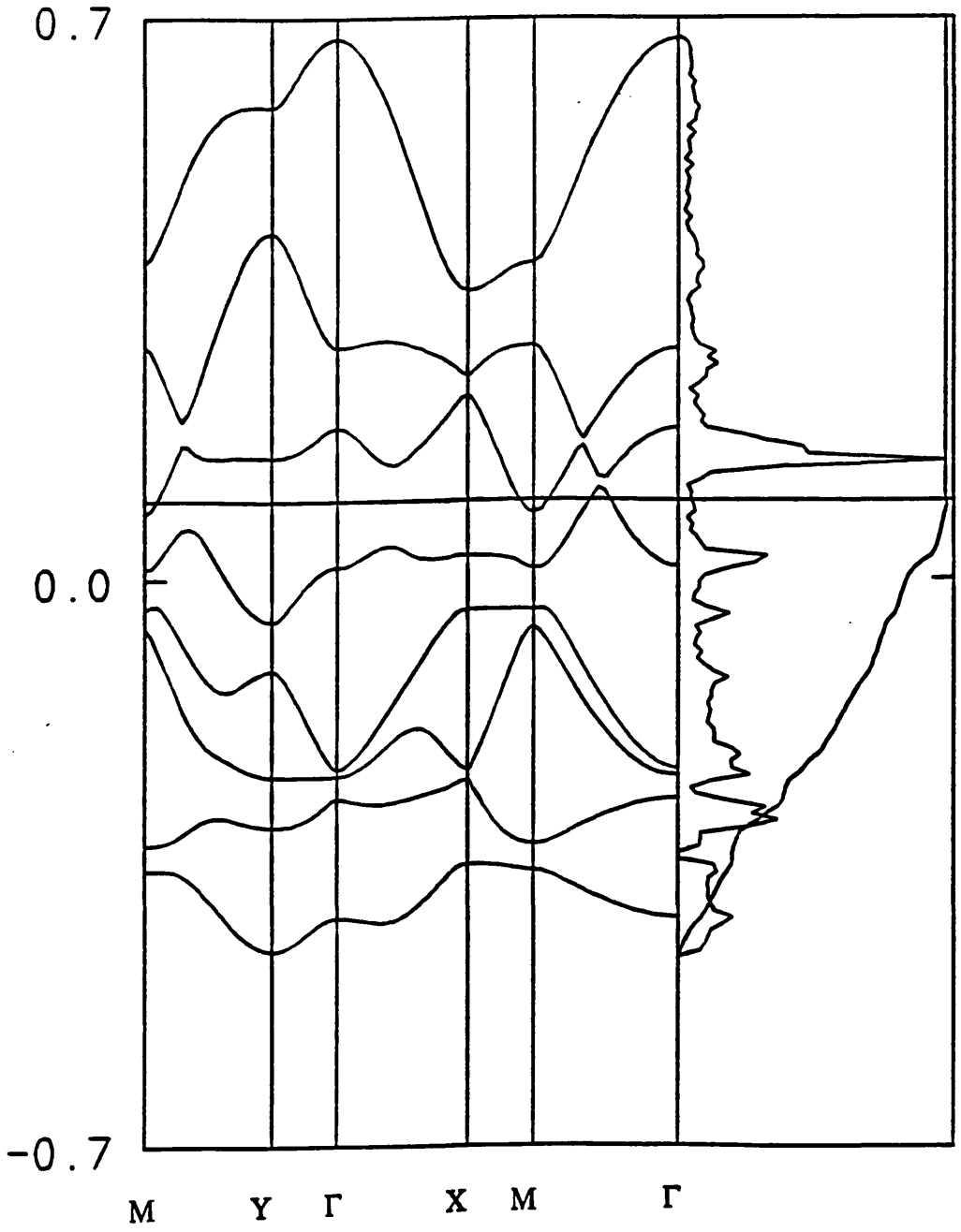

Figure 4.9 The calculated Band Structure of $(BEDT\text{-}TTF)_4(H_2O)Fe(C_2O_4)_3.C_6H_5CN$.

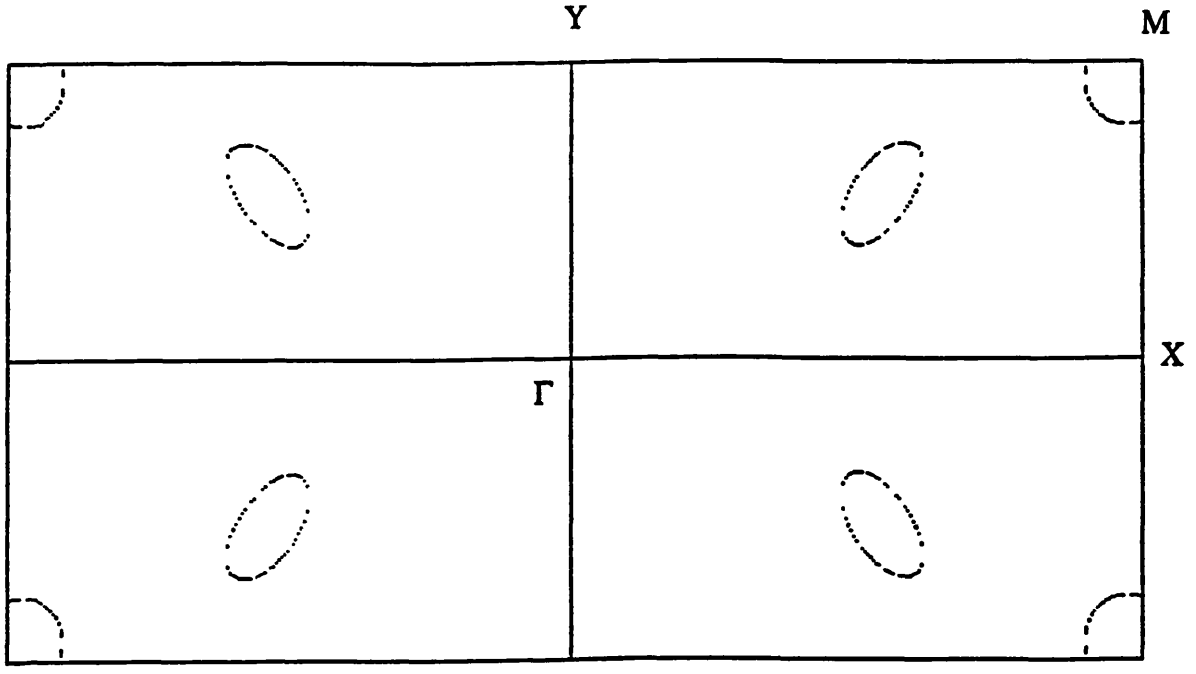

Figure 4.10 The Fermi Surface of (BEDT-TTF)$_4$(H_2O)Fe(C_2O_4)$_3$.C_6H_5CN.

4.5 SQUID magnetometery

4.5.1 Susceptibility

The susceptibility measured is independent of the applied field between 300 - 10K and can be fitted to the Curie -Weiss law to give a Curie constant of 4.44 emuKmol^{-1}. The major contribution therefore comes from the high spin Fe^{3+}. However, below 10K markedly different behaviour is observed as the field is varied. At low field, the susceptibility becomes diamagnetic at ~8.0K, but as the field is increased the diamagnetism decreases, until at 3mT, a Curie tail begins to develop. Figure 4.11 illustrates the data collected from a zero field cooled sample, with a measuring field applied in 1mT increments between 1 - 41mT. At 1mT, the transition to the superconducting state is clearly evident with an onset temperature of 8.0K(±0.2K). As the field is increased, the temperature of the transition decreases, and at 41mT, the transition occurs at 7.2K. Despite a very evident Curie tail, the sample is still superconducting, as has been confirmed by magnetoresistance measurements (section 4.6). This can be observed in greater detail by subtracting the moment due to the Fe^{3+} from the total susceptibility. This results in the transition still be very evident at fields greater than 40mT.

The transition from paramagnetic to diamagnetic behaviour is suppressed when a field of 1 Tesla is applied to the polycrystalline sample. A plot of $1/\chi$ versus temperature is illustrated in Figure 4.12 and fits to the Curie - Weiss law to give a Curie constant of 4.44 emuKmol^{-1} and a Weiss constant of -0.2K.

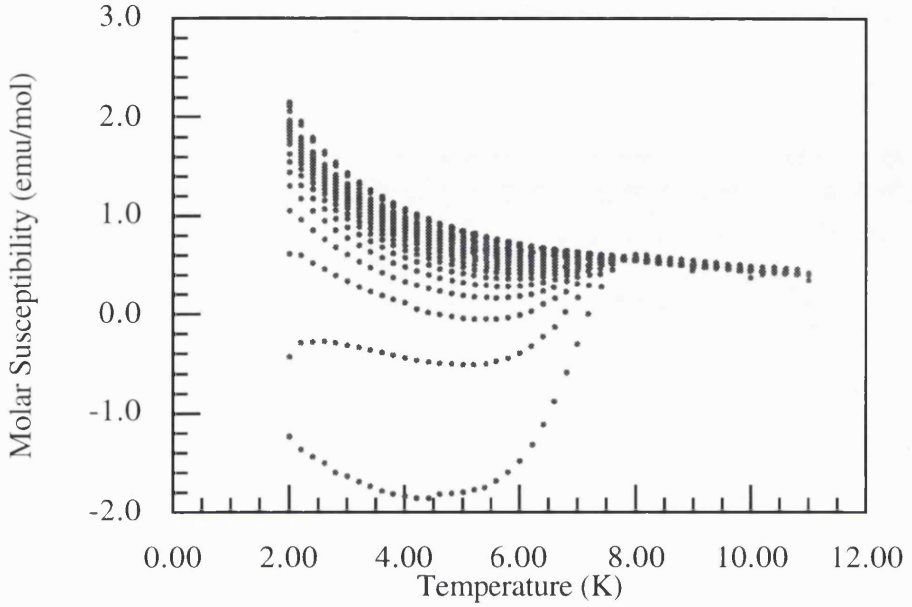

Figure 4.11 The field dependence on the magnetic susceptibility between 1 - 41mT for (BEDT-TTF)$_4$(H_2O)Fe(C_2O_4)$_3$.C_6H_5CN.

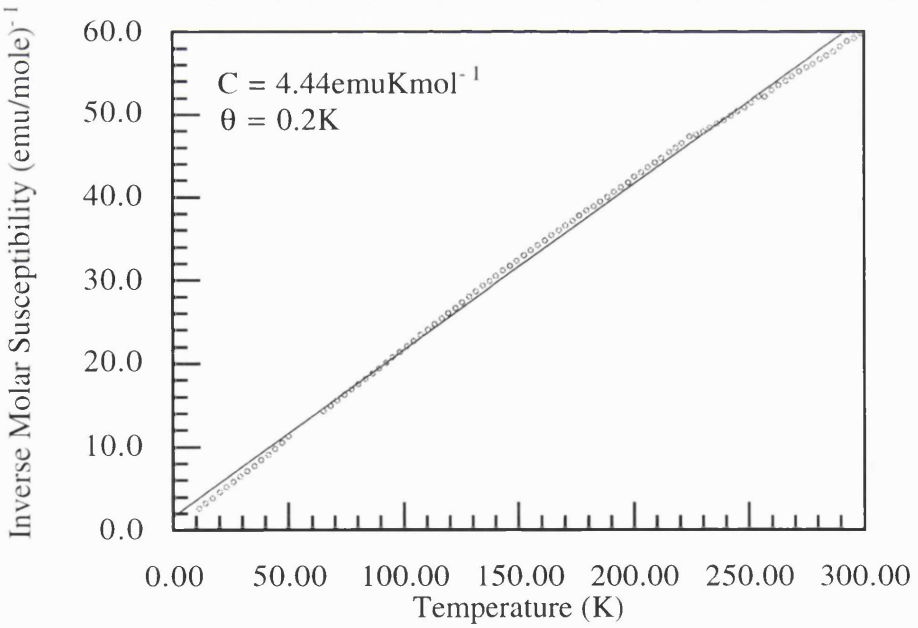

Figure 4.12 Curie Weiss fit to the inverse of molar susceptibility versus temperature for (BEDT-TTF)$_4$(H_2O)Fe(C_2O_4)$_3$.C_6H_5CN. Data collected at 0.5T.

Subtraction of the calculated value for the paramagnetic contribution from the high spin Fe^{3+} to the total susceptibility yields a temperature independent paramagnetic term (Figure 4.13), which is attributable to the Pauli paramagnetism from the metallic BEDT-TTF sublattice.

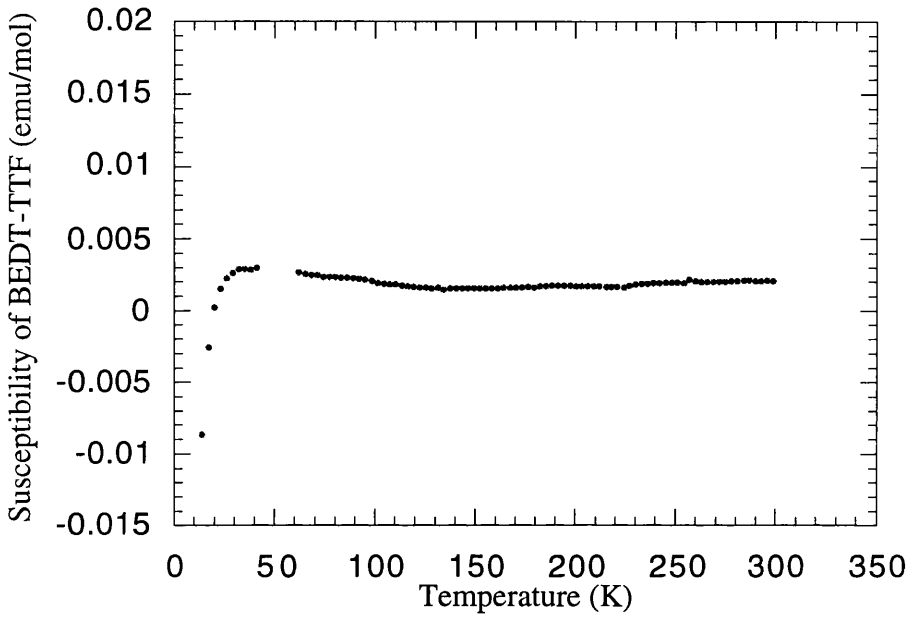

Figure 4.13 Pauli paramagnetism of BEDT-TTF in $(BEDT\text{-}TTF)_4(H_2O)Fe(C_2O_4)_3.C_6H_5CN$.

The density of states at the Fermi level can be calculated via equation 1.22 from the magnitude of the Pauli paramagnetism. This yields a value of $6.80eV^{-1}$, which can be compared to $7.1eV^{-1}$ and $6.5eV^{-1}$ for κ-$(BEDT\text{-}TTF)_2Cu(NCS)_2$ and β-$(BEDT\text{-}TTF)_2I_3$ respectively [99]. The transfer integral can also be calculated via the following equation:

$$t = \mu_B^2 N/(4\chi_p')$$

where χ_p' is the molar susceptibility for one mole of BEDT-TTF molecules. This gives a value of 147meV for the transfer integral which is to be compared with a maximum value of 188meV from the band structure calculations.

Electron Spin Resonance measurements performed by Mohamedally Kurmoo at the University of Oxford confirm the presence of conduction electrons. Two signals have been observed, of which one is assigned to the resonance of Fe^{3+} (observed in both $K_3Fe(C_2O_4)_3.3H_2O$ and $(BEDT\text{-}TTF)_4KFe(C_2O_4)_3.C_6H_5CN$) and the other (broader) signal to the conduction electrons of BEDT-TTF

4.5.2 Magnetisation

Magnetisation data were collected on a polycrystalline sample (3.18mg) of $(BEDT\text{-}TTF)_4(H_2O)Fe(C_2O_4)_3.C_6H_5CN$ contained within a gelatine capsule. The sample was cooled in a zero field to 2K and data were collected as the applied field was increased in increments of 0.25T. The data were collected at fields greater than H_{c2} to ensure that paramagnetic behaviour is observed.

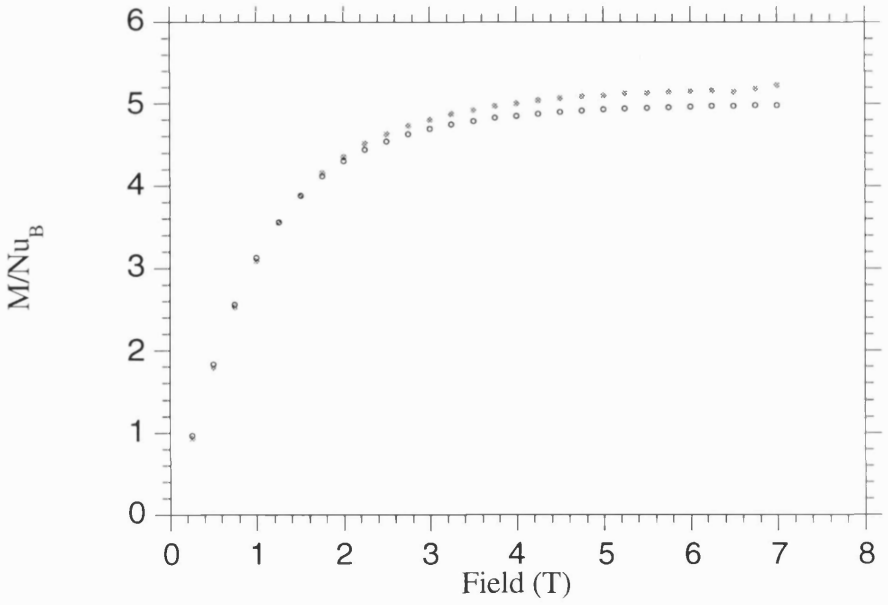

Figure 4.14 The 2K magnetisation of $(BEDT\text{-}TTF)_4(H_2O)Fe(C_2O_4)_3.C_6H_5CN$ (filled circles) and the theoretical Brillouin function for S = 5/2, g =2 (empty circles).

The 2K magnetisation isotherm fits extremely well to a Brillouin function calculated for S = 5/2 and g = 2 (Figure 4.14). However, the data reveal that there is an excess susceptibility, which offers further evidence for Pauli paramagnetism being present. However, a plot of the difference between these two data sets versus field does not give a straight line. Apart from the excess susceptibility, the line shape and saturation values are in very good agreement with the predicted values.

4.5.3 The Meissner Effect

The Meissner effect was detected by cooling the sample in zero field to 1.8K, applying a field of 0.5mT and collecting data points every 0.2K whilst warming to 12K. The sample was then cooled in the same applied field and measured on warming. The difference in the field cooled and zero field data is illustrated in Figure 4.15. The diagram reveals that the susceptibility is identical from 10 to 4K, at which point, there is a divergence between the two data sets. The zero field cooled data becomes more negative as the temperature is decreased, whereas the field cooled data becomes slightly less negative. This corresponds to ~75% perfect diamagnetism.

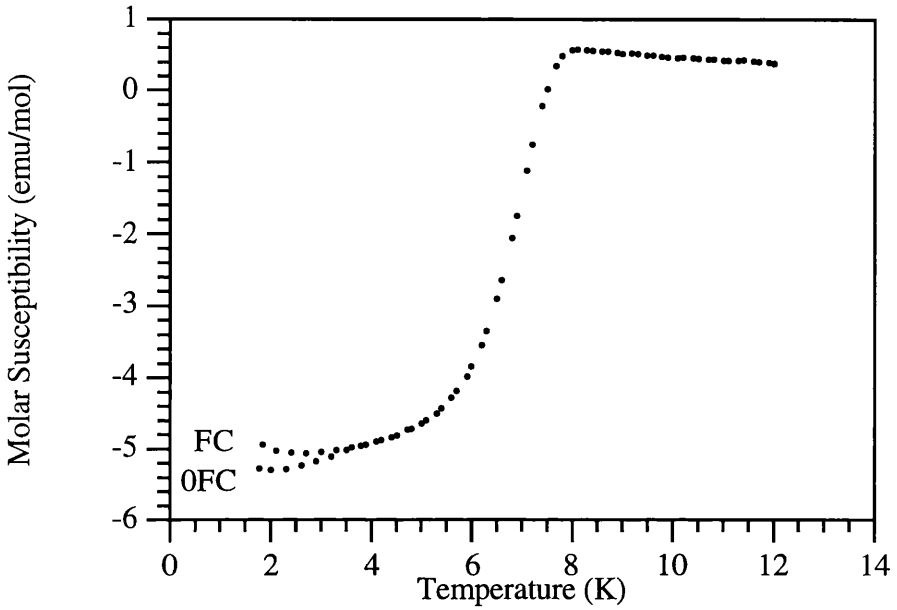

Figure 4.15 The Meissner Effect at 0.5mT for $(BEDT\text{-}TTF)_4(H_2O)Fe(C_2O_4)_3.C_6H_5CN$.

In order to observe the Meissner effect in greater detail, it would be desirable to perform the measurement in a non superconducting magnet, so that the sample can be cooled in a truly zero field and then the earths magnetic field would be applied. Unfortunately, this type of measurement is not possible with the equipment available at The Royal Institution.

4.6 Magnetoresistance

Magnetoresistance measurements were performed on two single crystals of $(BEDT\text{-}TTF)_4(H_2O)Fe(C_2O_4)_3.C_6H_5CN$. Four gold wires (25μm) were attached using Platinum paint and the crystals were positioned normal to each other so that one could be aligned to the applied field whilst the other would be orthogonal. The samples were lowered into the SQUID magnetometer so that they were located in the centre of the pick up coils. The resistance was measured as described in section 2.3.1. Unfortunately, the crystal parallel to the field was cracked whilst cooling and therefore,

it was only possible to collect data on the crystal which was aligned perpendicular to the applied field. Magnetoresistance parallel to the applied field has been measured by Jason Caulfield at the University of Oxford.

The measurement was performed by sweeping the field at isotherms between 2-7K in 0.2K increments. The data obtained are illustrated in Figures 4.16.

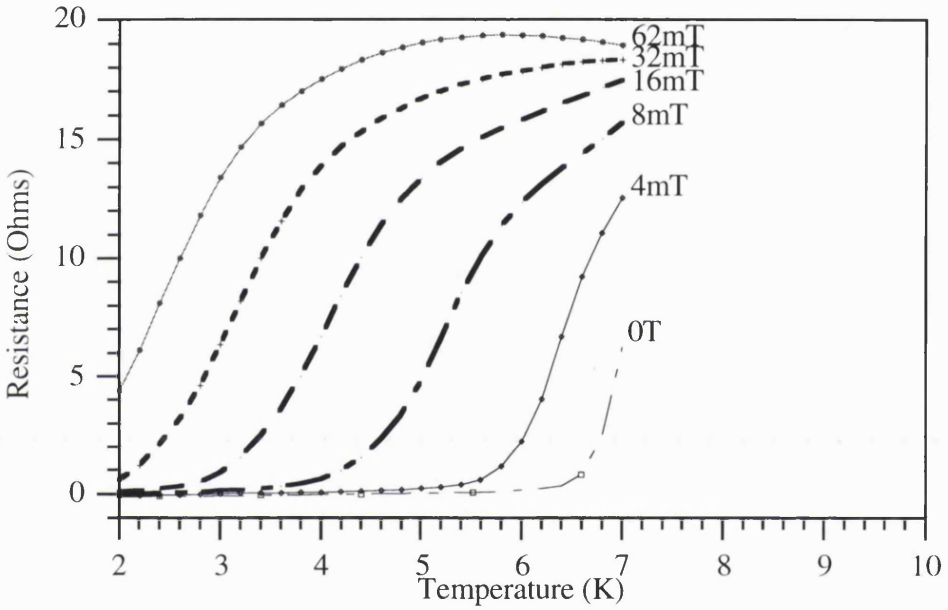

Figure 4.16 The magnetoresistance at selected fields of $(BEDT\text{-}TTF)_4(H_2O)Fe(C_2O_4)_3.C_6H_5CN$ perpendicular to the long axis.

The transition temperature to the superconducting state is reduced with the application of a magnetic field, as is expected. As the field is increased, T_c decreases until at a field of 62mT the sample does not become superconducting at 2K. However, there is still a large drop in the resistance and at lower temperatures, the material will superconduct. A general trend is that the superconducting transition broadens as field is increased. This effect has also been observed in the data collected at Oxford with the field being applied

parallel to the long axis [100] and has been observed in other quasi two dimensional BEDT-TTF salts [101].

4.7 Conclusions

The anionic layer is different to that observed in (BEDT-TTF)$_4$AFe(C_2O_4)$_3$.C_6H_5CN (A = K or NH_4) in two ways. Firstly, the monpositive cation has been replaced with a neutral water molecule, directly affecting the band filling of the organic layer and secondly, the benzonitrile molecule is ordered. These slight differences have had a significant effect on the packing of the organic layer. The BEDT-TTF molecules pack in the β" - phase and the conduction electrons are not localised.

The conductivity measurements demonstrate that it is possible to observe superconductivity within a lattice which contains localised spins. More insight into this has been obtained by magnetic measurements which indicate that at low field (1mT) the material is a superconductor, but as the field is increased the paramagnetic signal attributable to the localised spins becomes more predominant. Magnetoresistance measurements indicate that the compound is still superconducting when a paramagnetic signal is observed in the susceptibility data. At fields greater than H_{c2}, the susceptibility is dominated by the $3d^5$ high spin Fe^{3+}, although there is a signal attributable to Pauli paramagnetism of the conduction electrons.

The derived Fermi surface from band structure calculations consists of two dimensional hole and electron pockets. High Field magnetoresistance measurements are currently underway to deduce the experimental Fermi surface.

Chapter 5

The Physical Properties of other charge transfer salts based upon BEDT-TTF.

Chapter 5 Other Charge Transfer Salts based upon BEDT-TTF

5.1 Introduction

The preceeding two chapters have given a detailed description of three compounds prepared and investigated throughout this research project. It is the intention of this chapter to collate together the products synthesised and the information obtained on other members of the (BEDT-TTF)$_x$[M(C_2O_4)$_3$]$_y$ family and products obtained from BEDT-TTF with squarate anions.

The preliminary results obtained on three of these compounds, are of particular interest and offer the possibility of further study. One of these compounds is based upon the superconducting phase with subtle variations in the solvent conditions. The other two compounds have been prepared from mixtures of BEDT-TTF and $K_3Cr(C_2O_4)_3.3H_2O$ and $(PPh_4)_3Fe(C_2O_2S_2)_3$ respectively in Benzonitrile.

5.2 Crystals grown from BEDT-TTF and $A_3Fe(C_2O_4)_3.3H_2O$

The previous chapters have reported the fascinating electrical properties of the (BEDT-TTF)$_4$A$Fe(C_2O_4)_3.C_6H_5CN$ series of compounds. In order to explore this family of compounds fully, the synthetic conditions have been systematically varied, resulting in the formation of other novel phases. This section will discuss the preparative conditions used to synthesise the materials and their resulting electrical properties.

5.2.1 Crystals grown from BEDT-TTF and $Na_3Fe(C_2O_4)_3.3H_2O$

5.2.1.1 Introduction

Chapter 3 reported the synthesis, structure and physical properties of (BEDT-TTF)$_4$AFe(C_2O_4)$_3$.C_6H_5CN (A = K or NH_4). The formation of these materials yielded a novel packing arrangement of the BEDT-TTF layer. It was postulated that the symmetry of the anion layer (the hexagonal network) had driven the packing of the BEDT-TTF layer via Hydrogen bonds. A critical component of the anion layer is the counter cation, A, which is co-ordinated to the oxalate complex to form a hexagonal layer network. In order to investigate the effect of the cation on the hexagonal symmetry, sodium tris(oxalato)ferrate was used as the electrolyte.

5.2.1.2 Electrical Transport

The electrochemical synthesis yielded hexagonal plates which allowed conductivity experiments to be performed along the three crystal axes. Four probe conductivity measurements could be performed in two directions, whilst the two probe method was employed to measure the temperature dependent resistance through the plate. Data were collected between 300 - 140K and the results obtained are illustrated in Figure 5.1.

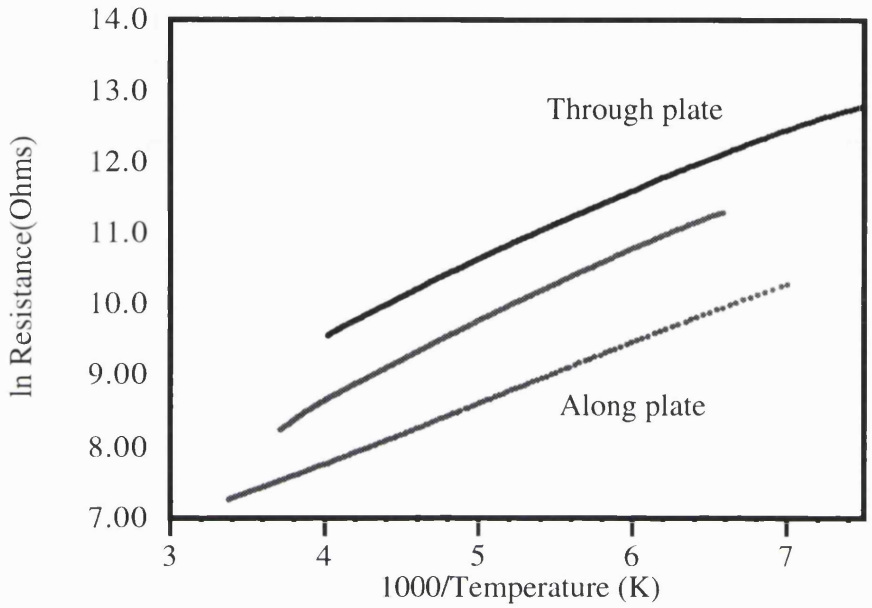

Figure 5.1 The ln resistance versus 1000/ Temperature for the hexagonal plate obtained from a solution of BEDT-TTF and $Na_3Fe(C_2O_4)_3$ along the three crystal axes.

The room temperature resistivity is ($\sim 2*10^3\ \Omega cm^{-1}$), and this value increases as temperature is reduced, indicating semiconducting behaviour. Figure 5.1 illustrates a linear graph of the natural log of the resistance versus inverse temperature for the three data sets. The three curves are parallel to each other which suggests that the activation energy is isotropic. Fitting of these curves by least squares gives an energy gap of 0.146eV (E_a = 0.073eV) between the electronic bands.

5.2.2 Crystals grown from BEDT-TTF and $K_3Fe(C_2O_4)_3.3H_2O$

5.2.2.1 Introduction

Chapter 4 reported the synthesis, structure and physical properties of the first molecular superconductor containing localised moments, $(BEDT\text{-}TTF)_4(H_2O)Fe(C_2O_4)_3.C_6H_5CN$. The replacement of K or NH_4 for water in the anion layer is critical for changing the band filling and the packing of the BEDT-TTF layer. In order to prepare crystals of the highest possible quality, the synthetic conditions had to be optimised. The concentration of the electrolyte and the amount of water added to the solvent were varied and the latter approach led to the formation of crystals with a plate like morphology.

5.2.2.2 Electrical Transport

The experiment yielded crystals with a plate like morphology which were of a sufficient size to perform four probe conductivity measurements along two of the three crystal axes. Gold wire (25μm) was attached to the crystal using Platinum paint and the temperature profile of the resistance was measured between 300 - 150K.

The room temperature resistivity was $\sim 3*10^3 \Omega cm^{-1}$ and this value increased as the temperature was lowered, suggesting semiconducting behaviour. A plot of the natural log of the resistance versus 1000/ Temperature yields three straight lines which are parallel to each other (Figure 5.2). A least squares fit to these lines gives an activation energy of 0.12eV.

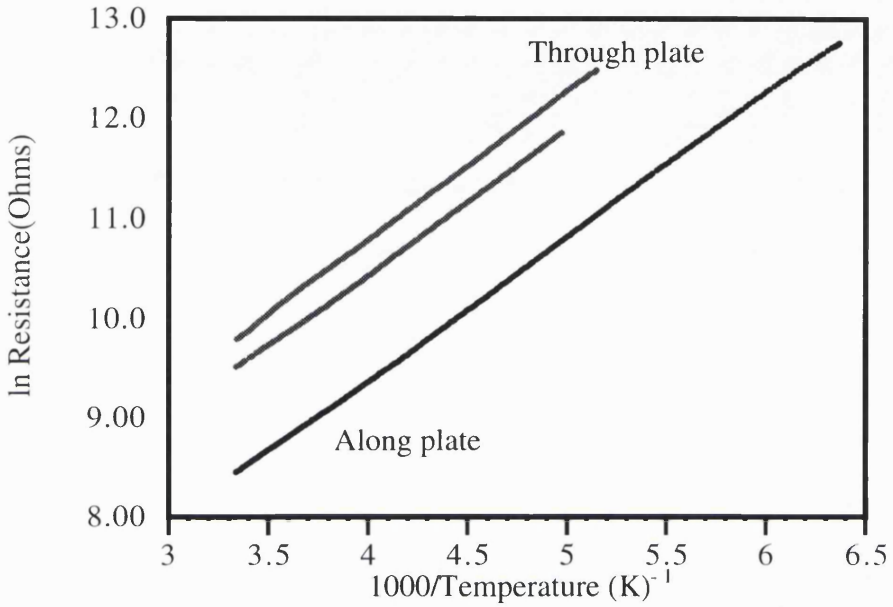

Figure 5.2. ln Resistance versus 1000/ Temperature for the crystals obtained from a solution of BEDT-TTF and $K_3Fe(C_2O_4)_3$ in wet Benzonitrile along the three crystal axes.

5.3 Crystals grown from BEDT-TTF and $A_3Co(C_2O_4)_3.3H_2O$

5.3.1 Introduction

The bulk of this thesis has been concerned with $(BEDT\text{-}TTF)_xFe[(C_2O_4)_3]_y$ systems, with a multitude of physical properties being realised, which include semiconducting, metallic and superconducting behaviour. This series of results has opened up a multitude of other materials which could be prepared to enable the physics of these systems to be explored fully. One such alternative is to replace the iron(III) centre for another transition metal and see what effect this has on the physical properties. Consequently, charge transfer salts have been formed with BEDT-TTF and $Co(C_2O_4)_3^{3-}$. This has the effect of

changing the number of localised spins on the anion from a high spin d^5 complex to low spin d^6, without changing the size, shape or charge of the anion.

5.3.2 Electrical Transport

The crystals obtained from the potassium salt (section 2.2.4) had a spear like morphology and were only of a sufficient size to perform two probe measurements. The room temperature resistivity was very high (~$6*10^6$ Ωcm^{-1}) and therefore the contact resistance is assumed to be negligible. This value increased as temperature was lowered and a plot of the ln resistance versus inverse temperature is given in Figure 5.3.

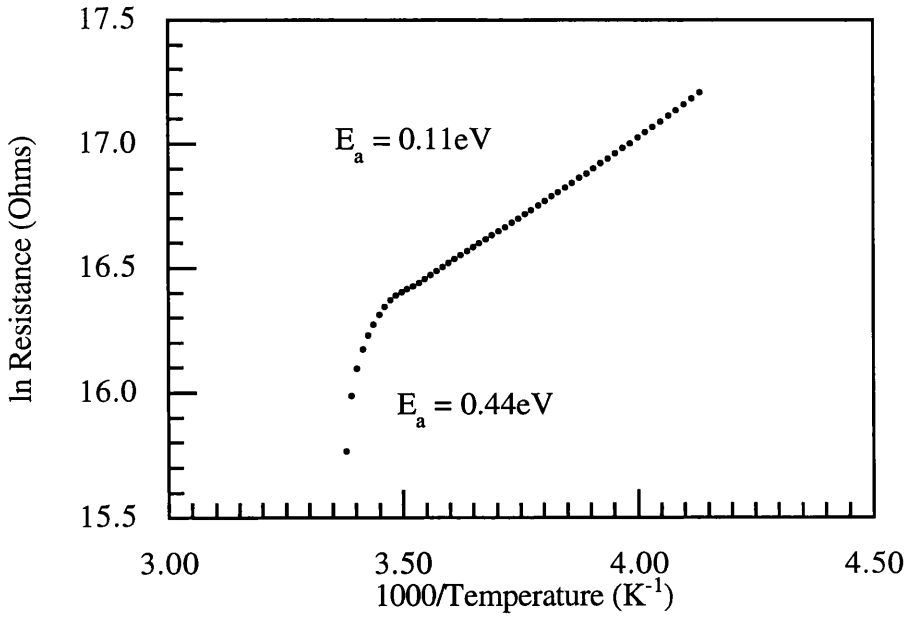

Figure 5.3. ln Resistance versus 1000/ Temperature for a crystal grown from BEDT-TTF and $K_3Co(C_2O_4)_3.3H_2O$ in benzonitrile.

Clearly there are two separate regions to which the curve must be fitted. The slope of the line changes drastically at ~ $0.0035K^{-1}$ which is indicative of a change in the activation energy. Least squares fit to these lines yields values for the activation energy of 0.44eV between 300 to 290K and 0.11eV between 289 to 245K, suggesting a phase transition at 289K.

The crystals prepared from $(NH_4)_3Co[(C_2O_4)_3].3H_2O$ had a diamond like morphology and a two probe conductivity experiment was performed upon them. Data were collected between 298 and 254K and the results obtained are illustrated in Figure 5.4.

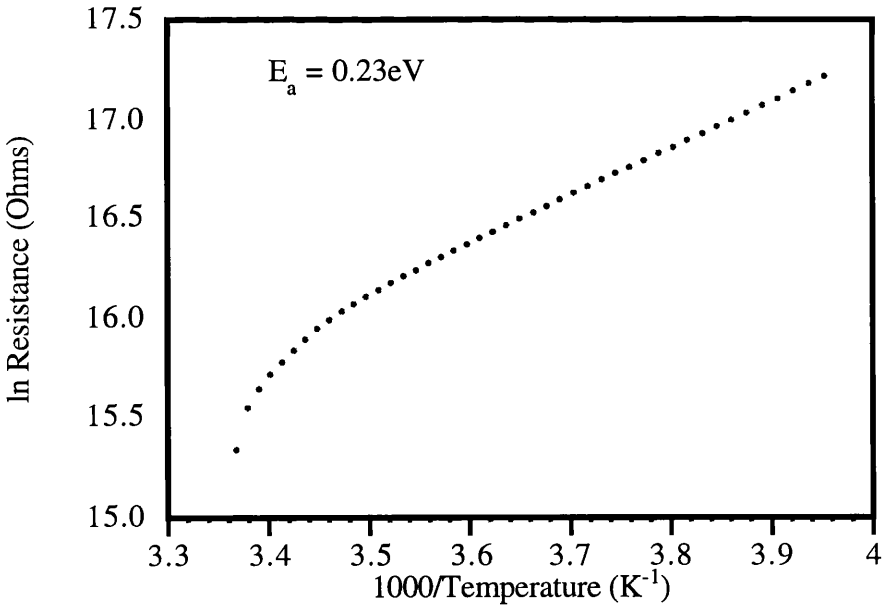

Figure 5.4. ln Resistance versus 1000/ Temperature for the crystals grown from a benzonitrile solution of BEDT-TTF and $(NH_4)_3Co(C_2O_43).3H_2O$

The temperature dependent resistivity in this compound shows similar behaviour to that observed in the crystals grown from the potassium salt. That is to say that at 290K there is

a marked change in the slope of the ln Resistance versus inverse temperature curve suggesting a phase transition at a similar temperature to the potassium salt. However, despite having a similar ambient temperature resistance, the activation energy at temperatures beneath the transition (0.23eV) in the ammonium salt is over twice that observed in the potassium salt.

5.4 Crystals grown from BEDT-TTF and $K_3Cr(C_2O_4)_3.3H_2O$

5.4.1 Introduction

Another possibility for analysing the effect of magnetic anions on electrical properties is to prepare charge transfer salts with $Cr(C_2O_4)_3^{3-}$. This will change the d electron configuration to d^3, again with the shape and charge remaining constant.

The synthesis of these compounds proved to be considerably more challenging than their iron counterparts. However, in the final weeks of this research project, crystals have been obtained with comparable morphologies to their iron counterparts have using $K_3Cr(C_2O_4)_3.3H_2O$ (100mg) and 18 - crown - 6 ether (160mg) as the electrolyte. Unfortunately, there has been no time to characterise these materials, but their morphologies suggest that they are $(BEDT\text{-}TTF)_4KCr(C_2O_4)_3.C_6H_5CN$ (diamond), $(BEDT\text{-}TTF)_4(H_2O)Cr(C_2O_4)_3.C_6H_5CN$ (needle) and the Chromium analogue of the material discussed in section 5.2.2.2 (plate). Another material with a needle like morphology has also been isolated and the physical properties of this compound are discussed in the following sections.

5.4.2 Crystallography

Unfortunately, due to twinning of the crystals it has not been possible to solve the crystal structure. However, it has been possible to deduce the lattice parameters of two separate crystals, both with needle morphology at 300 and 150K and these results are listed in Table 5.1.

	300K	150K
a	4.484Å	10.3Å
b	10.938Å	19.4Å
c	35.86Å	35.86Å
α	90°	90°
β	90°	90°
γ	90°	90°

Table 5.1 Crystallographic lattice parameters for the crystals grown from BEDT-TTF and $K_3Cr(C_2O_4)_3.3H_2O$ in wet benzonitrile. One crystal at 300K, another at 150K.

These two sets of data were collected on different crystals, and despite there being a great similiarity in the length of the c axis, the other parameters suggest that the crystals are of different materials.

The lattice parameters collected at 150K are in excellent agreement to the data of (BEDT-TTF)$_4$AFe$(C_2O_4)_3.C_6H_5CN$. Table 5.2 lists the lattice parameters of the four compounds for direct comparison.

Parameter	KFe (120K)	NH_4Fe (120K)	$(H_2O)Fe$ (120K)	?Cr (150K)
a	10.33(2)Å	10.370(5)Å	10.232(12)Å	10.3Å
b	19.53(3)Å	19.588(12)Å	20.04(3)Å	19.4Å
c	35.94(2)Å	35.790(8)Å	34.97(2)Å	35.86Å
α	90.0°	90.0°	90.0°	90.0°
β	90.0°	90.0°	93.25°	90.0°
γ	90.0°	90.0°	90.0°	90.0°

Table 5.2 The lattice parameters of $(BEDT\text{-}TTF)_4AFe(C_2O_4)_3.C_6H_5CN$ (A = K, NH_4 or H_2O) and of a crystal grown from BEDT-TTF and $K_3Cr(C_2O_4)_3.3H_2O$ in wet benzonitrile.

The lattice parameters of the Chromium complex at 150K are thus in excellent agreement with those obtained from the iron compounds. The greatest similarity is observed with $(BEDT\text{-}TTF)_4KFe(C_2O_4)_3.C_6H_5CN$, but the errors in determining these parameters cannot lead to a definitive conclusion. However, they strongly suggest that the unit cell will have very similar contents and therefore it is assumed that the material has the general formula $(BEDT\text{-}TTF)_4ACr(C_2O_4)_3.C_6H_5CN$. Given that the material was prepared from a solution of $K_3Cr(C_2O_4)_3.3H_2O$ in wet benzonitrile, it is unclear whether A will equal K or H_2O, but the crystallographic data strongly suggests that A is potassium .

5.4.3 Electrical Transport

The needle like morphology of these crystals allowed four probe electrical transport experiment to be performed. The room temperature resistivity was low (~20 Ωcm^{-1}) and

as the material was cooled, this value increased very slightly, indicating semimetallic behaviour (Figure 5.5).

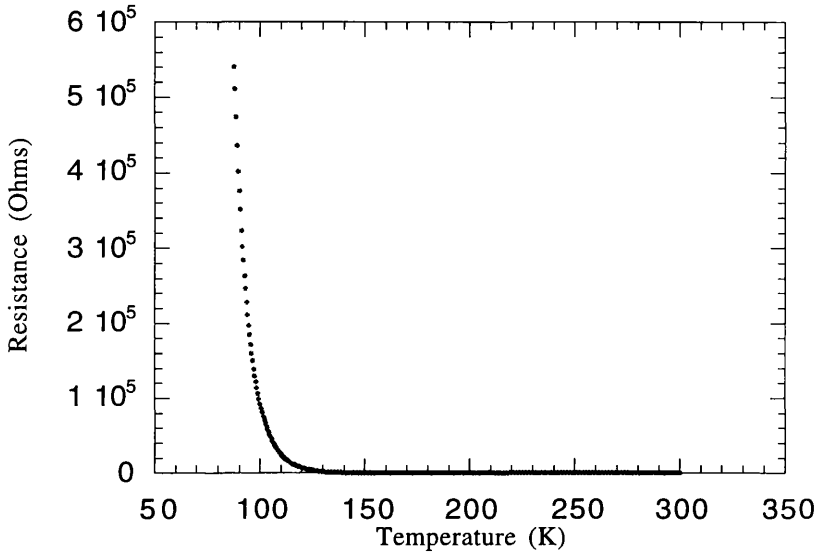

Figure 5.5. The temperature dependent conductivity of a crystal grown from BEDT-TTF and $K_3Cr(C_2O_4)_3.3H_2O$ in wet benzonitrile.

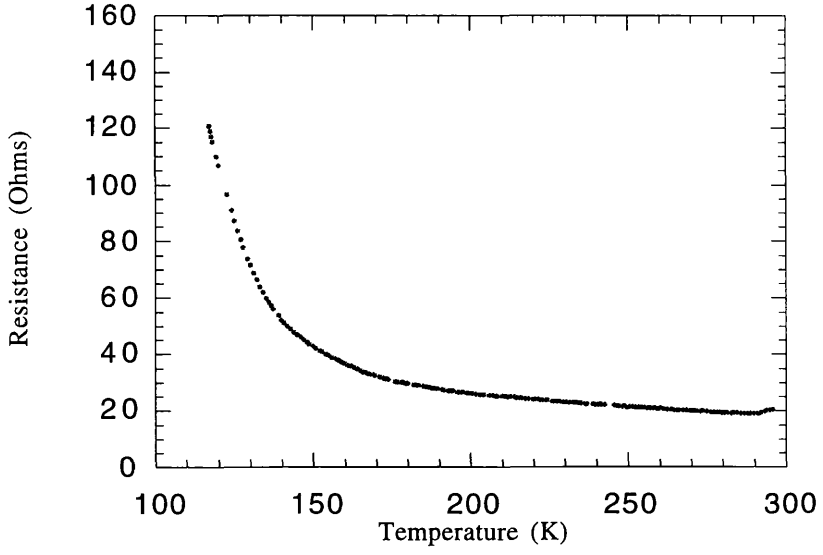

Figure 5.6 The temperature profile of the resistance between 300 to 115K of a crystal grown from BEDT-TTF and $K_3Cr(C_2O_4)_3.3H_2O$ in wet benzonitrile.

However, at 150K, there is a sharp increase in the resistance (Figure 5.7) and a semimetal to insulator phase transition has occured. A least squares fit to the slope of the ln resistance versus 1000/ Temperature curve below 150K yields an activation energy of 0.11eV.

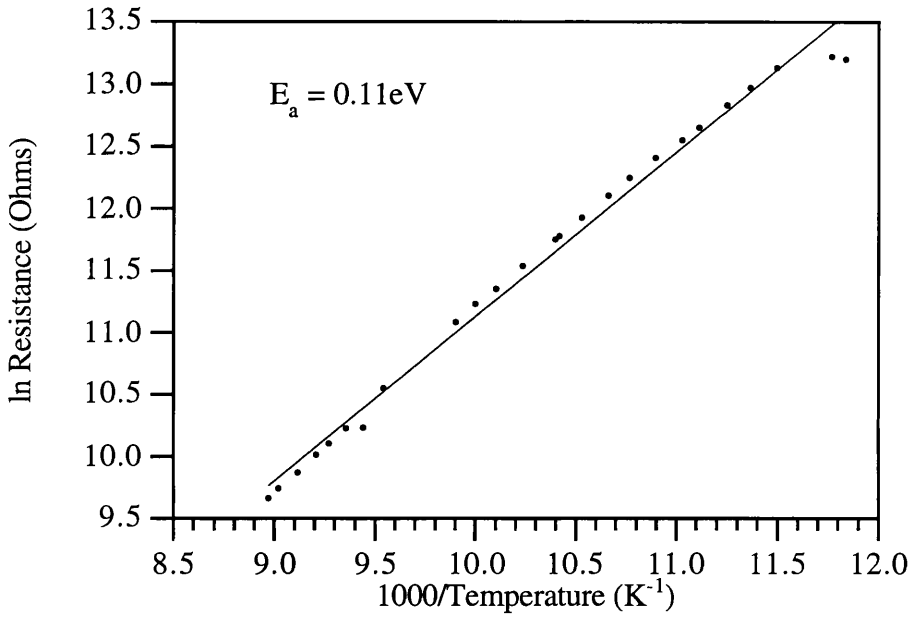

Figure 5.7. Linear fit for the activation energy in crystals grown from BEDT-TTF and $K_3Cr[(C_2O_4)_3]$ in wet benzonitrile.

5.4.4 SQUID Magnetometery

In order to quantitatively analyse the magnetic measurements, it was assumed that this compound had the same stoichiometery as the iron analogue i.e. $(BEDT\text{-}TTF)_4ACr(C_2O_4)_3.C_6H_5CN$. In this section, it has been assumed that A = K. This assumption was originally based upon the crystallographic data given in section 5.4.1 and justification for this has been obtained with fits to the magnetic data

5.4.4.1 Susceptibility

Susceptibility measurements were performed on a polycrystalline sample (12.29mg) of needle like crystals contained within a gelatine capsule. The temperature dependent susceptibility was measured on a SQUID magnetometer at fields of 0.5, 1 and 1.5T. The molar susceptibilities derived from these data sets were in excellent agreement and the data collected at 1T is illustrated in Figure 5.7.

A plot of the inverse of the molar susceptibility versus temperature (Figure 5.8) reveals that there is a transition at ~150K, which is the same temperature as the semimetallic to insulator transition in the conductivity masurements. Both above and below the transition, there is a constant slope which is indicative of paramagnetic behaviour. However, the slopes vary, suggesting different values for C and θ. It should be noted that the fits were performed by the method described in section 2.3.4 and not to a linear fit of the inverse susceptiblity.

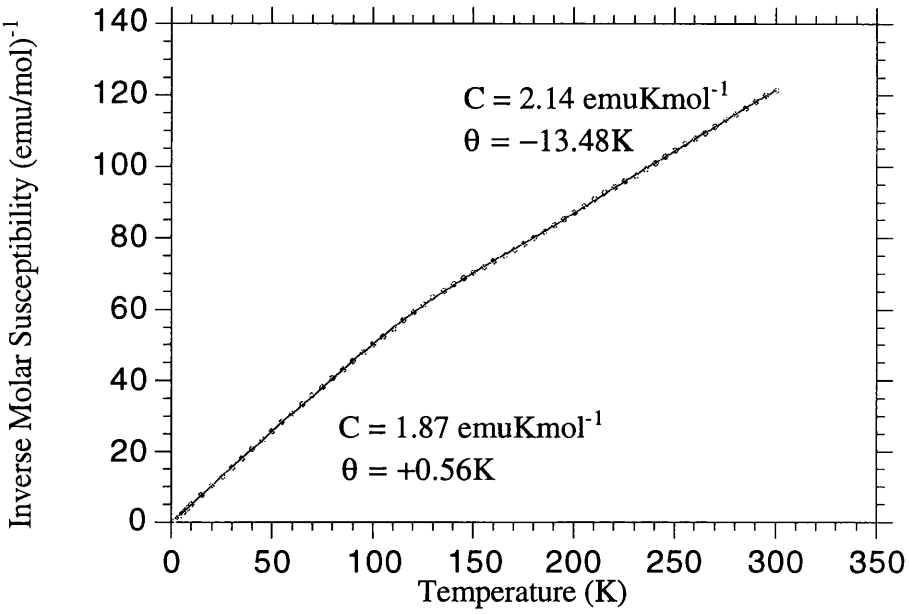

Figure 5.8. The inverse molar susceptibility versus temperature for needle like crystals grown from BEDT-TTF and $K_3Cr(C_2O_4)_3]$ in wet benzonitrile. Data collected at 1T.

Fitting the data between 300 - 160K gives a Curie constant of 2.14emuKmol^{-1} (The calculated value for C in a d^3 system is 1.88emuKmol^{-1}) and a Weiss constant of -13.48K, indicating a relatively strong antiferromagnetic interaction. This suggests that there are more spins contributing to the susceptibility than are available from the inorganic layer. However, when the data are fitted between 140 - 2K, the Curie constant has fallen to 1.87emuKmol^{-1} and the Weiss constant is +0.56K indicating very little magnetic interaction. The higher temperature data suggests that there is a contribution to the paramagnetic susceptibility from BEDT-TTF. Below the transition, the value of the Curie constant is consistent with the expected value for a Cr^{3+} cation. This reduction in the value of the Curie constant is consistent with the loss of 0.13 spins per mole.

In fitting the curve, a temperature independent term was added to eliminate any diamagnetic contributions to the susceptibility. However, if the calculated value for the paramagnetic susceptibility is subtracted from the measured total susceptibility, the susceptibility of the BEDT-TTF electrons can be obtained. This is illustrated in Figure 5.9.

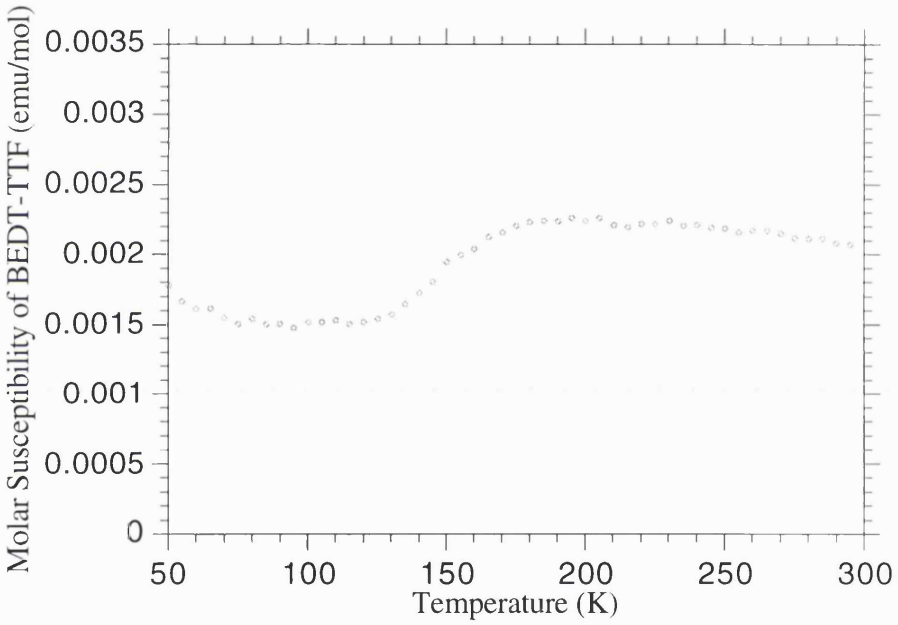

Figure 5.9. The susceptibility of the conduction electrons in crystals grown from BEDT-TTF and $K_3Cr[(C_2O_4)_3]$ in wet benzonitrile.

The susceptibility of the BEDT-TTF electrons between 300 -180K has a reasonably temperature independent value of ~0.002 emu/mol. However at 160K, the temperature of the observed metal - insulator transition in the conductivity experiment, there is a marked decrease in the susceptibility of the conduction electrons to 0.0015emu/mol.

5.4.4.2 Magnetisation

Magnetisation experiments were performed at 2K on the same polycrystalline sample used in the susceptibility experiments. The field was increased from 0 to 1 Tesla in increments of 0.05T and then from 1 to 7 Tesla in 0.5T increments. The experimental data points and the calculated values for a d^3 system are shown in Figure 5.10.

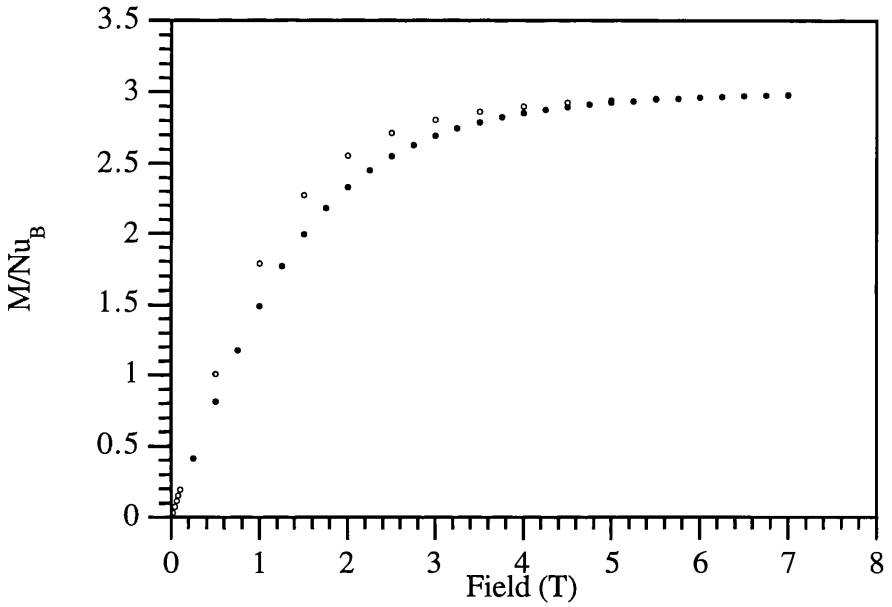

Figure 5.10. The magnetisation of a polycrystalline sample grown from BEDT-TTF and $K_3Cr(C_2O_4)_3$ in wet benzonitrile (empty circles) and the theoretical Brillouin function for S = 3/2 and g = 2.

The experimental and theoretical values are in reasonable agreement with each other. There is a slight divergence at low field, but as saturation is reached, the calculated and observed values are superimposable.

5.5 Crystals grown from BEDT-TTF and $(PPh_4)_3Fe(C_2O_2S_2)_3$

5.5.1 Introduction

An obvious extension to the oxalate family of compounds are their dithiooxalate analogues. The formation of the dithiooxalate derivatives has two effects upon the anion. Firstly, the size is increased and secondly, by introducing Sulfur orbitals into the anion array there is a possibility of increasing the dimensionality of the conduction network. The Sulfur atoms are chelated to the metal ion and the Oxygen atoms are on the outer side of the ligand. In addition to this, the Fe^{3+} has changed from being high spin in the oxalate complex to low spin in the dithiooxalate complex. Hence there is only one unpaired spin per Fe^{3+}.

5.5.2 Electrical Transport

A four probe conductivity experiment was performed on a polycrystalline sample to liquid nitrogen temperatures. The room temperature resistance was $20\Omega cm^{-1}$ and this value decreased with temperature to a minimum of $11\Omega cm^{-1}$ at 160K, indicating metallic behaviour. However, at 150K, this value began to increase, marking the onset of a metal to insulator phase transition (Figure 5.11).

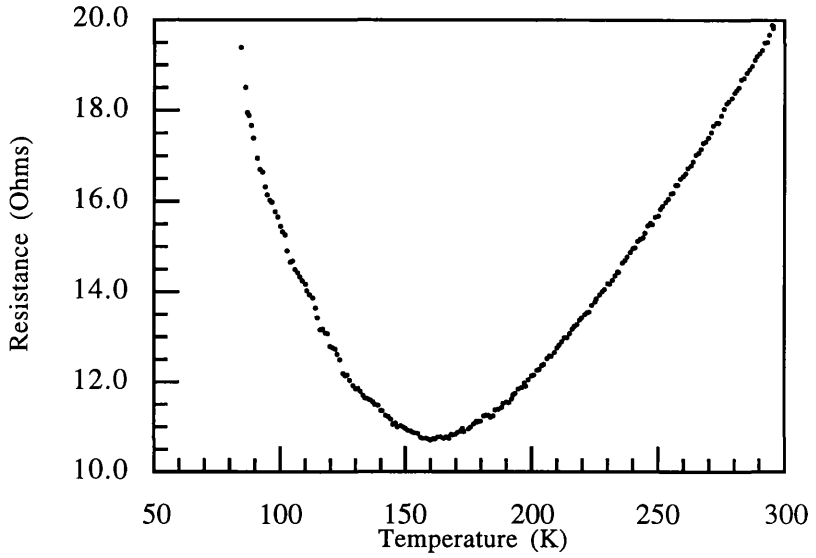

Figure 5.11. The temperature dependent resistance of a polycrystalline sample of material grown from BEDT-TTF and $(PPh_4)_3Fe(C_2O_2S_2)_3$ in wet benzonitrile.

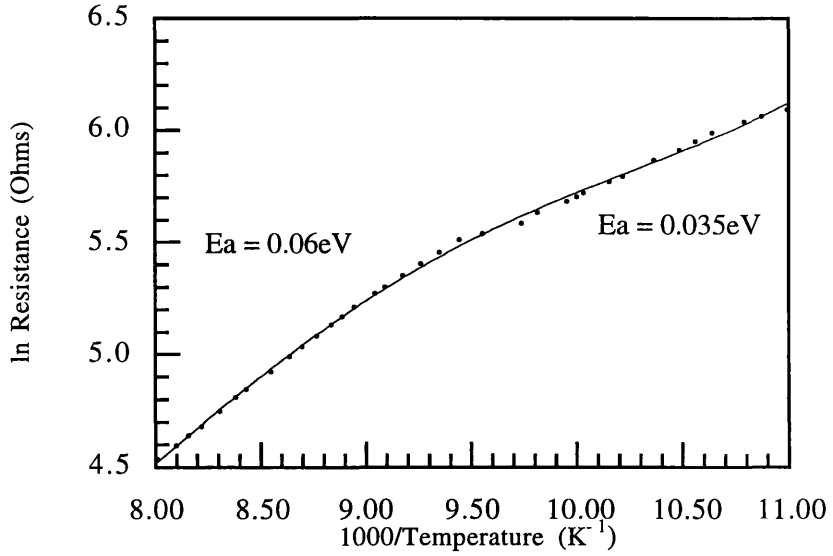

Figure 5.12. The natural log of the resistance versus inverse temperature in the semiconducting region for a polycrystalline sample of material grown from BEDT-TTF and $(PPh_4)_3Fe(C_2O_2S_2)_3$ in wet benzonitrile.

There is a gradual increase in the resistance as the sample is cooled to temperatures below 160K. A plot of the natural log of the resistance versus the inverse temperature yields a curve which constitutes of two straight lines. Least squares fits to these lines gives activation energies of 0.06eV and 0.035eV between 125 - 106K and 102 - 90K respectively.

Attempts to measure the magnetic susceptibility on this material failed to give a reasonable signal. This is a consequence of low sample mass (< 5mg) and only one unpaired spin on the metal ion. The data collected were of too poor a quality to be analysed in any way.

5.6 Crystals grown from BEDT-TTF and $(NH_4)_3Fe(C_2O_4)_3$ in Benzonitrile with 5% Methanol

5.6.1 Introduction

The superconducting phase $(BEDT\text{-}TTF)_4(H_2O)Fe(C_2O_4)_3.C_6H_5CN$ offers the possibilty for changing the structure very slightly in order to monitor the effect on the physical properties. One such possibility for altering the structure is to change the conditions of the solvent. $(BEDT\text{-}TTF)_4(H_2O)Fe(C_2O_4)_3.C_6H_5CN$ was prepared by adding a drop of water to the electrochemical cell. Instead of adding water, the material discussed in this section was prepared by adding 5% dry methanol, thus increasing the size of the counter solvent molecule. The concentration of $(NH_4)_3Fe(C_2O_4)_3$ was kept constant.

5.6.2 X-ray Crystallography

Due to twinning of the crystals, it has not been possible to solve the crystal structure. However lattice parameters have been deduced at 120K and the data obtained are listed in Table 6.3

MeOH	H_2O
a = 10.36Å	a = 10.232Å
b = 11.37Å	b = 20.04Å
c = 36.78Å	c = 34.97Å
α = 91.11°	α = 90.00°
β = 116.5°	β = 93.25°
γ = 91.96°	γ = 90.00°

Table 6.3 Crystallographic lattice parameters of (BEDT-TTF)$_4$(MeOH)Fe(C_2O_4)$_3$.C_6H_5CN) and (BEDT-TTF)$_4$(H_2O)$_{0.5}$Fe(C_2O_4)$_3$.C_6H_5CN).

There is a similarity between the lengths of a and c and the corresponding angles of α and γ between the two salts. However, there is a marked deviation in the length of b and the β angle. The α and γ angles in the MeOH salt are very close to 90° and more accurate data may indeed indicate that they are equal to 90°. If this is the case, the length of b and angle β will be affected correspondingly to give parameters closer to those observed in the H_2O salt.

5.6.3 SQUID magnetometery

Magnetic measurements were performed upon a polycrystalline sample (10.57mg) contained within a gelatine capsule. Except where stated, the material was cooled in a zero field to 2K, at which temperature a field was applied and data were collected as the sample was warmed.

5.6.3.1 Susceptibility

Figure 5.14 shows a plot of the inverse of the molar susceptibility versus temperature. Data points were collected in an applied field of 1T between 2 and 300K, every 3K. The data gives a linear plot which is indicative of paramagnetic behaviour and fits to the Curie Weiss law give C = 4.47 emuKmol^{-1} and θ = - 0.48K. The value of the Curie constant is slightly higher than would be expected solely for high spin Fe^{3+} (C = 4.375emuKmol^{-1}). This deviation could be accounted for by the empirical formula of the material being slightly different to that postulated, thus affecting the molecular weight and oxygen freezing in the cryostat, which will give an additional paramagnetic signal.

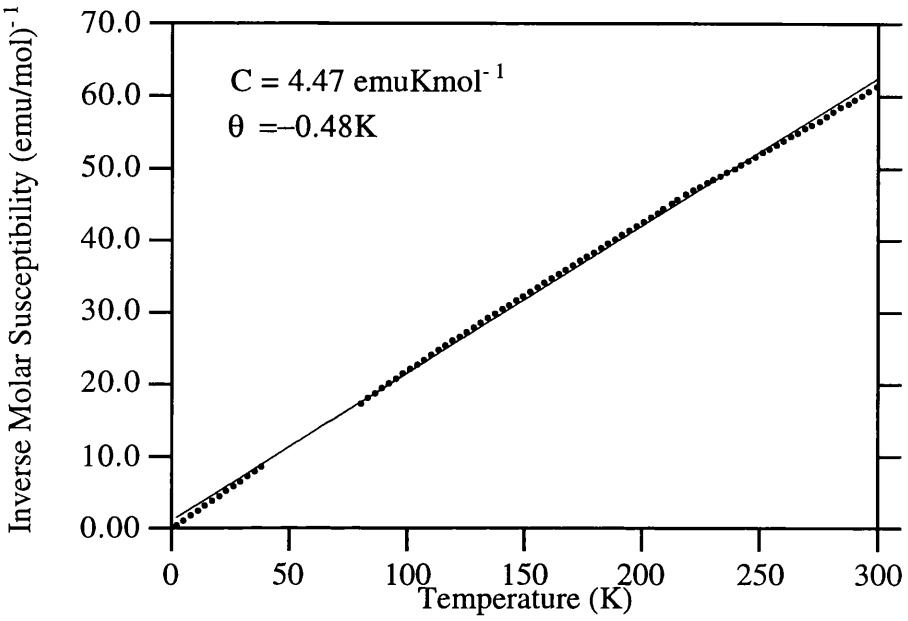

Figure 5.14 The inverse of the molar susceptibility versus temperature for (BEDT-TTF)$_4$(MeOH)Fe(C_2O_4)$_3$.C_6H_5CN) (?). Data collected at 1T.

Figure 5.15 illustrates the effect of an applied magnetic field on the magnetic properties. Data were collected on a polycrystalline sample (2.56mg) contained within a gelatine capsule. Due to the low sample mass, the signal obtained from the SQUID magnetometer was relatively small and thus the errors were higher. However, the data is of sufficient quality to deduce the effect of an applied field on the superconducting properties.

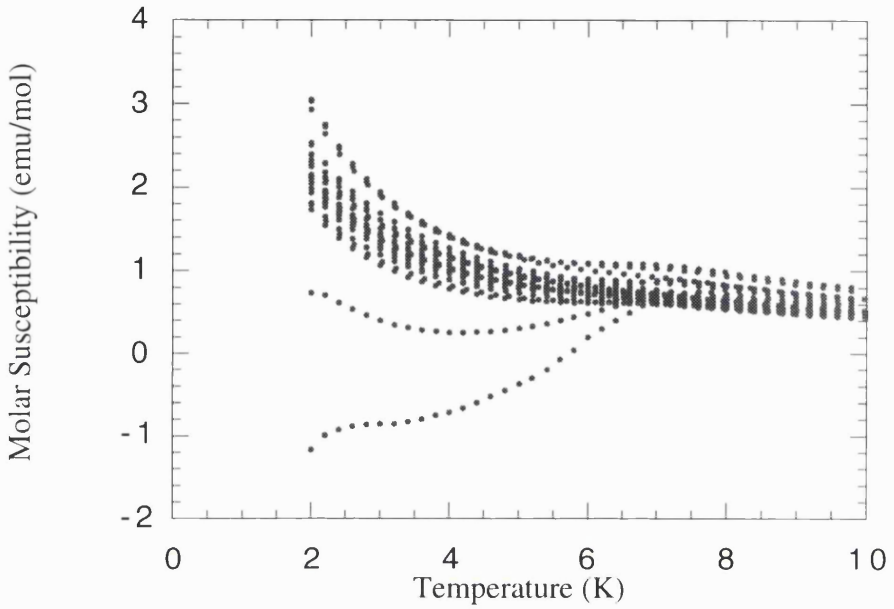

Figure 5.15 The field dependence upon the magnetic susceptibility in (BEDT-TTF)$_4$(MeOH)Fe(C_2O_4)$_3$.C_6H_5CN) (?).

Data were collected by cooling the sample in a zero field to 2K and then applying a measuring field in 1mT intervals between 1 - 25mT. The sample was then warmed to 10K, with data points being collected every 0.2K.

The field dependence of this material is similar to that reported for (BEDT-TTF)$_4$(H_2O)Fe(C_2O_4)$_3$.C_6H_5CN. That is to say in an applied field of 1mT, the material is superconducting, but as the applied field is increased, the diamagnetic signal diminishes and a Curie tail begins to develop, until at 25mT, the signal is dominated by paramagnetic behaviour. However, there is still a significant kink at 7K indicating that the superconductivity has not been destroyed.

5.6.2.2 Magnetisation

Magnetisation measurements were performed on a polycrystalline sample (10.57mg). The sample was cooled in a zero field to 2K and data were collected as field was increased in increments of 0.02T between 0.002 and 0.1T and steps of 0.25T between 0.5T to 7T. The results obtained are illustrated in Figure 5.16.

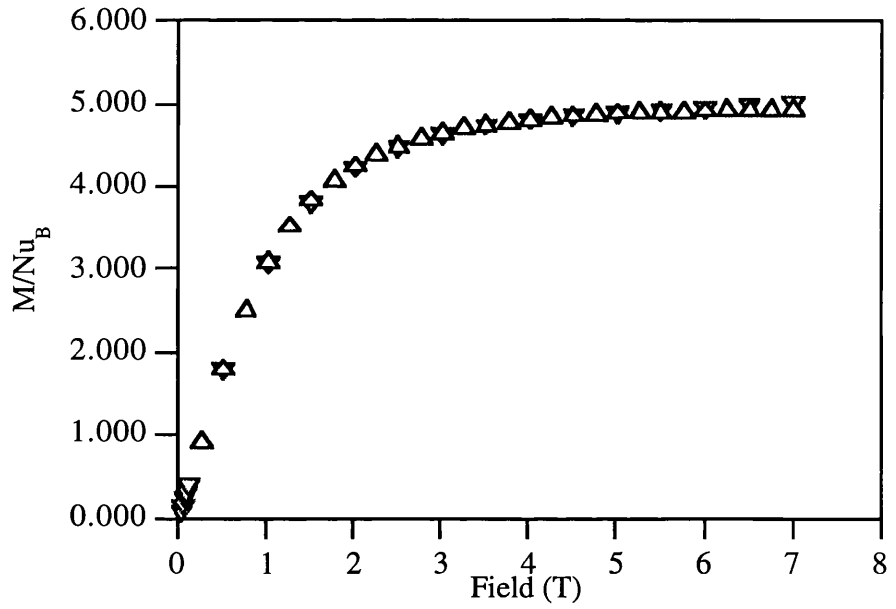

Figure 5.16 The magnetisation of (BEDT-TTF)$_4$(MeOH)Fe(C_2O_4)$_3$.C_6H_5CN) (?) at a 2K isotherm (inverted triangles) and the calculated values for a high spin Fe^{3+} system (triangles).

The experimental data are depicted as inverted triangles and have been converted to a molar value by assuming the emperical formula to be (BEDT-TTF)$_4$(MeOH)Fe(C_2O_4)$_3$.C_6H_5CN. The theoretical magnetisation is illustrated by triangles and as the diagram shows, these two curves are almost superimposable. There is a slight deviation, with the magnitude of the signal from the sample being greater than the expected value, and this deviation increases with field (c.f. (BEDT-

TTF)$_4$(H_2O)Fe(C_2O_4)$_3$.C_6H_5CN). This effect can be accounted for by the Pauli paramagnetism of the conduction electrons of BEDT-TTF.

5.6.3 The Meissner Effect

The Meissner Effect was detected by cooling the sample in a zero field to 2K and applying a field of 0.05mT. Data were collected every 0.3K between 2 - 12K. The sample was then cooled in an applied field of 0.05mT to 2K and data were again collected every 0.3K between 2 - 12K. The results obtained are illustrated in Figure 5.17.

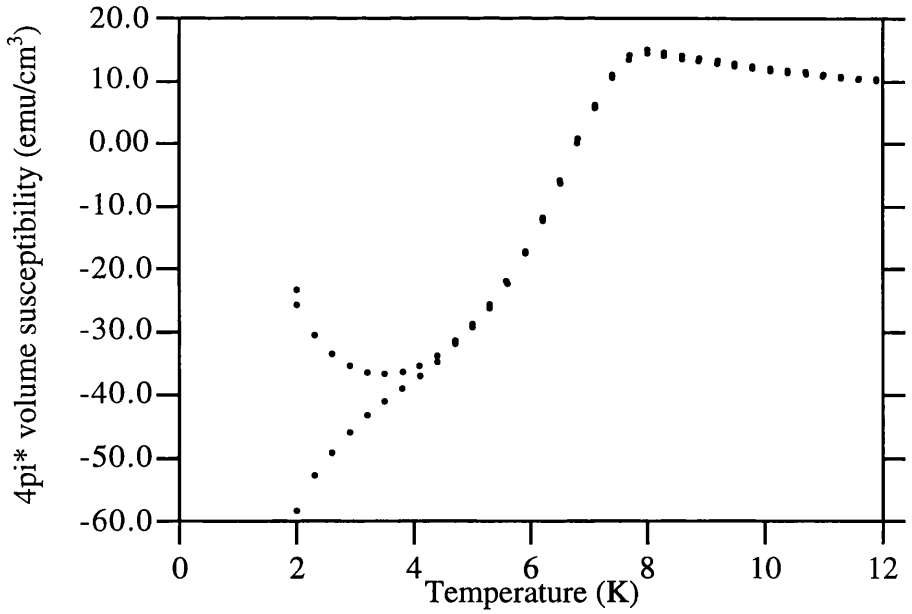

Figure 5.17 The Meissner Effect in (BEDT-TTF)$_4$(MeOH)Fe(C_2O_4)$_3$.C_6H_5CN) (?).

There is a marked deviation between the zero field cooled and the field cooled data sets. Both sets show a broad transition to the superconducting state and the signal becomes more diamagnetic as temperature is reduced in the zero field cooled data set. However,

when the sample is cooled in an applied field, the signal becomes less diamagnetic as temperature is lowered beneath 3.2K. The transition temperature to the superconducting state is very similar to that observed for the water salt (7.7K ± 0.2K). The degree of the diamagnetic shielding is also less than that observed in the H_2O salt (~60% opposed to ~75%), indicating the formation of a different phase. However, with the value of T_c being very similar, it is suggested that a mixed phase mat have formed (e.g. (BEDT-TTF)$_4$(MeOH)$_{0.5}$(H_2O)$_{0.5}$Fe(C_2O_4)$_3$.C_6H_5CN) which would also account for the broadening of the signal to the superconducting state.

5.7 Squarates

5.7.1 Crystals grown from BEDT-TTF and 1,3-[N(C_4H_9)$_4$]$_2$$C_4O_2$(C(CN)$_2$)$_2$ in Tetrahydrofuran (THF).

5.7.1.1 Introduction

Attempts to prepare a purely organic superconductor led to the attempted synthesis of charge transfer salts of BEDT-TTF with squarate dianions. This section will report the electrical properties of one material obtained which was prepared electrochemically prepared from a solution of 1,3- [N(C_4H_9)$_4$]$_2$$C_4O_2$(C(CN)$_2$)$_2$ and BEDT-TTF in THF.

5.7.2 Electrical Transport

The experiment yielded crystals with a plate like morphology which were of a sufficient size to perform a four probe conductivity measurement upon. Four gold wires were attached using Platinum paint and the resistance was measured as a function of

temperature between 300 and 150K. Data were collected every 1K and the results obtained are depicted in Figure 5.18.

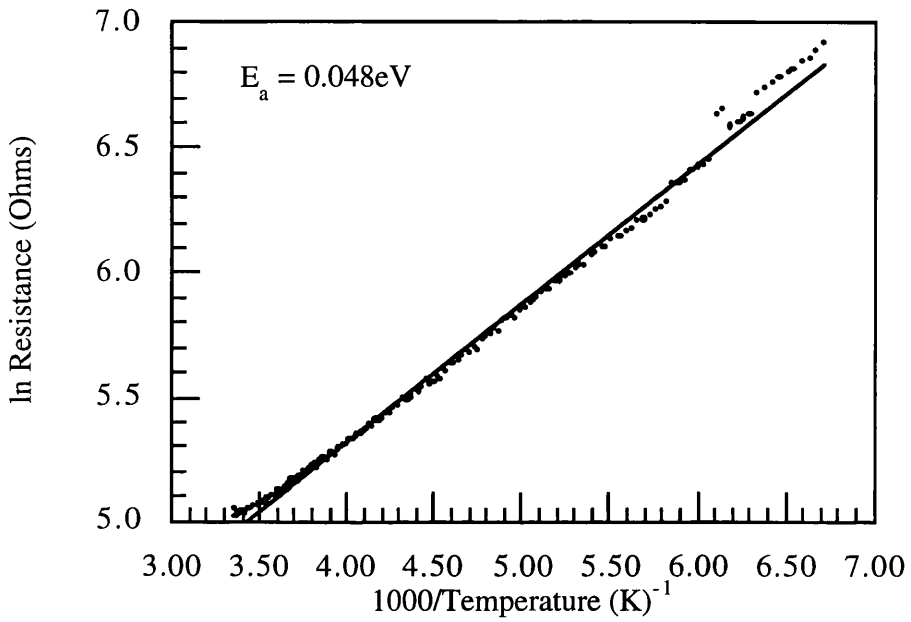

Figure 5.18 The ln Resistance versus inverse temperature for a crystal grown from 1,3-$[N(C_4H_9)_4]_2C_4O_2(C(CN)_2)_2$ in THF.

The resistance increases as temperature is reduced indicating semi conducting behaviour. Least squares fit to the data in Figure 5.18 yields an activation energy of 0.048eV.

Chapter 6

Conclusions and Future Work.

6.1 Conclusions and Future Work.

This research project has predominately been concerned with the synthesis and characterisation of charge transfer salts of BEDT-TTF with metal tris oxalato anions. Three materials, $(BEDT\text{-}TTF)_4AFe(C_2O_4)_3.C_6H_5CN$ (A = K, NH_4 or H_2O) have been prepared and thoroughly characterised by a variety of physical techniques.

The crystal structures of these materials show great similarity within the anionic layer. A honeycomb type structure has formed with A being co-ordinated to the outer oxygen atoms of the oxalate ligand. A benzonitrile molecule resides within the cavity of the honeycomb, which has two fold disorder in the case where A = K or NH_4, but is ordered when A = H_2O.

The subtle differences in the inorganic layer have a great effect on the packing of the organic layer. When A = K or NH_4, a novel packing arrangement of the BEDT-TTF moieties is observed. Orthogonally oriented face to face dimers with a monopositive charge are surrounded by six neutral BEDT-TTF molecules. The packing arrangement resembles that observed within the inorganic layer. However, when A = H_2O, the BEDT-TTF layer packs in the β" phase. That is to say the BEDT-TTF molecules pack flatly with respect to each other, but rather than the stacks being eclipsed, the inner organo sulfur ring of one BEDT-TTF molecule resides above the central carbon carbon double bond of another. This has a huge effect upon the physical properties. When A = K or NH_4, semiconducting behaviour is observed with an activation energy of ~0.14eV. The magnetisation is dominated by the high spin Fe^{3+}. However, when A = H_2O, the material is a superconductor with a T_c of 8.5K. The susceptibility is dominated by the iron tris oxalate complex at high fields, although a signal attributable to the conduction electrons of the organic layer is observed. At low fields though (< 3mT), the susceptibility is strongly

diamagnetic as a consequence of the superconductivity. This is the first time that superconductivity has been observed in a molecular compound which contains localised moments and indeed in any compound where the magnetism comes from 3d electrons.

The rest of the project has been concerned with synthesising related compounds to (BEDT-TTF)$_4$AFe(C_2O_4)$_3$.C_6H_5CN. This research has taken three directions: Firstly, the metal centre has been varied in order to change the number of localised spins in the anionic layer; secondly A has been changed in order to increase the unit cell volume and thirdly the oxalate ligand has been replaced with the dithiooxalate ligand. These efforts have yielded results which offer considerable promise. Where A = MeOH, a superconducting salt has been prepared with a T_c of 7.7K. However, it has not been possible to structurally characterise this material during the current research programme. Therefore, it is suggested that this should form part of a future project. as should the synthesis and characterisation of (BEDT-TTF)$_4$ACr(C_2O_4)$_3$.C_6H_5CN salts. Isomorphous materials to (BEDT-TTF)$_4$AFe(C_2O_4)$_3$.C_6H_5CN have been prepared in the final weeks of this research project and these compounds should be characterised and compared to their iron analogues. In addition to this, metal tris oxalato anions should be used which do not possess any localised moments (e.g. Co(C_2O_4)$_3^{3-}$ and Al(C_2O_4)$_3^{3-}$). This would enable the effect of localised moments on the electrical properties to be examined. A further synthetic challenge would be to form BEDT-TTF charge transfer salts with the following series of compounds: [M(C_2O_4)$_2$($C_2O_2S_2$)]$^{3-}$; [M(C_2O_4)($C_2O_2S_2$)$_2$]$^{3-}$ and [M($C_2O_2S_2$)$_3$]$^{3-}$ which would allow the effect of ligand substitution to be systematically monitored. Another permeatation would be to replace the monpositive A cation with a dication such as Fe^{2+} in order to prepare compounds with interesting magnetic properties.

Appendix 1

The atomic coordinates , bond lengths and bond angles of $(BEDT\text{-}TTF)_4AFe(C_2O_4)_3.C_6H_5CN$.

(A = K, NH_4 or H_2O)

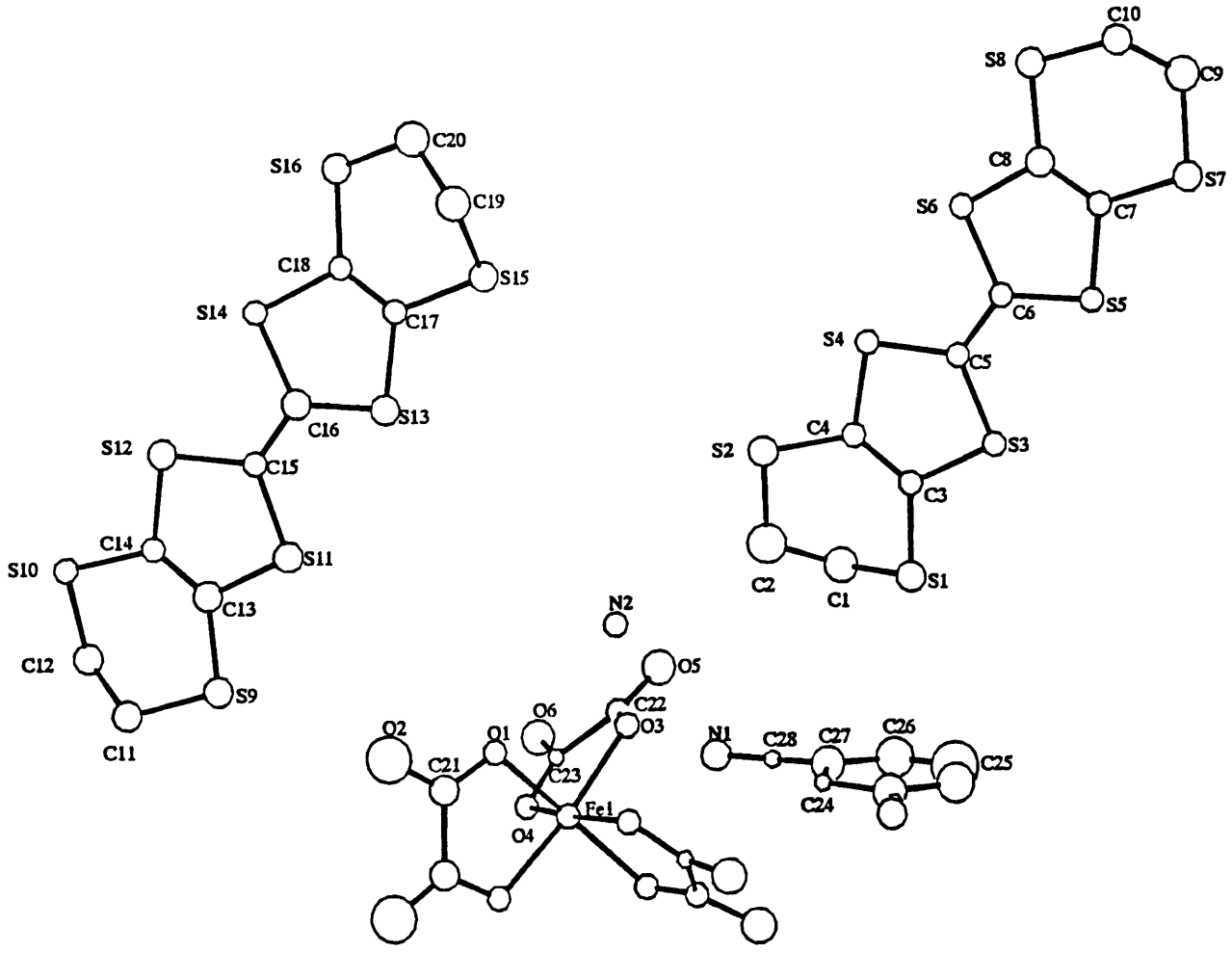

Figure A.1 The labelling scheme of the asymmetric unit in (BEDT-TTF)$_4$AFe(C_2O_4)$_3$.C_6H_5CN

(A = K or NH_4)

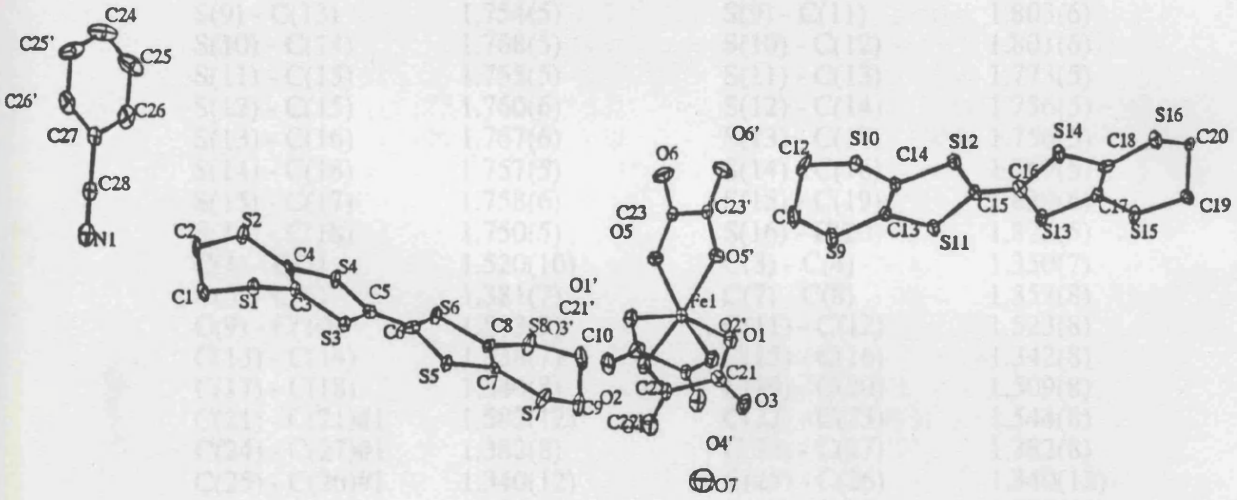

Figure A.2 The labelling scheme of the asymmetric unit in $(BEDT\text{-}TTF)_4(H_2O)Fe(C_2O_4)_3.C_6H_5CN$.

Bond lengths (Å) for $(BEDT\text{-}TTF)_4KFe(C_2O_4)_3.C_6H_5CN$.

Bond	Bond Length (Å)	Bond	Bond Length (Å)
Fe(1) - O(1)	1.998(4)	Fe(1) - O(1)#1	1.998(4)
Fe(1) - O(4)#1	2.017(4)	Fe(1) - O(4)	2.017(4)
Fe(1) - O(3)	2.019(4)	Fe(1) - O(3)#1	2.019(4)
O(1) - C(21)	1.279(8)	O(2) - C(21)	1.219(8)
O(3) - C(22)	1.293(7)	O(4) - C(23)	1.292(7)
O(5) - C(22)	1.210(7)	O(6) - C(23)	1.230(7)
S(1) - C(3)	1.755(5)	S(1) - C(1)	1.816(6)
S(2) - C(4)	1.747(6)	S(2) - C(2)	1.807(7)
S(3) - C(5)	1.730(5)	S(3) - C(3)	1.754(5)
S(4) - C(5)	1.735(5)	S(4) - C(4)	1.745(5)
S(5) - C(6)	1.731(6)	S(5) - C(7)	1.753(5)
S(6) - C(8)	1.741(5)	S(6) - C(6)	1.727(5)
S(7) - C(7)	1.746(6)	S(7) - C(9)	1.811(6)
S(8) - C(8)	1.746(5)	S(8) - C(10)	1.806(6)
S(9) - C(13)	1.754(5)	S(9) - C(11)	1.803(6)
S(10) - C(14)	1.768(5)	S(10) - C(12)	1.801(6)
S(11) - C(15)	1.755(5)	S(11) - C(13)	1.773(5)
S(12) - C(15)	1.760(6)	S(12) - C(14)	1.756(5)
S(13) - C(16)	1.767(6)	S(13) - C(17)	1.756(5)
S(14) - C(18)	1.757(5)	S(14) - C(16)	1.769(5)
S(15) - C(17)	1.758(6)	S(15) - C(19)	1.839(6)
S(16) - C(18)	1.750(5)	S(16) - C(20)	1.828(5)
C(1) - C(2)	1.520(10)	C(3) - C(4)	1.350(7)
C(5) - C(6)	1.381(7)	C(7) - C(8)	1.357(8)
C(9) - C(10)	1.513(9)	C(11) - C(12)	1.523(8)
C(13) - C(14)	1.338(7)	C(15) - C(16)	1.342(8)
C(17) - C(18)	1.340(8)	C(19) - C(20)	1.509(8)
C(21) - C(21)#1	1.583(12)	C(22) - C(23)	1.544(8)
C(24) - C(27)#1	1.382(8)	C(24) - C(27)	1.382(8)
C(25) - C(26)#1	1.340(12)	C(25) - C(26)	1.340(12)
C(26) - C(27)	1.424(12)	C(27) - C(28)	1.259(13)
C(28) - N(1)	1.138(14)		

Bond angles for $(BEDT\text{-}TTF)_4KFe(C_2O_4)_3.C_6H_5CN$.

Bond	Angle (°)	Bond	Angle (°)
O(1) - Fe(1) - O(1)#1	81.2(2)	O(1) - Fe(1) - O(4)#1	91.0(2)
O(1)#1 - Fe(1) - O(4)#1	96.4(2)	O(1) - Fe(1) - O(4)	96.4(2)
O(1)#1 - Fe(1) - O(4)	91.0(2)	O(4)#1 - Fe(1) - O(4)	170.3(2)
O(1) - Fe(1) - O(3)	94.8(2)	O(1)#1 - Fe(1) - O(3)	170.9(2)
O(4)#1 - Fe(1) - O(3)	91.8(2)	O(4) - Fe(1) - O(3)	81.3(2)
O(1) - Fe(1) - O(3)#1	170.9(2)	O(1)#1 - Fe(1) - O(3)#1	94.8(2)
O(4)#1 - Fe(1) - O(3)#1	81.3(2)	O(4) - Fe(1) - O(3)#1	91.8(2)
O(3) - Fe(1) - O(3)#1	90.3(2)	C(21) - O(1) - Fe(1)	116.0(4)
C(22) - O(3) - Fe(1)	114.5(3)	C(23) - O(4) - Fe(1)	114.1(3)
O(1) - Fe(1) - O(3)	94.8(2)	O(1)#1 - Fe(1) - O(3)	170.9(2)
C(23) - O(6) - K(1)	119.9(4)	C(22) - O(5) - K(1)	122.4(4)
C(3) - S(1) - C(1)	97.7(3)	C(4) - S(2) - C(2)	103.8(3)
C(5) - S(3) - C(3)	95.3(2)	C(6) - C(5) - S(3)	123.4(4)
C(5) - C(6) - S(5)	124.3(4)	C(8) - S(6) - C(6)	95.8(3)
C(7) - S(7) - C(9)	100.2(3)	C(8) - S(8) - C(10)	101.2(3)
C(13) - S(9) - C(11)	100.9(3)	C(14) - S(10) - C(12)	99.8(3)
C(15) - S(11) - C(13)	94.7(3)	C(15) - S(12) - C(14)	94.4(2)
C(16) - S(13) - C(17)	93.9(3)	C(18) - S(14) - C(16)	94.3(3)
C(17) - S(15) - C(19)	97.0(3)	C(18) - S(16) - C(20)	105.4(3)
C(2) - C(1) - S(1)	112.9(4)	C(1) - C(2) - S(2)	114.3(4)
C(4) - C(3) - S(1)	124.8(4)	C(4) - C(3) - S(3)	116.6(4)
S(1) - C(3) - S(3)	118.5(3)	C(3) - C(4) - S(2)	130.0(4)
C(3) - C(4) - S(4)	117.2(4)	S(2) - C(4) - S(4)	112.8(3)
C(6) - C(5) - S(4)	120.8(4)	C(6) - C(5) - S(4)	120.8(4)
S(4) - C(5) - S(3)	115.6(3)	C(5) - C(6) - S(5)	115.4(3)
C(5) - C(6) - S(6)	120.3(4)	S(5) - C(6) - S(6)	115.2(9)
C(8) - C(7) - S(5)	116.5(4)	C(8) - C(7) - S(7)	128.7(4)
S(5) - C(7) - S(7)	114.9(3)	C(7) - C(8) - S(6)	116.8(4)
C(7) - C(8) - S(8)	128.7(4)	S(6) - C(8) - S(8)	114.5(3)
C(10) - C(9) - S(7)	113.3(4)	C(9) - C(10) - S(8)	114.2(4)
C(12) - C(11) - S(9)	114.2(4)	C(11) - C(12) - S(10)	113.4(3)
C(14) - C(13) - S(9)	129.6(4)	C(14) - C(13) - S(11)	116.5(4)
S(9) - C(13) - S(11)	114.0(3)	C(13) - C(14) - S(10)	127.9(4)
C(13) - C(14) - S(12)	118.4(4)	S(10) - C(14) - S(12)	113.6(3)
C(16) - C(15) - S(11)	124.1(4)	C(16) - C(15) - S(12)	120.9(4)
S(11) - C(15) - S(12)	114.9(3)	C(15) - C(16) - S(13)	124.1(4)
C(15) - C(16) - S(14)	121.3(4)	S(13) - C(16) - S(14)	114.5(3)
C(18) - C(17) - S(13)	118.2(4)	C(18) - C(17) - S(15)	123.1(4)
S(13) - C(17) - S(15)	118.3(3)	C(17) - C(18) - S(16)	126.9(4)
C(17) - C(18) - S(14)	117.2(4)	S(16) - C(18) - S(14)	115.8(3)
C(20) - C(19) - S(15)	113.6(4)	C(19) - C(20) - S(16)	116.2(4)
O(1) - C(21) - O(2)	126.5(6)	O(1) - C(21) - C(21)#1	113.4(3)
O(2) - C(21) - C(21)#1	120.0(4)	O(3) - C(22) - O(5)	126.0(5)
O(3) - C(22) - C(23)	114.1(5)	O(5) - C(22) - C(23)	119.9(5)
O(6) - C(23) - O(4)	124.9(5)	O(4) - C(23) - C(22)	115.4(5)
O(4) - C(23) - C(22)	119.7(5)	C(27)#1 - C(24) - C(27)	119.5(9)
C(26)#1 - C(25) - C(26)	119.5(14)	C(25) - C(26) - C(27)	121.7(10)
C(28) - C(27) - C(26)	115.6(9)	C(28) - C(27) - C(24)	125.5(9)
C(26) - C(27) - C(24)	118.8(8)	N(1) - C(28) - C(27)	178.5(12)

Symmetry transformations used to generate equivalent atoms:

#1 - x, y, -z + 1/2 #2 x-1/2, y+1/2, -z+1/2 # -x+1, y, -z+1/2
#4 x+1/2, y-1/2, -z+1/2 #5 -x+1/2, y-1/2, z

Atomic coordinates ($*10^4$) and equivalent isotropic displacement parameters ($Å^2 * 10^3$) for $(BEDT\text{-}TTF)_4KFe(C_2O_4)_3.C_6H_5CN$. U (eq) is defined as one third of the trace of the orthogonaliised Uij tensor.

Atom	x	y	z	U(eq)
Fe(1)	0	3045(1)	2500	23(1)
O(1)	574(4)	3822(2)	2822(1)	27(1)
O(2)	627(6)	4964(3)	2846(1)	58(2)
O(3)	866(3)	2316(2)	2811(1)	25(1)
O(4)	1664(4)	2958(2)	2210(1)	27(1)
O(5)	2560(5)	1609(3)	2794(1)	46(1)
O(6)	3522(4)	2370(2)	2209(1)	37(1)
S(1)	303(1)	-179(1)	36421)	22(1)
S(2)	2653(1)	918(1)	3995(1)	29(1)
S(3)	220(1)	-730(1)	4425(1)	17(1)
S(4)	2261(1)	191(1)	4692(1)	21(1)
S(5)	143(1)	-1432(1)	5263(1)	19(1)
S(6)	2184(1)	-480(1)	5486(1)	19(1)
S(7)	-54(1)	-2127(1)	5990(1)	24(1)
S(8)	2502(1)	-1013(1)	6243(1)	22(1)
S(9)	-117(1)	7247(1)	3581(1)	22(1)
S(10)	2522(1)	8293(1)	3853(1)	21(1)
S(11)	-183(1)	6858(1)	4376(1)	21(1)
S(12)	2126(1)	7667(1)	4591(1)	22(1)
S(13)	-108(1)	6125(1)	5208(1)	22(1)
S(14)	2225(1)	6957(1)	5283(1)	21(1)
S(15)	185(1)	5265(1)	5901(1)	23(1)
S(16)	2834(1)	6201(1)	6078(1)	25(1)
C(1)	1807(6)	67(3)	3417(2)	34(2)
C(2)	2223(6)	793(4)	3512(2)	39(2)
C(3)	852(5)	-143(3)	4104(1)	18(1)
C(4)	1797(5)	276(3)	4228(2)	19(1)
C(5)	1180(4)	-463(3)	4792(1)	17(1)
C(6)	1155(5)	-764(3)	5140(2)	19(1)
C(7)	698(5)	-1494(3)	5723(1)	21(1)
C(8)	1662(5)	-1059(3)	5822(1)	19(1)
C(9)	1123(5)	-2223(3)	6359(2)	30(1)
C(10)	1510(5)	-1551(3)	6536(2)	28(1)
C(11)	647(5)	7938(3)	3332(2)	29(1)
C(12)	2102(5)	7993(3)	3395(2)	28(1)
C(13)	590(5)	7339(3)	4022(1)	18(1)
C(14)	1615(5)	7712(3)	4126(1)	18(1)
C(15)	999(5)	7030(3)	4714(1)	20(1)
C(16)	1038(5)	6731(3)	5050(2)	22(1)
C(17)	794(5)	5906(3)	5605(1)	20(1)
C(18)	1838(5)	6284(3)	5687(1)	17(1)
C(19)	396(5)	5736(3)	6340(2)	28(1)

Atom	x	y	z	U(eq)
C(20)	1794(5)	5853(3)	6444(2)	27(1)
C(21)	348(6)	4423(4)	2696(2)	30(2)
C(22)	1948(5)	2092(3)	2677(2)	24(1)
C(23)	2446(5)	2498(3)	2338(2)	24(1)
C(24)	0	400(4)	2500	29(2)
C(25)	0	-1031(7)	2500	69(4)
C(26)	1017(1)	-686(5)	2365(2)	70(3)
C(27)	1047(7)	43(4)	2359(2)	45(2)
C(28)	2032(10)	307(5)	2212(3)	16(2)
N(1)	2911(10)	560(6)	2079(3)	35(3)
K(1)	5000	1241(1)	2500	57(1)
H(1A)	2484(6)	-248(3)	3492(2)	41
H(1B)	1703(6)	29(3)	3150(2)	41
H(2A)	1524(6)	1104(4)	3450(2)	47
H(2B)	2961(6)	913(4)	3359(2)	47
H(9A)	765(5)	-2521(3)	6550(2)	35
H(9B)	1890(5)	-2444(3)	6260(2)	35
H(10A)	1979(5)	-1646(3)	6764(2)	34
H(10B)	732(5)	-1301(3)	6603(2)	34
H(11A)	489(5)	7877(3)	3068(2)	34
H(11B)	246(5)	8366(3)	3406(2)	34
H(12A)	2465(5)	8303(3)	3212(2)	34
H(12B)	2490(5)	7546(3)	3357(2)	34
H(19A)	-34(5)	6176(3)	6319(2)	33
H(19B)	-23(5)	5482(3)	6538(2)	33
H(20A)	2157(5)	5420(3)	6525(2)	32
H(20B)	1819(5)	6162(3)	6654(2)	32
H(24)	0	876(4)	2500	35
H(25)	0	-1508(7)	2500	82
H(26)	1722(10)	-928(5)	2272(2)	84

Bond lengths (Å) for (BEDT-TTF)$_4$NH$_4$Fe(C_2O_4)$_3$.C_6H_5CN.

Bond	Bond Length (Å)	Bond	Bond Length (Å)
Fe(1) - O(1)	1.997(10)	Fe(1) - O(1)#1	1.997(10)
Fe(1) - O(4)#1	1.999(11)	Fe(1) - O(4)	1.999(11)
Fe(1) - O(3)	2.012(10)	Fe(1) - O(3)#1	2.012(11)
O(1) - C(21)	1.23(2)	O(2) - C(21)	1.27(2)
O(3) - C(22)	1.25(2)	O(4) - C(23)	1.25(2)
O(5) - C(22)	1.26(2)	O(6) - C(23)	1.24(2)
S(1) - C(3)	1.74(2)	S(1) - C(1)	1.84(2)
S(2) - C(4)	1.74(2)	S(2) - C(2)	1.81(2)
S(3) - C(5)	1.74(2)	S(3) - C(3)	1.79(2)
S(4) - C(5)	1.72(2)	S(4) - C(4)	1.74(2)
S(5) - C(6)	1.72(2)	S(5) - C(7)	1.76(2)
S(6) - C(8)	1.73(2)	S(6) - C(6)	1.74(2)
S(7) - C(7)	1.76(2)	S97) - C(9)	1.82(2)
S(8) - C(8)	1.77(2)	S(8) - C(10)	1.83(2)
S(9) - C(13)	1.75(2)	S(9) - C(11)	1.78(2)
S(10) - C(14)	1.77(2)	S(10) - C(12)	1.83(2)
S(11) - C(15)	1.75(2)	S(11) - C(13)	1.80(2)
S(12) - C(15)	1.77(2)	S(12) - C(14)	1.77(2)
S(13) - C(16)	1.74(2)	S(13) - C(17)	1.76(2)
S(14) - C(18)	1.76(2)	S(14) - C(16)	1.78(2)
S(15) - C(17)	1.78(2)	S(15) - C(19)	1.82(2)
S(16) - C(18)	1.75(2)	S(16) - C(20)	1.85(2)
C(1) - C(2)	1.48(3)	C(3) - C(4)	1.34(2)
C(5) - C(6)	1.40(2)	C(7) - C(8)	1.33(2)
C(9) - C(10)	1.52(3)	C(11) - C(12)	1.52(2)
C(13) - C(14)	1.32(3)	C(15) - C(16)	1.35(2)
C(17) - C(18)	1.29(2)	C(19) - C(20)	1.55(3)
C(21) - C(21)#1	1.52(4)	C(22) - C(23)	1.53(2)
C(24) - C(27)#1	1.42(2)	C(24) - C(27)	1.42(2)
C(25) - C(26)#1	1.32(3)	C(25) - C(26)	1.32(3)
C(26) - C(27)	1.39(3)	C(27) - C(28)	1.26(3)
C(28) - N(1)	1.17(4)		

Bond angles for $(BEDT\text{-}TTF)_4NH_4Fe(C_2O_4)_3.C_6H_5CN$.

Bond	Angle (°)	Bond	Angle (°)
O(1) - Fe(1) - O(1)#1	81.1(6)	O(1) - Fe(1) - O(4)#1	91.3(4)
O(1)#1 - Fe(1) - O(4)#1	96.7(4)	O(1) - Fe(1) - O(4)	96.7(4)
O(1)#1 - Fe(1) - O(4)	91.3(4)	O(4)#1 - Fe(1) - O(4)	169.4(6)
O(1) - Fe(1) - O(3)	94.7(4)	O(1)#1 - Fe(1) - O(3)	170.8(4)
O(4)#1 - Fe(1) - O(3)	91.6(4)	O(4) - Fe(1) - O(3)	80.9(4)
O(1) - Fe(1) - O(4)#1	170.8(4)	O(1)#1 - Fe(1) - O(3)#1	94.7(4)
O(4)#1 - Fe(1) - O(3)#1	80.9(4)	O(4) - Fe(1) - O(3)#1	91.6(4)
O(3) - Fe(1) - O(3)#1	90.6(6)	C(21) - O(1) - Fe(1)	113.4(11)
C(22) - O(3) - Fe(1)	113.5(10)	C(23) - O(4) - Fe(1)	114.3(10)
C(3) - S(1) - C(1)	96.6(8)	C(4) - S(2) - C(2)	104.5(9)
C(5) - S(3) - C(3)	93.9(7)	C(5) - S(4) - C(4)	94.6(8)
C(6) - S(5) - C(7)	95.1(7)	C(8) - S(6) - C(6)	95.1(8)
C(7) - S(7) - C(9)	101.1(8)	C(8) - S(8) - C(10)	101.3(8)
C(13) - S(9) - C(11)	100.4(8)	C(14) - S(10) - C(12)	99.3(8)
C(15) - S(11) - C(13)	94.5(8)	C(15) - S(12) - C(14)	94.2(8)
C(16) - S(13) - C(17)	92.4(8)	C(18) - S(14) - C(16)	92.8(8)
C(17) - S(15) - C(19)	96.8(8)	C(18) - S(16) - C(20)	105.1(9)
C(2) - C(1) - S(1)	113.6(14)	C(1) - C(2) - S(2)	114(2)
C(4) - C(3) - S(1)	126.4(13)	C(4) - C(3) - S(3)	115.6(12)
S(1) - C(3) - S(3)	117.8(9)	C(3) - C(4) - S(2)	128.8(13)
C(3) - C(4) - S(4)	118.5(13)	S(2) - C(4) - S(4)	112.7(9)
C(6) - C(5) - S(4)	121.6(12)	C(6) - C(5) - S(3)	120.9(12)
S(4) - C(5) - S(3)	117.3(9)	C(5) - C(6) - S(5)	126.2(12)
C(5) - C(6) - S(6)	118.5(12)	S(5) - C(6) - S(6)	115.2(9)
C(8) - C(7) - S(5)	116.9(12)	C(8) - C(7) - S(7)	129.1(13)
S(5) - C(7) - S(7)	113.9(8)	C(7) - C(8) - S(6)	117.6(13)
C(7) - C(8) - S(8)	128.2(13)	S(6) - C(8) - S(8)	114.2(9)
C(10) - C(9) - S(7)	112.3(13)	C(9) - C(10) - S(8)	113.4(13)
C(12) - C(11) - S(9)	114.5(13)	C(11) - C(12) - S(10)	112.8(13)
C(14) - C(13) - S(9)	130.3(14)	C(14) - C(13) - S(11)	116.3(14)
S(9) - C(13) - S(11)	113.4(9)	C(13) - C(14) - S(10)	127.9(14)
C(13) - C(14) - S(12)	118.6(13)	S(10) - C(14) - S(12)	113.4(9)
C(16) - C(15) - S(11)	123.0(14)	C(16) - C(15) - S(12)	121.7(14)
S(11) - C(15) - S(12)	114.9(9)	C(15) - C(16) - S(13)	124.8(14)
C(15) - C(16) - S(14)	119.6(14)	S(13) - C(16) - S(14)	115.5(10)
C(18) - C(17) - S(13)	120.4(14)	C(18) - C(17) - S(15)	123.3(14)
S(13) - C(17) - S(15)	116.2(10)	C(17) - C(18) - S(16)	128.2(14)
C(17) - C(18) - S(14)	117.1(13)	S(16) - C(18) - S(14)	114.4(9)
C(20) - C(19) - S(15)	111.0(13)	C(19) - C(20) - S(16)	115.8(14)
O(1) - C(21) - O(2)	123(2)	O(1) - C(21) - C(21)#1	115.9(10)
O(2) - C(21) - C(21)#1	120.9(11)	O(3) - C(22) - O(5)	124(2)
O(3) - C(22) - C(23)	115.4(14)	O(5) - C(22) - C(23)	120.4(14)
O(6) - C(23) - O(4)	127(2)	O(6) - C(23) - C(22)	117.9(14)
O(4) - C(23) - C(22)	115.1(14)	C(27)#1 - C(24) - C(27)	116(2)
C(26)#1 - C(25) - C(26)	125(4)	C(25) - C(26) - C(27)	119(3)
C(28) - C(27) - C(26)	116(2)	C(28) - C(27) - C(24)	124(2)
C(26) - C(27) - C(24)	121(2)	N(1) - C(28) - C(27)	174(3)

Symmetry transformations used to generate equivalent atoms:
#1 - x, y, -z + 1/2

Atomic coordinates ($*10^4$) and equivalent isotropic displacement parameters ($Å^2 * 10^3$) for $(BEDT\text{-}TTF)_4NH_4Fe(C_2O_4)_3.C_6H_5CN$. U (eq) is defined as one third of the trace of the orthogonaliised Uij tensor.

Atom	x	y	z	U(eq)
Fe(1)	0	3093(2)	2500	18(1)
O(1)	561(10)	3867(5)	2824(3)	20(3)
O(2)	619(15)	4989(8)	2852(5)	68(5)
O(3)	855(10)	2370(5)	2813(3)	18(3)
O(4)	1649(10)	2999(5)	2215(3)	23(3)
O(5)	2430(12)	1607(7)	2781(4)	38(3)
O(6)	3474(12)	2400(6)	2217(4)	40(3)
S(1)	-308(4)	-165(2)	3642(1)	26(1)
S(2)	2639(5)	919(2)	4000(1)	31(1)
S(3)	216(4)	-730(2)	4426(1)	18(1)
S(4)	2257(4)	193(2)	4697(1)	20(1)
S(5)	138(4)	-1434(2)	5268(1)	20(1)
S(6)	2177(4)	-483(2)	5492(1)	21(1)
S(7)	-44(4)	-2126(2)	5997(1)	25(1)
S(8)	2502(4)	-1021(2)	6252(1)	26(1)
S(9)	-128(4)	7261(2)	3572(1)	28(1)
S(10)	2514(4)	8295(2)	3846(1)	24(1)
S(11)	-188(4)	6859(2)	4372(1)	28(1)
S(12)	2111(4)	7670(2)	4588(1)	27(1)
S(13)	-106(4)	6117(2)	5201(1)	26(1)
S(14)	2211(4)	6956(2)	5382(1)	24(1)
S(15)	184(4)	5266(2)	5895(1)	30(1)
S(16)	2818(4)	6206(2)	6076(1)	26(1)
C(1)	1826(19)	99(10)	3419(6)	42(5)
C(2)	2224(20)	805(11)	3513(6)	46(6)
C(3)	861(15)	-129(8)	4099(4)	19(4)
C(4)	1789(15)	282(8)	4231(5)	20(4)
C(5)	1178(15)	-448(8)	4792(4)	17(4)
C(6)	1147(15)	-774(8)	5141(4)	16(4)
C(7)	697(14)	-1482(8)	5731(4)	16(4)
C(8)	1656(16)	-1063(9)	5825(5)	26(4)
C(9)	1126(18)	-2236(10)	6370(5)	36(5)
C(10)	1497(17)	-1563(9)	6551(5)	29(4)
C(11)	607(17)	7952(9)	3328(5)	30(4)
C(12)	2054(17)	8003(9)	3378(5)	30(5)
C(13)	586(17)	7356(9)	4013(5)	25(4)
C(14)	1605(16)	7715(8)	4117(5)	22(4)
C(15)	1008(16)	7017(8)	4707(5)	24(4)
C(16)	1018(17)	6717(9)	5048(5)	28(4)
C(17)	794(17)	5931(8)	5605(5)	24(4)
C(18)	1824(16)	6273(8)	5681(5)	23(4)
C(19)	351(18)	5717(10)	6337(6)	37(5)
C(20)	1790(19)	5812(10)	6441(6)	40(5)
C(21)	296(17)	4432(9)	2694(5)	30(4)
C(22)	1873(16)	2144(8)	2673(4)	19(4)
C(23)	2373(15)	2534(8)	2331(4)	14(4)
C(24)	0	420(11)	2500	12(5)
C(25)	0	-987(21)	2500	81(12)

C(26)	1031(22)	-673(12)	2365(7)	54(6)
C(27)	1068(20)	35(11)	2365(6)	45(5)
C(28)	2039(27)	299(14)	2213(8)	9(6)
N(1)	2902(29)	599(15)	2082(9)	33(8)
N(2)	5000	1281(10)	2500	21(5)

Bond lengths (Å) for $(BEDT\text{-}TTF)_4(H_2O)Fe(C_2O_4)_3.C_6H_5CN$.

Bond	Bond Length (Å)	Bond	Bond Length (Å)
Fe(1) - O(1)	2.008(3)	Fe(1) - O(1)#1	2.008(3)
Fe(1) - O(2)#1	2.011(3)	Fe(1) - O(2)	2.011(3)
Fe(1) - O(5)#1	2.016(3)	Fe(1) - O(5)	2.016(3)
S(4) - C(5)	1.749(4)	S(4) - C(4)	1.768(4)
S(3) - C(5)	1.744(4)	S(3) - C(3)	1.752(4)
S(1) - C(3)	1.750(4)	S(1) - C(1)	1.822(5)
S(2) - C(4)	1.740(5)	S(2) - C(2)	1.827(4)
S(5) - C(6)	1.739(5)	S(5) - C(7)	1.764(4)
S(6) - C(8)	1.732(4)	S(6) - C(6)	1.755(4)
S(8) - C(8)	1.741(4)	S(8) - C(10)	1.803(5)
S(7) - C(7)	1.749(4)	S(7) - C(9)	1.791(4)
S(12) - C(14)	1.739(4)	S(12) - C(15)	1.756(4)
S(11) - C(15)	1.741(4)	S(11) - C(13)	1.750(4)
S(10) - C(14)	1.761(4)	S(10) - C(12)	1.793(5)
S(9) - C(13)	1.744(5)	S(9) - C(11)	1.808(5)
S(14) - C(16)	1.732(5)	S(14) - C(18)	1.766(5)
S(13) - C(16)	1.746(4)	S(13) - C(17)	1.747(5)
S(16) - C(18)	1.740(5)	S(16) - C(20)	1.812(4)
S(15) - C(17)	1.771(4)	S(15) - C(19)	1.803(5)
O(1) - C(21)	1.292(5)	O(2) - C(22)	1.285(5)
O(3) - C(21)	1.221(5)	O(4) - C(22)	1.235(5)
O(5) - C(23)	1.268(5)	O(6) - C(23)	1.243(5)
C(21) - C(22)	1.549(6)	C(23) - C(23)#1	1.536(9)
C(5) - C(6)	1.345(6)	C(4) - C(3)	1.343(5)
C(2) - C(1)	1.478(6)	C(7) - C(8)	1.369(6)
C(9) - C(10)	1.494(6)	C(15) - C(16)	1.363(6)
C(14) - C(13)	1.351(6)	C(12) - C(11)	1.495(6)
C(18) - C(17)	1.335(6)	C(20) - C(19)	1.523(5)
C(24) - C(25)#2	1.357(6)	C(24) - C(25)	1.357(6)
C(25) - C(26)	1.369(7)	C(27) - C(26)	1.394(6)
C(27) - C(26)#2	1.394(6)	C(27) - C(28)	1.436(9)
C(28) - N(1)	1.142(8)		

Bond angles for $(BEDT\text{-}TTF)_4(H_2O)Fe(C_2O_4)_3.C_6H_5CN$.

Bond	Angle (°)	Bond	Angle (°)
O(1) - Fe(1) - O(1)#1	159.2(2)	O(1) - Fe(1) - O(2)#1	86.77(13)
O(1)#1 - Fe(1) - O(2)#1	80.46(13)	O(1) - Fe(1) - O(2)	80.46(13)
O(1)#1 - Fe(1) - O(2)	86.77(13)	O(2)#1 - Fe(1) - O(4)	104.0(2)
O(1) - Fe(1) - O(5)#1	96.88(12)	O(1)#1 - Fe(1) - O(5)#1	99.18(12)
O(2)#1 - Fe(1) - O(5)#1	88.9(2)	O(2) - Fe(1) - O(5)#1	166.59(12)
O(1) - Fe(1) - O(5)	99.18(12)	O(1)#1 - Fe(1) - O(5)	96.88(12)
O(2)#1 - Fe(1) - O(5)	166.59(12)	O(2) - Fe(1) - O(5)	88.9(2)
O(5)#1 - Fe(1) - O(5)	78.5(2)	C(5) - S(4) - C(4)	95.8(2)
C(5) - S(3) - C(3)	95.2(2)	C(3) - S(1) - C(1)	96.5(2)
C(4) - S(2) - C(2)	103.7(2)	C(6) - S(5) - C(7)	95.7(2)
C(8) - S(6) - C(6)	95.6(2)	C(8) - S(8) - C(10)	101.0(2)
C(7) - S(7) - C(9)	101.5(2)	C(14) - S(12) - C(15)	94.8(2)
C(15) - S(11) - C(13)	95.5(2))	C(14) - S(10) - C(12)	98.1(2)
C(13) - S(9) - C(11)	102.2(2)	C(16) - S(14) - C(18)	95.7(2)
C(16) - S(13) - C(17)	94.3(2)	C(18) - S(16) - C(20)	101.2(2)
O(4) - C(22) - C(21)	120.5(4)	O(2) - C(22) - C(21)	114.6(4)
O(6) - C(23) - O(5)	126.6(4)	O(6) - C(23) - C(23)#1	119.9(3)
O(5) - C(23) - C(23)#1	113.5(2)	C(6) - C(5) - S(3)	123.4(3)
C(6) - C(5) - S(4)	121.9(3)	S(3) - C(5) - S(4)	114.7(2)
C(3) - C(4) - S(2)	129.1(3)	C(3) - C(4) - S(4)	115.7(3)
S(2) - C(4) - S(4)	115.1(2)	C(4) - C(3) - S(1)	124.8(3)
C(4) - C(3) - S(3)	118.3(3)	S(1) - C(3) - S(3)	116.7(2)
C(1) - C(2) - S(2)	115.8(3)	C(2) - C(1) - S(1)	113.3(3)
C(5) - C(6) - S(5)	123.0(3)	C(5) - C(6) - S(6)	121.9(3)
S(5) - C(6) - S(6)	115.0(2)	C(8) - C(7) - S(7)	129.1(3)
S(5) - C(7) - S(7)	113.9(8)	C(7) - C(8) - S(7)	129.4(3)
C(8) - C(7) - S(5)	115.9(3)	S(7) - C(7) - S(5)	114.7(2)
C(7) - C(8) - S(6)	117.7(3)	C(7) - C(8) - S(8)	126.8(3)
S(6) - C(8) - S(8)	115.4(2)	C(10) - C(9) - S(7)	114.8(3)
C(9) - C(10) - S(8)	114.0(3)	C(16) - C(15) - S(11)	123.9(3)
C(16) - C(15) - S(12)	121.0(3)	S(11) - C(15) - S(12)	115.1(2)
C(13) - C(14) - S(12)	118.2(3)	C(13) - C(14) - S(10)	126.7(3)
S(12) - C(14) - S(10)	115.1(2)	C(14) - C(13) - S(9)	129.4(3)
C(14) - C(13) - S(11)	116.4(3)	S(9) - C(13) - S(11)	114.0(2)
C(11) - C(12) - S(10)	113.2(3)	C(12) - C(11) - S(9)	114.3(3)
C(15) - C(16) - S(14)	122.0(3)	C(15) - C(16) - S(13)	122.4(3)
S(14) - C(16) - S(13)	115.6(3)	C(17) - C(18) - S(16)	129.7(4)
C(17) - C(18) - S(14)	115.3(4)	S(16) - C(18) - S(14)	115.0(2)
C(18) - C(17) - S(13)	119.2(3)	C(18) - C(17) - S(15)	127.8(4)
S(13) - C(17) - S(15)	113.0(2)	C(19) - C(20) - S(16)	113.3(3)
C(20) - C(19) - S(15)	115.4(3)	C(25)#2 - C(24) - C(25)	121.4(7)
C(24) - C(25) - C(26)	120.2(5)	C(25) - C(26) - C(27)	119.4(5)
C(26)#2 - C(27) - C(26)	119.4(6)	C(26)#2 - C(27) - C(28)	120.3(3)
C(26) - C(27) - C(28)	120.3(3)	N(1) - C(28) - C(27)	180.0(4)

Symmetry transformations used to generate equivalent atoms:

#1 - x, y, -z + 1/2 #2-x, y, -z+3/2

Atomic coordinates ($*10^4$) and equivalent isotropic displacement parameters ($Å^2 * 10^3$) for $(BEDT\text{-}TTF)_4(H_2O)Fe(C_2O_4)_3.C_6H_5CN$. U (eq) is defined as one third of the trace of the orthogonaliised Uij tensor.

Atom	x	y	z	U(eq)
Fe(1)	0	4191(1)	2500	17(1)
O(1)	1481(2)	4371(1)	2162(1)	20(1)
O(2)	1078(2)	4808(1)	2844(1)	21(1)
O(3)	3135(2)	5096(2)	2098(1)	26(1)
O(4)	2825(2)	5480(2)	2852(1)	27(1)
O(5)	772(3)	3411(1)	2800(1)	23(1)
O(6)	953(3)	2296(2)	2799(1)	31(1)
S(1)	-233(1)	4255(1)	6077(1)	17(1)
S(2)	2573(1)	3396(1)	6357(1)	21(1)
S(3)	1131(1)	4564(1)	5367(1)	16(1)
S(4)	3515(1)	3822(1)	5611(1)	16(1)
S(5)	2403(1)	4894(1)	4557(1)	15(1)
S(6)	4752(1)	4126(1)	4809(1)	16(1)
S(7)	3285(1)	5203(1)	3786(1)	21(1)
S(8)	6124(1)	4323(1)	4103(1)	23(1)
S(9)	3751(1)	2759(1)	1519(1)	23(1)
S(10)	833(1)	1951(1)	1209(1)	20(1)
S(11)	4569(1)	2467(1)	747(1)	17(1)
S(12)	2168(1)	1739(1)	492(1)	17(1)
S(13)	5790(1)	2134(1)	-76(1)	17(1)
S(14)	3349(1)	1433(1)	-314(1)	17(1)
S(15)	7088(1)	1909(1)	-792(1)	19(1)
S(16)	4134(1)	1102(1)	-1092(1)	19(1)
C(1)	657(4)	4327(2)	6541(1)	22(1)
C(2)	1323(4)	3703(2)	6667(1)	22(1)
C(3)	1141(4)	4146(2)	5808(1)	16(1)
C(4)	2225(4)	3810(2)	5926(1)	14(1)
C(5)	2666(3)	4277(2)	5249(1)	14(1)
C(6)	3186(4)	4407(2)	4912(1)	16(1)
C(7)	3651(4)	4829(2)	4231(1)	14(1)
C(8)	4739(4)	4477(2)	4356(1)	16(1)
C(9)	4827(4)	5146(2)	3570(1)	27(1)
C(10)	5502(4)	4488(2)	3620(1)	29(1)
C(11)	2284(4)	2622(2)	1773(1)	25(1)
C(12)	1612(4)	1973(2)	1682(1)	25(1)
C(13)	3327(4)	2418(2)	1070(1)	15(1)
C(14)	2234(4)	2084(2)	949(1)	15(1)
C(15)	3735(3)	2015(2)	385(1)	13(1)
C(16)	4231(4)	1876(2)	40(1)	17(1)
C(17)	5668(4)	1783(2)	-534(1)	17(1)
C(18)	4569(4)	1465(2)	-651(1)	19(1)
C(19)	6519(4)	1666(2)	-1269(1)	18(1)
C(20)	5717(3)	1026(2)	-1295(1)	15(1)
C(21)	2279(4)	4838(2)	2278(1)	21(1)
C(22)	2068(4)	5073(2)	2692(1)	21(1)
C(23)	504(4)	2833(2)	2671(1)	19(1)
C(24)	0	1092(4)	7500	45(2)

Atom	x	y	z	U(eq)
C(25)	913(5)	1424(3)	7307(2)	40(2)
C(26)	938(4)	2107(2)	7307(1)	29(1)
C(27)	0	2458(3)	7500	21(2)
C(28)	0	3175(3)	7500	27(2)
N(1)	0	3745(3)	7500	33(8)
O(7)	5000	6016(2)	2500	51(2)
H(1A)	1305(4)	4679(2)	6528(1)	26
H(1B)	50(4)	4456(2)	6731(1)	26
H(2A)	666(4)	3358(2)	6686(1)	26
H(2B)	1728(4)	3774(2)	6921(1)	26
H(9A)	4689(4)	5235(2)	3298(1)	32
H(9B)	5401(4)	5491(2)	3678(1)	32
H(10A)	6224(4)	4472(2)	3452(1)	35
H(10B)	4893(4)	4137(2)	3540(1)	35
H(11A)	2509(4)	2638(2)	2046(1)	30
H(11B)	1675(4)	2983(2)	1713(1)	30
H(12A)	959(4)	1894(2)	1867(1)	30
H(12B)	2250(4)	1616(2)	1706(1)	30
H(19A)	5992(4)	2026(2)	-1381(1)	22
H(19B)	7273(4)	1613(2)	-1422(1)	22
H(20A)	6207(3)	672(2)	-1163(1)	18
H(20B)	5587(3)	899(2)	-1562(1)	18
H(24)	0	628(4)	7500	54
H(25)	1524(5)	1187(3)	7175(2)	47
H(26)	1576(4)	2335(2)	7180(1)	35

References

1) Onnes, H. K., *Akad.van Wenterschappen (Amsterdam)* **1911** , *14,* 113, 818

2) Kittel, C., *Introduction to Solid State Physics VI edition Wiley Press.*

3) Bednorz, J. G. and Müller, K. A., *Z. Phys.* **1986**, B64, 189

4) Chu, C. W.; Hor, P. H.; Meng, R. L.; Gao, L.; Huang, Z. J.; Wang, Y. Q., *Phys. Rev. Lett.* **1987**,*58*, 405

5) Ihara, H.; Hirabayashi, M.; Tanino, H.; Tokiwa, K.; Ozawa, H.; Akahama, Y.; Kawamura, H., *Jap. J. Appl. Phys.* **1993**, *32*, 12A, 1732

6) Palstra, T. T. M.; Zhou, O.; Iwasa, Y.; Sulewski, P. E.; Fleming, R. M.; Zegarski, B. R., *Solid State Commun.* **1995**, *70*, 917

7) Gavaler, J. R. Appl. Phys. Lett., **1973**, *23*, 480,

8) Delk, F. S.; Sienko, M. J., *Inorg. Chem.* **1980**, *19*, 1352

9) Williams, J. M.; Kini, A. M.; Wang, H. H.; Carlson, K. D.; Geiser, U.; Montgomery, L. K.; Pyrka, G. J.; Watkins, D. M.; Kommers, J. M.; Boryschuk, S. J.; Strieby Crouch, A. V.; Kwok, W. K.; Schrieber, J. E.; Overmyer, D. L.; Whangbo, M. H., *Inorg. Chem.*, **1990**, *29*, 3262

10) Fertig, W. A.; Johnston, D. C.; DeLong, L. E.; McCallum, R. W.; Maple, M. B.; Matthias, B. T., *Phys. Rev. Lett.* **1977**, 38, 17, 987

11) Rosenberg, H. M., *The Solid State,* Oxford Science Publications

12) Mazumdar, C.; Ghosh, K.; Ramakrishnan, S.; Nagarajan, R.; Gupta, L. C.; Chandra, G.; Padalia, B. D.; Vijayaraghavan, R., *Phys. Rev. B* **1994**, *50*, 118, 879

13) O' Hare, D.; Wong, H. V.; Hazell, S.; Hodby, J. W., *Advanced Materials* **1992**, *4*, 10 ,658

14) McCoy, H. N.; Moore, W. C., J. Am. Chem. Soc.1911, **33**, 273

15) Little, W. A., *Phys. Rev.* **1964**, *134A*, 1416

16) Ferraris, J.; Cowan, D. O.; Walatka, V. J.; Perlstein, J. H., *J. Am. Chem. Soc.* **1973**, *95*, 948

17) Bechgaard, K.; Jacobsen, C. S. ; Mortensen, K. ; Pedersen, M. J.; Thorup, N., *Solid State Commun.* **1980**, *33*, 1119

18) Moret, R.; Pouget, J. P.; Comes, R.; Bechgaard, K., *Phys. Rev. Lett.* **1982**, *49*, 1008

19) Bechgaard, K.; Jacobsen, C. S.; Mortensen, K; Pedersen, H. J.; Thorup, N., *Solid State Commun.*, **1980**, *33*, 1119

20) Mizuno, M.; Garito, A. F.; Cava, M. P., *J. Chem. Soc. Chem. Comm.* **1978**, 18

21) Williams, J. M.; Kini, A. M.; Wang, H. H.; Carlson, K. D.; Geiser, U.; Montgomery, L. K.; Pyrka, G. J.; Watkins, D. M.; Kommers, J. M.; Boryschuk, S. J.; Strieby Crouch, A. V.; Kwok, W. K.; Schrieber, J. E.; Overmyer, D. L.; Whangbo, M. H., *Inorg. Chem.*, **1990**, *29*, 3262

22) Williams, J. M.; Kini, A. M.; Geiser, U.; Wang, H. H.; Carlson, K. D.; Kwok, W. K.; Vandervoort, K. G.; Thompson, J. E.; Stupka, D. L.; Jung, D.; Whangbo, M. H., *Proc. Intl. Conf. Organic Superconductors*; South Lake Tahoe, CA, May **1990**.

23) Komatsu, T.; Nakamura, T.; Matsukawa, N.; Yamochi, H.; Saito, G.; Ito, H.; Ishiguro, T.; Kusunoki, M.; Sakaguchi, K., *Solid State Commun.* **1991**, *80*, 843

24) Posselt, H.; Muller, H.; Andres, K.; Sushko, Y. V.; Saito, G., *Synth. Met.* **1995**, *70*, 917

25) Urayama, H.; Yamochi, H.; Saito, G.; Nozawa, K.; Sugano, T.; Kinoshita, M.; Sato,S.; Oshima, K.; Kawamoto, A.; Tanaka, J., *Chem. Lett.* **1988**, 55

26) Williams, J. M.; Schlueter, J. A.; Geiser, U.; Wang, H. H.; Dudek, J. D.; Kelly, M. E.; Sirchio, S. A.; Carlson, K. D.; Naumann, D.; Roy, T., **1995** ISCOM (Conference Abstracts)

27) Graham, A. W.; Kurmoo, M.; Day, P. *J. Chem. Soc. Chem. Comm. (in press)*

28) Qian, M. X.; Wang, X. H.; Zhu, Y. L.; Zhu, D.; Li, L.; Ma, B. H.; Duan, H. M.; Zhang, D. L., *Synth. Met.* **1988**, *27*, A277

29) Bender, K.; Henning, I.; Schweitzer,D.; Dietz, K.; Endres, H.; Keller, H. J., *Mol. Cryst. Liq. Cryst.* **1984**, *108*, 359

30) Shibaeva, R. P.; Rozenberg, L. P., *Kristallografiya* **1988**, *33*, 1402

31) Wang, H. H.; Beno, M. A.; Geiser, U.; Firestone, M. A.; Webb, K. S.; Nunez, L.; Crabtree, G. W.; Carlson, K. D.; Williams, J. M.; Azevedo, L. J.; Kwak, J. F.; Schreiber, J. E., *Inorg, Chem.* **1985**, *24*, 2465

32) Kurmoo, M.; Talham, D. R.; Pritchard, K. L.; Day, P.; Stringer, A. M.; Howard, J. A. K., *Synth. Met.* **1988**, *27*, A177

33) Lyubovskaya, R. N.; Zhilyaeva, E. I.; Pesotskii, S. I.; Lyubovskii, R. B.; Atovmyan, L. O.; D'yachenko, O. A.; Takhirov, T. J., *JETP Lett.* **1987**, 46, 188

34) Schlueter, J. A.; Geiser, U.; Williams; J. M., Wang; H. H., Kwok, W. K..; Fendrich, J. A.; Carlson, J. D.; Achenbach,C. A.; Dudek, J. D.; Naumann, D.; Roy, T.; Schirber, J. E.; Bayless, W. R., *J. Chem. Soc. Chem. Comm.* **1994**, *13*, 1599

35) Komatsu, T.; Nakamura, T.; Matsukawa, N.; Yamochi, H.; Saito, G.; Ito, H.; Ishiguro, T.; Kusonoki, M.; Sakaguchi, K., *Solid State Commun.* **1991**, *80*, 843

36) Kajita, K.; Nishio, Y.; Moriyama, S.; Sasaki, W.; Kato, R.; Kobayashi, H.; Kobayashi, A., *Solid State Commun.* **1987**, *64*, 1279

37) Kato, R.; Kobayashi, H.; Kobayashi, A.; Nishio, Y.; Kajita, K.; Sasaki, W., *Chem. Lett.* **1986**, 833

38) Williams, J. M.; Wang, H. H.; Beno, M. A.; Emge, T. J.; Sowa, L. M.; Copps, P. T.; Behroozi, F.; Hall, L. N.; Carlson, K. D.; Crabtree, G. W., *Inorg. Chem.* **1984**, *23*, 3839

39) Shibaeva, R. P.; Kaminskii, V. F.; Yagubskii, E. B., *Mol. Cryst. Liq. Cryst.* **1985**, *119*, 361

40) Parkin, S. S. P.; Engler, E. M.; Schumaker, R. R.; Lagier, R.; Lee, V. Y.; Scott, J. C.; Greene, R. L., *Phys. Rev. Lett.* **1983**, *50,* 270

41) Mori, H.; Hirabayashi, I.; Tanaka, S.; Mori, T.; Maruyama, Y.; Inokuchi, H., *Solid State Commun.* **1991**, *80*, 411

42) Rosseninsky, M. J.; Kurmoo, M.; Talham, D. R.; Day, P.; Chasseau, D., *J. Chem. Soc., Chem. Commun.* **1988**, 88

43) Williams, J. M.; Emge, T. J.; Wang, H. H.; Beno, M. A.; Copps, P. T.; Hall, L. N.; Carlson, K. D.; Crabtree, G. W., *Inorg Chem.* **1984**, *23*, 2558

44) Mori, T.; Kato, K.; Maruyama, Y.; Inokuchi, H.; Mori, H.; Hirabayashi, I.; Tanaka, S., *Solid State Commun.* **1992**, *82*, 177

45) Mori, H.; Tanaka, S.; Oshima, M.; Saito, G.; Mori, T.; Maruyama, Y.; Inokuchi, H., *Bull. Chem. Soc. Jpn.* **1990**, *63*, 2183

46) Williams, J. M.; Wang, H. H.; Emge, T. J.; Geiser, U.; Beno, M. A.; Leung, P. C.; Carlson, K. D.; Thorn, R. J.; Schultz, A. J.; Whangbo, M. H., *Prog. Inorg. Chem.* **1987**, *35*, 51

47) Fleming, R. M. ; Ramirez, A. P.; Rosseinsky, M. J.; Murphy, D. W.; Haddon, R. C.; Zahurak, S. M.; Makhija, A. V., *Nature* **1991**, *352*, 787

48) Rovira, C.; Whangbo, M.-H., *Synth. Met.* **1993**, 145

49) Yamochi, H.; Komatsu, T.; Matsukawa, N.; Saito, G.; Mori, T.; Kusunoki, M.; Sakaguchi, K., *J. Am. Chem. Soc.* **1993**, *115*, 11319

50) Kato, R.; Kobayashi, H.; Kobayashi, A., *Synth. Met.* **1991**, *41*, 2093

51) Suzuki, T.; Yamochi, H.; Srdanov, G.; Hinkelmann, K.; Wudl, F., *J. Am. Chem. Soc.* **1989**, *111*, 3108

52) Kikuchi, K.; Namiki, T.; Ikemoto, I.; Kobayashi, H., *J. Chem. Soc. Chem. Comm.* **1986**, 1472

53) Moore, A. J.; Bryce, M. R.; Ando, D.; Hursthouse, M. B., *J. Chem. Soc. Chem. Comm.* **1991**, 320

54) Steimecke, G.; Sieler, H. J.; Kirmse, R.; Hoyer, E., *Phosphorous and Sulfur* **1979**, *7*, 49

55) Kobayashi, H.; Udagawa, T.; Tomita, H.; Bun, K.; Naito, T.; Kobayashi, A.; *Chem. Lett.*, **1993**, 1559

56) Kobayashi, H.; Tomita, H.; Naito, T.; Tanaka, H.; Kobayashi, A.; Saito, T., *J. Chem. Soc. Chem. Comm.* **1995**,*12,* 125

57) Brossard, L.; Hurdequint, H.; Ribault, M.; Valade, L.; Legros, J. P.; Cassoux, P., *Synth. Met.* **1988**, *27*, B157

58) Cassoux, P.; Errami, A.; Kushsch, N.; Faulmann, C.; Malfant, I.; Legros, J. P.; Kobayashi, H., **1995** ISCOM (Conference Abstracts)

59) Kobayashi, A.; Kim, H.; Sasaki, Y.; Kato, R.; Kobayashi, H.; Moriyama, S.; Nishio, Y.; Kajita, K.; Sasaki, W., *Chem. Lett.* **1987**, 1819

60) Papavassiliou, G. C.; Mousdis, G. A.; Zambounis, J. S., Terzis, A.; Hountas, A.; Hilti, B.; Mayer, C. W.; Pfeiffer, J., *Synth. Met.* **1988**, *27*, B379

61) Kikuchi, K.; Saito, K.; Ikemoto, I.; Murata, K.; Ishiguro, T.; Kobayashi, K., *Synth. Met.* **1988**, *27*, B269

62) Brossard, L.; Hurdequint, H.; Ribault, M.; Valade, L.; Legros, J. P.; Cassoux, P., *Synth. Met.* **1988**, *27*, B157

63) Brossard, L.; Ribault, M.; Valade, L.; Cassoux, P., *C. R. Acad. Sc. (Paris),* **1986**, *302*, 205

64) Beno, M. A.; Wang, H. H.; Kini, A. M.; Carlson, K. D.; Geiser, U.; Kwok, W. K.; Thompson, J. E.; Williams, J. M.; Ren, J.; Whangbo, M. H., *Inorg. Chem.* **1990**, *29*, 1599

65) Ishikawa, Y.; Saito, K.; Kikuchi, K.; Ikemoto, I.; Kobayashi, K.; Anzai, H., *Acta. Cryst.* **1990**, *C46*, 1652

66) Kikuchi, K.; Ishikawa, Y.; Saito, K.; Ikemoto, I.; Kobayashi, K., *Acta. Cryst.* **1988**, *C44*, 466

67) Kikuchi, K.; Ishikawa, Y.; Saito, K.; Ikemoto, I.; Kobayashi, K., *Synth. Met.* **1988**, *27*, B391

68) Ishikawa, Y.; Kikuchi, K.; Saito, K.; Ikemoto, I.; Kobayashi, K., *Acta. Cryst.* **1989**, *C45*, 572

69) Yoshino, H.; Saito, K.; Kikuchi, K.; Nishikawa, H.; Kobayashi, K.; Ikemoto, I., *J. Phys. Soc. Jpn.* **1995**, *64*, 7, 2307

70) Bleaney, B.; Bowers, K. D., Proc. Roy. Soc.(London) **1952**, *A214*, 451

71) Jung, D.; Evain, M.; Novoa, J. J.; Whangbo, M. H.; Beno, M. A.; Kini, A. M.; Scultz, A. J.; Williams, J. M.; Nigrey, P. J., *Inorg. Chem.* **1989**, *28*, 4516

72) Emge, T. J.; Wang, H. H.; Geiser, U.; Beno, M. A.; Webb, K. S.; Williams, J. M., *J. Am. Chem. Soc.* **1986**, *108*, 3849

73) Bardeen, J.; Cooper, L. N.; Schreiffer J. R. *Phys. Rev.*, **1957**, *108*, 1175

74) Meissner, W.; Ochsenfeld, R., *Naturwissenschaften* **1933**, *21*, 787

75) Siegrist, T.; Zandbergen, H. W.; Cava, R. J.; Krajewski, J. J.; Peck W. F., *Nature* **1994**, *367* , 254

76) Beauchamp, K. M.; Spalding, G. C.; Huber, W. H.; Goldman, A. M., *Phys. Rev. Lett.*, **1994**, *73*, 2752

77) Ishikawa, M.; Fisher, Ø., *Solid State Commun.*, **1977**, *23*, 37

78) Grigereit, T. E.; Lynn, J. W.; Huang, Q.; Santoro, A.; Cava, R. J.; Krajewski, J. J.; Peck, W. F., *Phys. Rev. Lett.* **1994**, *73*, (20), 2756

79) Mallah, T.; Hollis, C.; Bott, S.; Kurmoo, M.; Day, P. *J. Chem. Soc. Dalton Trans.* **1990**, 859

80) Mathonière, C.; Carling, S. G.; Dou, Y.; Day, P. *J. Chem. Soc. Chem. Comm.* **1994**, 1551

81) Larsen, J.; Lenoir, C., *Synthesis*, **1988**, *2*, 134

82) Bailar, J. C.; Jones, E. M., *Inorg. Synthesis* **1939**, *1*, 35

83) Coucouvanis, D.; Piltingsrud, D., *J. Am. Chem. Soc.* **1973**, 5556

84) Mann, K. P. Thesis *Universistät Marburg* (**1977**)

85) Sprenger, H. E.; Ziegenbein, W., *Angew. Chem. Int. Ed. Engl.* **1968**, *7*, 530

86) Gerecht, B.; Kämpchen, T.; Köhler, K.; Massa, W.; Offermann, G.; Schmidt, R. E.; Seitz, G.; Sutrisino, R., *Chem. Ber.* **1984,** *117,* 2714

87) Maahs, G., *Liebigs Ann. Chem.* **1965,** *686*, 55

88) Seitz, G., Personal Communication.

89) Almann, R.; Debaerdemaker, T.; Mann, K. P.; Mautsch, R.; Schmeidal, R.; Seitz, G., *Chem. Ber.* **1976**, *109*, 2208

90) Shelldrick, G. M., *Acta Cryst A* **1990**, *46*, 467

91) Descurtins, S.; Scmalle, H. W.; Oswald, H. R.; Linden, A.; Ensling, J.; Gütlich, P.; Hanser, A., *Inorg. Chim. Acta*, **1994**, *65*, 216

92) Farrel, R. P.; Hambley, T. W.; Lay, P., *Inorg. Chem.* **1995**, *34*, 757

93) Merrachi, E- H.; Mentzen, B. F.; Chassagneux, F.; Boux, J., *Revue de Chimie Minerale* **1987**, *24*, 56

94) Hamilton, W. C.; Ibers, J. A., Hydrogen Bonding in Solids, W. A. Benjamin, Inc. (1968)

95) Kurmoo, M.; Pritchard, K. L.; Talham, D. R.; Day, P.; Stringer, A. M.; Howard, J. A. K., *Acta Cryst.* **1990**, *B46*, 348

96) Handbook of Chemistry and Physics. Weast 66th Edition (1985 - 1986) CRC Press.

97) Kurmoo, M.; Day, P.; Stringer, A. M.; Howard, J. A. K.; Ducasse, L.; Pratt, F. L.; Singleton, J.; Hayes, W., *J. Mater. Chem.* **1993**, *3*, 1161

98) Carling, S. G.; Mathonière, C.; Nuttall, C. J.; Day, P.; Coles, S.J.; Malik, A., Manuscript in preparation.

99) Nozawa, K.; Sugano, T.; Urayama, H.; Yamochi, H.; Saito, G.; Kinoshita, M., *Chem. Lett.* **1988**, 617

100) Caulfield, J. L., Personal Communication

101) Wosnitza, J., *Int. J. Mod. Phys. B*, **1993**, 15, 2707

102) Hollis, C. Part II Thesis, University of Oxford 1987

Bibliography

Williams, J. M., Ferraro, J. R., Thorn, R. J., Carlson, K. D., Geiser, U., Wang, H. H., Kini, A. M., Whangbo, M. H.; Organic Superconductors (including Fullerenes), Synthesis, Structure, Properties and Thoery, Prentice Hall (1992)

Carlin, R. L., *Magnetochemistry* Springer-Verlag (1986)

Kahn, O., *Molecular Magnetism*

Kittel, C., *Introduction to Solid State Physics VI edition* Wiley Press.

Murrell, J. N.; Kettle, S. F. A.; Tedder, J. M., *The Chemical Bond* John Wiley and Sons (1985)

Pierrot, M., *Structure and Properties of Molecular Crystals* Elsevier Science Publishers B. V. (1990)

Rosenberg, H. M., *The Solid State,* Oxford Science Publications

Hoffmann, R., *Solids and Surfaces. A Chemist's View of Bonding in Extended Structures.* VCH Publishers, Inc (1988)

Cox, P. A., *The Electronic Structure of Solids* , Oxford Science Publications (1995)